Solar Radiation Processes on the East Antarctic Plateau: Interaction of Clouds, Snow, and Atmospheric Gases

Stephen R. Hudson

A dissertation submitted in partial fulfillment of
the requirements for the degree of

Doctor of Philosophy

University of Washington

2007

Program Authorized to Offer Degree: Atmospheric Sciences

University of Washington
Graduate School

This is to certify that I have examined this copy of a doctoral dissertation by

Stephen R. Hudson

and have found that it is complete and satisfactory in all respects,
and that any and all revisions required by the final
examining committee have been made.

Chair of the Supervisory Committee:

Stephen G. Warren.

Stephen G. Warren

Reading Committee:

Stephen G. Warren.

Stephen G. Warren

Thomas C. Grenfell

Thomas C. Grenfell

Thomas P. Ackerman

Date: 19 October 2007

In presenting this dissertation in partial fulfillment of the requirements for the doctoral degree at the University of Washington, I agree that the Library shall make its copies freely available for inspection. I further agree that extensive copying of this dissertation is allowable only for scholarly purposes, consistent with "fair use" as prescribed in the U.S. Copyright Law. Requests for copying or reproduction of this dissertation may be referred to Proquest Information and Learning, 300 North Zeeb Road, Ann Arbor, MI 48106-1346, to whom the author has granted "the right to reproduce and sell (a) copies of the manuscript in microform and/or (b) printed copies of the manuscript made from microform."

Signature 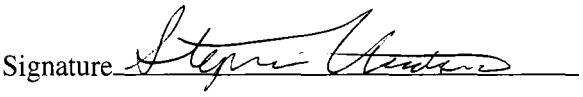

Date 2 November 2007

University of Washington

Abstract

Solar Radiation Processes on the East Antarctic Plateau:
Interaction of Clouds, Snow, and Atmospheric Gases

Stephen R. Hudson

Chair of the Supervisory Committee:
Professor Stephen G. Warren
Atmospheric Sciences

The bidirectional reflectance distribution function (BRDF) of snow was measured from a 32-meter tower at Dome C, at latitude 75°S on the East Antarctic Plateau. These measurements were made at 96 solar zenith angles between 51° and 87°, and cover wavelengths 350–2400 nm, over the full range of viewing geometry.

Parameterizations are presented for the anisotropic reflectance factor using a small number of empirical orthogonal functions. The parameterizations cover nearly all viewing angles and are applicable to the high parts of the Antarctic Plateau that have small surface roughness.

It has been a long-standing puzzle why clouds, which should interact with solar radiation similarly to a thin layer of snow, have such a dramatic effect on the reflectance observed by satellites over snow-covered regions. The presence of a cloud over the snow strongly enhances the anisotropy of the scene; by contrast, when a plane-parallel cloud is placed above a plane-parallel snow surface in a model, it slightly decreases the anisotropy of the system due to the cloud's smaller particles.

Using the surface-reflectance parameterizations, I show that this effect of clouds over snow is due to the non-plane-parallel nature of the snow surface, not to unexpected features of the clouds. The snow-surface roughness reduces the anisotropy of the reflected sunlight compared to that from a plane-parallel snow surface. Clouds hide this roughness with a surface that is very smooth in units of optical depth. I use the surface parameterization to accurately model

reflectance observations made from above cloud-covered snow.

I also use these parameterizations in a model to calculate the directional reflectance above Dome C, integrated over the solar spectrum, for comparison with observations from Clouds and the Earth's Radiant Energy System (CERES). These comparisons suggest that the CERES radiances may be biased low, by about 5%, but that the anisotropic reflectance factors used by CERES to convert radiance to flux are appropriate for use over the region. A study of the effect of atmospheric variations on anisotropy suggests this is not likely to introduce significant uncertainty into CERES results.

TABLE OF CONTENTS

LIST OF FIGURES

LIST OF TABLES

GLOSSARY

ADM: Angular distribution model used to convert satellite radiance observations to fluxes

BRDF: Bidirectional reflectance distribution function, see Equation 2.1

BRF: Bidirectional reflectance factor, see Section 3.4; differs from BRDF by a factor of π

CERES: Clouds and the Earth's Radiant Energy System, a suite of satellite instruments for observing components of the Earth radiation budget

DISORT: A discrete ordinates radiative transfer model

ERBE: The Earth Radiation Budget Experiment, an older program for observing the Earth radiation budget, the predecessor of CERES

$F_\circ$: Incident (downwelling) flux

g: Asymmetry factor

I_r: Reflected (upwelling) radiance

MISR: Multiangle Imaging Spectroradiometer

MODIS: Moderate Resolution Imaging Spectroradiometer

R: Anisotropic reflectance factor, see Equation 2.2; differs from BRF by a factor of the albedo

R_f: R at the forward reflectance peak

r_{eff}: Effective radius

SBDART: Santa Barbara DISORT Atmospheric Radiative Transfer model, a spectral atmospheric radiative transfer model built around DISORT

TOA: Top-of-atmosphere; top of the atmosphere

α: Albedo

$\theta_\circ$: Solar zenith angle

θ_v: Viewing zenith angle

λ: Wavelength

$\mu_\circ$: Cosine of the solar zenith angle

ρ: Mathematical symbol for BRDF

ϕ: Relative azimuth angle

$\phi_\circ$: Solar azimuth angle

ϕ_v: Viewing azimuth angle

ACKNOWLEDGMENTS

Many people have contributed in a wide variety of ways to help me reach the point of presenting this dissertation. Without some, the work presented here would not have been done as well; without others, I may never have had the opportunity to pursue this degree or the determination to complete it. Below I list some of those who have been most important in helping me get here. No doubt I have left some people out who should be included here, and I apologize for that.

My research experience at the University of Washington has been shaped by my advisor, Steve Warren, and I have been very fortunate for that. His excellent advice has always improved my work, and without his incredibly helpful editing, I am sure to find publishing to be more difficult in the future. Studying under Steve ensured that I received an excellent education without the frustration and stress that sometimes seem to come from graduate work. I feel very lucky that he invited me to join his research group shortly after I arrived here, and I hope we will have the opportunity to work together in the future.

I am also grateful to the rest of my advisory committee, Tom Grenfell, Tom Ackerman, Qiang Fu, and Norm McCormick. Their help and guidance has improved the work presented here.

Without support from Mike Wallace I might not be at the University of Washington. He agreed to take me on as a student, even though my interests were not entirely in line with his work, and while he remained my advisor he worked at ensuring that we could find ways for me to pursue my interests. I could not resist the offer from Steve to work in Antarctica, but I am sure that had it not come, my time here would have been very fulfilling and rewarding working with Mike.

Another way in which I have benefited from being advised by Steve is through the wonderful people he surrounds himself with. Von Walden co-advised me on my masters project and has been very helpful throughout my time here. Mike Town accepted me as a last-minute, unexpected coworker to be stuck with for nearly a year at the South Pole; he helped make my experience there enjoyable and has remained a good friend and coworker here in Seattle. Rich Brandt and Tom Grenfell have both improved my experiences on field campaigns and helped me with my work along the way. Melanie Fitzpatrick and Ryan Eastman have both been wonderful officemates and Penny Rowe helped me figure out some things along the way and always provided

encouragement.

I have been fortunate to have had several opportunities to do work in the field while I have been here, and these experiences have been better because of the people I was working with. The rest of the 2001 South Pole winterover crew all played a big part in that piece of my graduate career, especially Andrea Grant, who has remained a good friend and colleague. At Dome C, I also benefited from working closely with Delphine Six, Lance Roth, and Brad Halter. The proposal to use Dome C was sponsored by Michel Fily. I am also grateful to all of the people at both Dome C and South Pole who worked to make our projects successful. On a recent field project with Tom Grenfell in Russia we were helped greatly from the assistance of Valeriy Ippolitov, Mikhail Lamakin, Vladimir Radionov, and Victor Boyarsky.

My work has benefited from interaction with others outside of Steve's group as well. Discussions with Seiji Kato, Norman Loeb, Tom Charlock, Elise Hendriks, Larry Di Girolamo, and Michael Wilson were all helpful. Seiji Kato also provided me with the CERES ADMs for use in Chapter 4. Yu Xie and Ping Yang computed the ice-crystal phase functions used in Chapter 3. Ronald Welch, Nadine Nereson, and Steve Warren provided figures used in Chapter 3. MISR and CERES data were obtained from the NASA Langley Atmospheric Sciences Data Center.

Of course this work could not have happened without funding, so I thank the National Science Foundation Office of Polar Programs for funding us through grants OPP-97-26676, OPP-02-30466, OPP-00-03826, and ANT-06-36993.

Fortunately, my experiences here have extended beyond my work, and I am very grateful to all of my friends here in Seattle, including this department's graduate classes from 2000 and 2001. These friends have helped make Seattle a wonderful place to live and I hope they will all come to visit when I move to Norway.

Finally, I thank my family for all of the love and support they have given me throughout my life. I owe my success to them. I am sure that at times over the last few years they thought I would be in school forever, but they have always supported and encouraged me in all of my decisions. I wish my grandmother were alive to see this; I believe she and Betty Scruggs both provided me with the curiosity and desire to learn that have gotten me here. Most importantly, my mother has done everything possible my entire life to make sure I always had what I needed and lived up to my potential. Without her never-ending support, this dissertation would not exist.

Chapter 1

INTRODUCTION

The East Antarctic Plateau is the high-elevation portion of the Antarctic Ice Sheet, including most of Antarctica more than a few hundred kilometers from the coast, from the Greenwich Meridian, through 90° E, to about 145° E. Its approximate extent is shown by the red contour in Figure 1.1. With surface elevations from about 2500 to 4100 m, surface slopes less than 0.3°, and continuously sub-freezing temperatures, it is a remarkably homogeneous area covering about 5.5 million square kilometers. The low temperatures found on the Plateau all year limit temporal variability of the snow surface by slowing metamorphosis rates of near-surface snow grains. The entire Plateau is covered by clean, cold snow, so spatial variability consists primarily of variations in the size and orientation of surface roughness features. Its permanent snow cover and its location inside the Antarctic Circle make it a region of extremes with respect to solar radiation, among other things.

With continuous sunlight for the summer months, parts of the Plateau have more solar radiation incident at the top of the atmosphere over the course of a midsummer day than is incident at the top of the atmosphere above any other part of the planet at any time of year. However, the perpetually cold, fine-grained snow surface of the Plateau has an albedo of about 0.8, ensuring that the upward flux of solar radiation in summer is also one of the highest in the world. The combination of high albedo and low solar elevation means the atmosphere plays an important part in determining the solar radiation budget of the Antarctic Plateau; indeed, it is one of the few regions of the planet where the top-of-atmosphere (TOA) albedo is lower than the surface albedo.

Accurately determining the TOA albedo over bright surfaces is important for studies of the Earth's radiation budget since small errors or changes in the albedo of bright regions lead to large relative errors or changes in the absorbed solar energy. Satellite instruments provide a

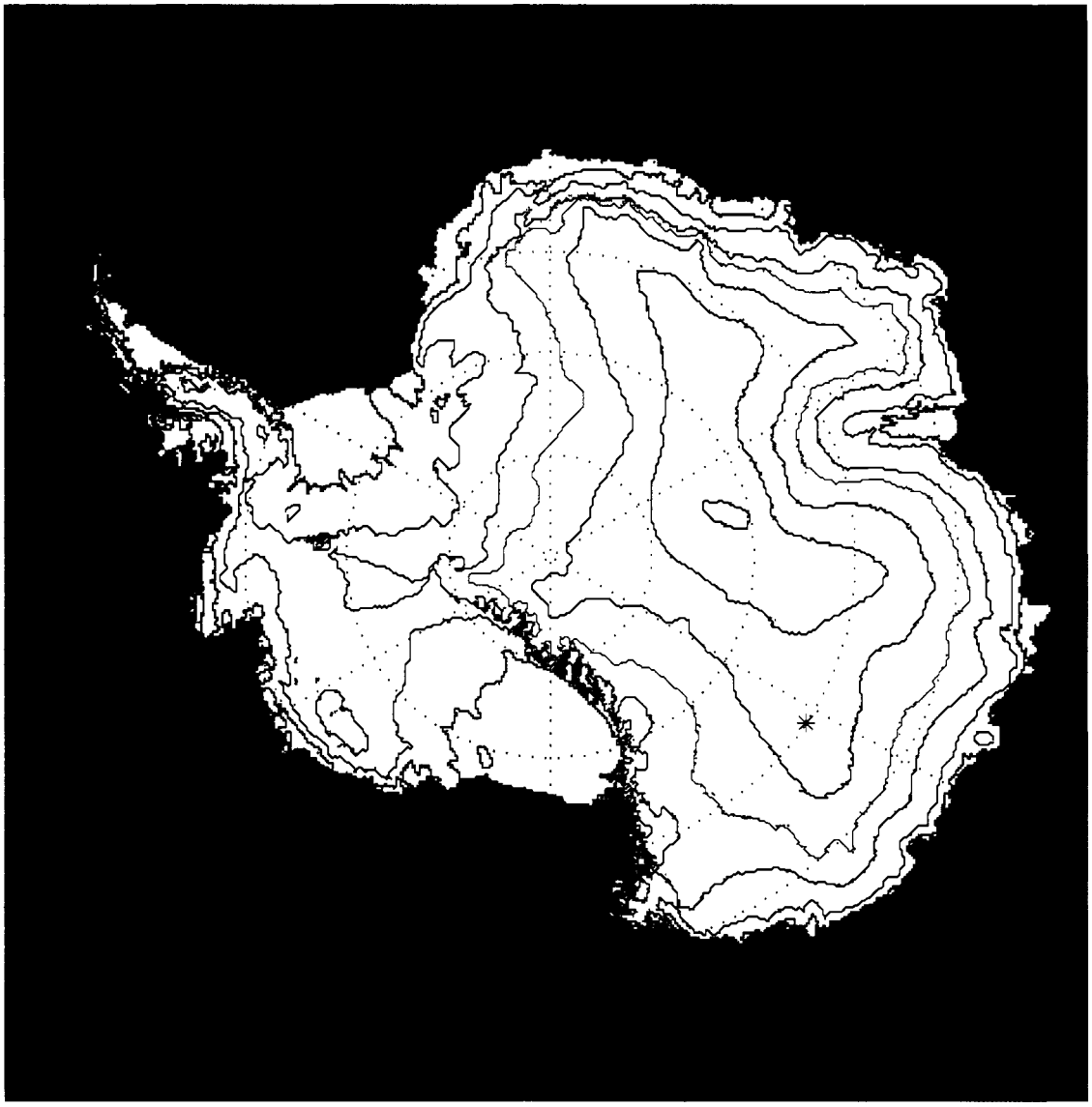

Figure 1.1: This map shows contours of surface elevation on Antarctica. The contours are at 1000, 2000, 2500, 3000, 3500, and 4000 m; the 2500-meter contour is in red and is an approximate limit of the East Antarctic Plateau. The red asterisk marks the location of Dome C station, where our measurements were made.

convenient way to observe otherwise under-monitored regions of the planet, including the East Antarctic Plateau, but to make use of their data—to determine albedo or to derive other properties remotely—we must have a good knowledge of the angular distribution of the reflected radiance. Calculating albedo requires integrating the upwelling radiance over all viewing angles, something that cannot generally be done in a short time by satellite instruments; knowing how the radiance varies with viewing angle allows a radiance observation at a single viewing angle to be converted to upwelling flux, or albedo.

Modelling radiative transfer through the atmosphere, to the surface, and back to space requires knowing the angular distribution of the reflected radiance at the surface. This affects not only the resulting modeled angular distribution at the TOA, which may be used for interpreting satellite observations, but also the modeled atmospheric radiation budget, since the atmosphere will absorb more of the upwelling radiation if it is preferentially reflected into large zenith angles rather than straight up.

This dissertation examines the role of snow-surface features, clouds, and atmospheric gases in determining the angular distribution of reflected sunlight over the East Antarctic Plateau. Beginning with observations of the reflected radiance field at the surface, a parameterization is developed to calculate the anisotropic reflectance factor for the Plateau snow surface as a function of solar zenith angle and viewing angles. This parameterization is then used as the lower boundary in radiative transfer models to explain the effect of clouds on the reflected radiance field at the TOA and to examine the angular distribution models used with and observations made by Clouds and the Earth's Radiant Energy System (CERES) instruments. The results presented here will help scientists using radiative transfer models or interpreting satellite observations to better understand and explain their results over an area where the interaction of solar radiation, the atmosphere, and the surface can be quite different from what happens over most of the planet.

Chapter 2

OBSERVATIONS AND PARAMETERIZATIONS

This chapter was published under the title "Spectral bidirectional reflectance of Antarctic snow: Measurements and parameterization" in 2006 in *Journal of Geophysical Research* **111** (D18106) with coauthors Stephen G. Warren, Richard E. Brandt, Thomas C. Grenfell, and Delphine Six. My coauthors designed and helped carry out the experiment at Dome C; Brandt and Grenfell acquired and built the necessary equipment for our observations, and kept it functioning in the field; all of the coauthors gave comments on the manuscript, and Warren, in particular, provided me excellent guidance on carrying out the work and helped me greatly with improving the manuscript.

2.1 Introduction

The light reflected from a snow surface is diffuse, but not isotropic. This anisotropy is sometimes apparent to the unaided eye and can often be important for geophysical observations and modelling. The angular distribution of reflected light is described by the bidirectional reflectance distribution function (BRDF); here, bidirectional refers to the two directions of interest: that from which the light is coming and that into which the light is being reflected.

Knowledge of a surface's BRDF is a necessary lower boundary condition for accurate modelling of radiative transfer through the atmosphere. Such knowledge is also important for the interpretation of remote-sensing observations. Remote-sensing applications using reflected sunlight generally begin with a measurement of radiance coming from a particular direction. An understanding of the BRDF of the scene being viewed is required either to convert the measured radiance to an upwelling flux, or to normalize the radiance to account for the angular distribution of the reflected light before using it to determine other properties of the scene.

If the radiance measurements are made near the surface, as with many aircraft measurements, then it is the BRDF of the surface that is obtained. For remote sensing using sensors on satellites it is the BRDF of the surface-atmosphere system that is required. Determining this top-of-atmosphere BRDF is difficult because satellites cannot view a scene from all angles in a short period, so the top-of-atmosphere BRDF pattern is typically inferred by combining numerous observations of the same scene type with similar solar zenith angles that were made at different times and span the available range of satellite viewing angles (Loeb et al. 2005). That method does not require the surface BRDF, but having knowledge of it allows an evaluation of the accuracy of the satellite-derived top-of-atmosphere BRDF.

Loeb (1997) and Masonis and Warren (2001) used top-of-atmosphere observations of solar radiation reflected from the high surfaces of Antarctica and Greenland to provide estimates of the calibration drift of the sensors for channels 1 and 2 on the Advanced Very High Resolution Radiometer (AVHRR). While their methods do not require a detailed *a priori* knowledge of the surface BRDF, such knowledge would help improve these techniques.

Many studies have provided estimates of either surface or top-of-atmosphere BRDF for various surface types. Here we present comprehensive measurements of the surface BRDF of Antarctic snow, and parameterizations that allow for the calculation of this BRDF for any viewing geometry, for wavelengths covering the solar spectrum from 350 to 2400 nm, and for solar zenith angles of 51° to 87°. These parameterizations are strictly applicable to the snow in the vicinity of Dome C, where the measurements were made, but given the homogeneity of the Antarctic Plateau surface, they can probably represent any region of the high plateau having low surface slope.

These measurements and parameterizations complement and extend numerous previous studies of the BRDF of snow. Several recent studies have investigated the BRDF of midlatitude, macroscopically-flat snow surfaces (Leroux et al. 1998; Aoki et al. 2000; Painter and Dozier 2004; Kokhanovsky et al. 2005). Those measurements all include only a few wavelengths or a limited range of solar zenith angles, and they exclude the effects of the macroscale surface roughness found on polar snow. However, they do examine the effect of changing snow type (grain size, grain shape, impurities), which we are unable to do because the snow at Dome C has

a relatively stable BRDF since it is always cold, fine-grained, and clean.

Other studies have focused on polar snow. Using a radiometer on an aircraft flying about 600 m above the surface, Arnold et al. (2002) measured the BRDF of Arctic scene types, including snow-covered sea ice and tundra, at wavelengths 470–2300 nm with solar zenith angles of about 65° for the snow-covered scenes. Li and Zhou (2004) compared modelling results with near-surface measurements of the BRDF of snow-covered late-summer Antarctic sea ice at 4 wavelengths for solar zenith angles of 65° and 85°.

The BRDF of snow on the Antarctic Plateau has been reported by Kuhn (1985) and Warren et al. (1998). Kuhn presented spectral measurements from the South Pole at 450, 750, and 1000 nm for a solar zenith angle of 67°, and broadband measurements from Plateau Station for solar zenith angles of 60° and 68°. Warren et al. reported measurements made at South Pole Station at 600, 660, and 900 nm with solar zenith angles from 67° to 89.3°. They examined the effect of the oriented surface roughness features, known as sastrugi, on the measurements and, concluding the effect was minimal at viewing zenith angles less than 50°, provided a parameterization for the BRDF valid for these viewing angles, for dry, fine-grained snow at visible wavelengths, with solar zenith angles in the measured range.

The present work extends the measurements of Warren et al. (1998) by covering a broader spectral interval and a wider range of solar zenith angles and by extending the parameterization to longer wavelengths and larger viewing zenith angles. The extension to larger viewing zenith angles was possible because the snow surface at Dome C is smoother than at South Pole, with significantly smaller sastrugi.

2.2 Reflectance Terminology

The angles necessary for the discussion of reflectance are illustrated in Figure 2.1. The solar zenith angle (θ_o) and viewing zenith angle (θ_v) are measured from the z-axis. The solar azimuth angle (ϕ_o) and the viewing azimuth angle (ϕ_v) are measured clockwise from north; the viewing azimuth is opposite the direction into which the detected light is travelling.

For most surfaces the BRDF does not depend separately on ϕ_o and ϕ_v, but instead only on the relative azimuth (ϕ), which we define as the angle measured clockwise from ϕ_o to ϕ_v. Using

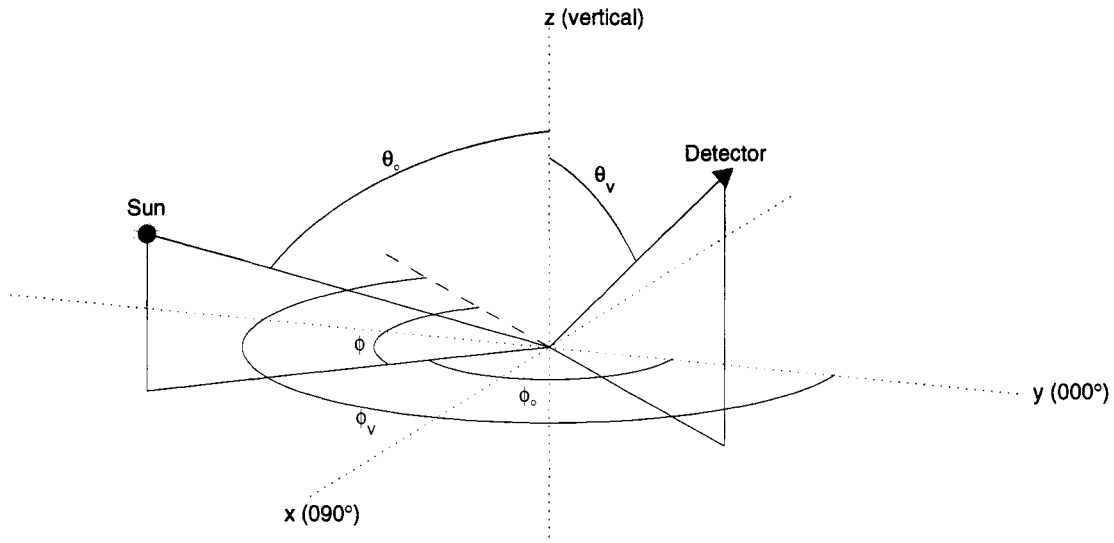

Figure 2.1: Definition of the solar zenith angle ($\theta_\circ$), the viewing zenith angle (θ_v), the solar azimuth angle ($\phi_\circ$), the viewing azimuth angle (ϕ_v), and the relative azimuth angle (ϕ).

this convention, a measurement made with the instrument pointed toward the azimuth of the sun corresponds to $\phi = 0°$, while a measurement made with the instrument pointed 90° to the left of the sun corresponds to $\phi = 270°$.

Warren et al. (1998) found this assumption, that ϕ can replace $\phi_\circ$ and ϕ_v, to be invalid at South Pole because of the alignment of the surface roughness features with the prevailing wind direction. However, because our measurements were made at a location with weaker and less directionally constant winds, ϕ appears to be sufficient to describe our observations.

One final geometrical definition is the principal plane, the plane containing the sun, the observer and the z-axis. The BRDF is usually symmetric across the principal plane, an observation we rely on in our data analysis.

The BRDF (ρ, sr^{-1}) is formally defined by Nicodemus et al. (1977) as the ratio of the radiance reflected into a particular direction (I_r, $\mathrm{W\,m^{-2}\,sr^{-1}\,\mu m^{-1}}$), to the incident flux ($F_\circ$, $\mathrm{W\,m^{-2}\,\mu m^{-1}}$), all of which is coming from a single direction:

$$\rho(\theta_\circ, \theta_v, \phi) = \frac{I_r(\theta_\circ, \theta_v, \phi)}{F_\circ(\theta_\circ)}. \tag{2.1}$$

This definition presents two difficulties for an observer working at the Earth's surface. First,

it is impossible to measure reflected sunlight with the incident light all coming from a single direction because of atmospheric scattering. Second, it is difficult to accurately measure the incident flux, especially for large solar zenith angles.

The existence of scattered light means that any observation made with sunlight as the source actually provides the "hemispherical directional reflectance factor", which has the same definition as BRDF except that the incident flux is from the entire hemisphere. Because of the strong wavelength dependence of Rayleigh scattering and the clean air over the Antarctic Plateau, our measurements at wavelengths longer than about 800 nm are essentially of the BRDF of snow, while those at shorter wavelengths, especially below 500 nm, are significantly influenced by diffuse light.

To avoid having to accurately measure the incident flux, we will report our BRDF observations in the form of the anisotropic reflectance factor (R), which was defined by Suttles et al. (1988) as π times the ratio of radiance reflected into a particular direction, to the reflected flux:

$$R(\theta_\circ, \theta_v, \phi) = \frac{\pi I_r(\theta_\circ, \theta_v, \phi)}{\int_0^{2\pi} \int_0^{\pi/2} I_r(\theta_\circ, \theta_v, \phi) \cos\theta_v \sin\theta_v \, d\theta_v \, d\phi}. \tag{2.2}$$

Multiplying by π sr makes this function nondimensional and ensures that its average value over the upward hemisphere, weighted by its contribution to the upward flux (proportional to $\cos\theta_v$), is unity:

$$\frac{1}{\pi} \int_0^{2\pi} \int_0^{\frac{\pi}{2}} R(\theta_\circ, \theta_v, \phi) \cos\theta_v \sin\theta_v \, d\theta_v \, d\phi = 1. \tag{2.3}$$

An isotropic (Lambertian) reflector has $R = 1$ at all angles.

The spectral albedo (α) is the ratio of reflected to incident flux as a function of wavelength (λ), and its values for snow on the Antarctic Plateau have been reported before (Grenfell et al. 1994), and we also measured similar values near our BRDF site. The albedo can be derived from the BRDF as

$$\alpha(\theta_\circ) = \int_0^{2\pi} \int_0^{\frac{\pi}{2}} \rho(\theta_\circ, \theta_v, \phi) \cos\theta_v \sin\theta_v \, d\theta_v \, d\phi, \tag{2.4}$$

which illustrates that R and ρ differ by a factor of $\frac{\pi}{\alpha}$:

$$R(\theta_\circ, \theta_v, \phi) = \frac{\pi}{\alpha} \rho(\theta_\circ, \theta_v, \phi). \tag{2.5}$$

2.3 Measurements

2.3.1 Location

All measurements reported in this paper were made at Dome C (75°06′S, 123°18′E, 3200 m MSL) during the summers of 2003–2004 and 2004–2005. This site was chosen because it is in the low-latitude part of the plateau, 15° from the pole, which allows measurements at a wide range of solar zenith angles each day, and because it is near a local maximum in ice-sheet elevation, which means winds there are generally lighter and less directionally constant than at other plateau sites because the surface slope at Dome C is extremely small. The lighter and more variable winds minimize the effect of surface roughness on the observations by creating smaller and less-aligned sastrugi. The latitude of 75° is seen frequently by most polar-orbiting satellites.

The observations were made from atop a 32-meter tower to ensure that the instrument's footprint was large enough to include a representative sample of the rough snow surface. A footprint that is too small may be dominated by a single, unrepresentative surface feature. The instrument's field of view has a diameter of 15°, and measurements were centered on viewing zenith angles of 22.5°, 37.5°, 52.5°, 67.5°, and 82.5°. The areas of the footprints at the first four angles were about 70, 110, 260, and 1170 m^2; the footprint at 82.5° extends to the horizon. Even the smallest of these footprints should contain multiple sastrugi.

The French and Italian Antarctic programs have been jointly operating a small summer research camp at Dome C since 1996. The last few years have seen the construction of a new, year-round base, which was first occupied during the winter of 2005. The tower on which we operated was erected in the summer of 2002–2003 in a previously undisturbed area. It is situated about 900 m WNW of the construction site for the year-round base, 1300 m WNW of the summer camp, and 1700 m WNW of the runway. Travel was forbidden inside a large region, providing us with an undisturbed snow surface over 255 degrees of azimuth, from $\phi_v = 142.5°$ clockwise to $\phi_v = 37.5°$. By the time we began BRDF measurements, in December 2003, all of the surface disturbances caused by the tower installation had been erased by 11 months of blowing and falling snow. Snow samples collected near our site had soot concentrations around 3 nanograms of carbon per gram of snow (ng g^{-1}) in the upper 0.2 m of snow (that which had fallen since the

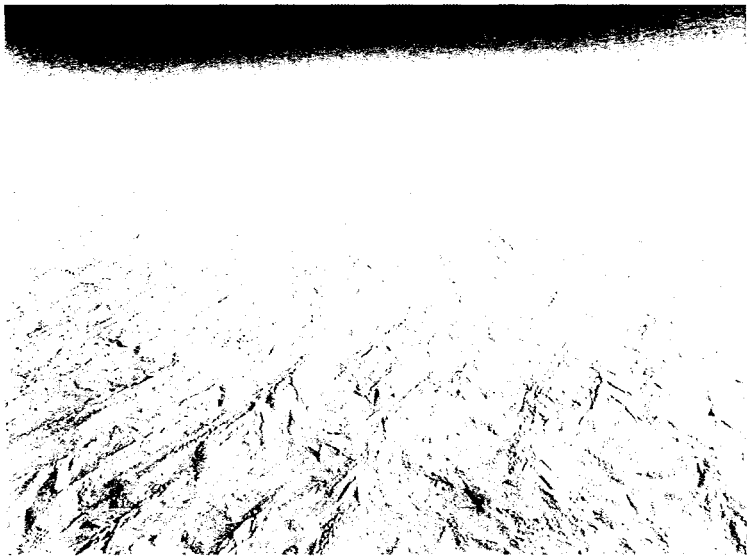

Figure 2.2: A photograph looking west from the top of the 32-m tower from which the BRDF measurements were made. The sun is in the north.

tower was installed), and about 1 ng g^{-1} in deeper snow (Warren et al. 2006). Warren and Clarke (1990) suggested a soot concentration of 3 ng g^{-1} would reduce the albedo at the most sensitive wavelength by less than 0.004, indicating that this level of contamination produces no significant impact on our observations.

Figure 2.2 shows the appearance of the snow surface to the west of the tower. A theodolite and leveling rod were used on several days to measure the surface elevation every 20 or 50 cm along numerous 20- to 35-meter lines in areas just outside our measurement domain. The standard deviation of these data was 2.3 cm, and the highest sastrugi were only 6 to 8 cm above the mean surface.

2.3.2 Equipment and Experimental Design

All radiance measurements were made using a FieldSpec Pro JR spectroradiometer manufactured by Analytical Spectral Devices, Inc. (hereinafter referred to as ASD). The ASD records the radiance every 1 nm from 350 to 2500 nm, with 3- to 30-nanometer spectral resolution (full width at half-maximum). More details about the ASD are given by Kindel et al. (2001).

The fiber optic input cable to the ASD was mounted in a baffle, limiting its field of view to a 15° cone. This baffle was then mounted on a goniometer, which allowed for accurate pointing in both the zenith and azimuth. The pointing of the goniometer was performed manually. The ASD and the laptop computer with which it interfaced were both kept at the top of the 32-meter tower inside heated boxes.

Each observation sequence involved recording the radiance coming from 85 different locations on the snow surface. Each of the 85 recorded measurements was an average of 10 of the ASD's spectral scans; each 10-scan average took less than three seconds to complete. An entire observation sequence, including positioning the goniometer to point at each location and driving the computer, took between 10 and 15 minutes to complete.

2.3.3 Generation of Anisotropic Reflectance Patterns

During each observation, measurements were made every 15° in both θ_v (22.5°, 37.5°, 52.5°, 67.5°, and 82.5°) and ϕ_v (150°, 165°, ..., 345°, 0°, 15°, and 30°). These points represent the locations that would be viewed by an infinitesimal field of view; the intersection of our 15° conical field of view with the surface creates an ellipse, with the two foci along a line extending in the direction of ϕ_v, from below the goniometer's location.

For planning purposes, observation sequences were centered on times when ϕ_o was a multiple of 15°. The local standard times at which the desired solar geometry would occur on each day were calculated using a program adapted by Warren Wiscombe from Michalsky (1988).

To ensure both that the incoming solar flux did not change significantly during an observation, and that no measurements were affected by shadows, observations were made only when the sky either was clear or contained very few clouds, all of which were thin and within a few degrees of the horizon.

Because the snow to the east of the tower was disturbed by buildings and foot and vehicle traffic, radiances could be measured from only about two thirds of the viewing azimuths during each observation sequence. In order to generate anisotropic reflectance functions, reflected radiances must be available from all azimuths to carry out the integral in the denominator of Equation 2.2. We chose one of the following two methods to complete each pattern, depending on the location

of the sun during the measurements.

For those observations that contain measurements at both $\phi = 0°$ and $\phi = 180°$, and therefore contain measurements at all azimuths on one side of the principal plane, we relied on the observation that the BRDF is approximately symmetric across this plane to allow us to complete the patterns by reflecting measurements across the principal plane [e.g., we set $R(\theta_\circ, \theta_v, \phi = 45°) = R(\theta_\circ, \theta_v, \phi = 315°)$ if we had measurements from $\phi = 180°$ clockwise to $\phi = 0°$]. Our available viewing geometry meant that this method was applied to observations with $\phi_\circ$ within 30° of 0° or 180°, which were those made during the period between about two hours before and after noon and midnight local time.

To complete patterns using observations made at other times, two separate observations, with equal solar zenith angles, but different solar azimuth angles, were combined. Observations made within about 36 hours of each other, with equal values of $|180° - \phi_\circ|$ have approximately equal solar zenith angles and could be combined. This method requires R to be a function only of the relative azimuth, and our measurements showed this to be a reasonable assertion. To make a complete pattern, measurements at each of the 24 relative azimuths must exist in at least one of the two observations. This was true of the correct combinations of observations made between about two hours before and after 0600 and 1800 local time.

When this method of stitching two partial patterns together is used, a scale factor must be applied to one of the patterns to account for small changes in atmospheric conditions and any changes in the instrument response. All observations that were stitched together contained at least 10 angles at which measurements were made in both observations. Ratios of these overlapping measurements provided numerous possible scale factors, from which one was chosen using the method described by Warren et al. (1998). Various methods to determine a single scale factor from the numerous overlapping measurements, including taking the mean or median of the possible factors and the method used by Warren et al., produced patterns with insignificant differences.

Once a complete pattern was available, the solar geometry was determined for the time of each of the 85 individual measurements. Each radiance measurement was then divided by the cosine of the solar zenith angle at the time of that measurement to account for variations in

reflected radiance caused by the small variation of θ_o during the time required for the complete observation. For a few of the measured directions, the field of view contains part of the tower's shadow. We therefore discarded the measurements at ($\phi = 180°$, $\theta_v < \theta_o + 7.5°$) and ($\phi = 165°$ and $\phi = 195°$, $\theta_v = 22.5°$) and replaced them with estimates determined by fitting a cubic spline to data from the neighboring backscattered azimuths at the same viewing zenith. No measurements were made closer to nadir than 22.5°. Radiances at all azimuths at $\theta_v = 7.5°$ were therefore set to the median of the measurements at $\theta_v = 22.5°$. The data were then interpolated to a fixed angular grid: every 7.5° in ϕ, beginning at 0°, and every 15° in θ_v, beginning at 7.5°. For the interpolation of the values in the shadow region and for the gridding process, the measurements were placed at their actual relative azimuth, as calculated for the time of each measurement, rather than at their nominal relative azimuths; the two differ slightly because of the roughly 3° to 4° change in ϕ_o during the observation sequence.

At this point we have a complete and consistent set of reflected radiance measurements. These are then normalized using Equation 2.2, providing the anisotropic reflectance functions that are used in the rest of this paper.

2.3.4 Experimental Uncertainties

Warren et al. (1998) discussed five major factors that affect the BRDF of snow: single-scattering phase function, solar zenith angle, snow grain size, absorption coefficient of ice, and surface roughness. Of these, only the solar zenith angle changes appreciably in the time required for an observation sequence. The micro-scale properties of the snow are relatively homogeneous around Dome C, but spatial variations of the surface roughness features can affect our observations.

Macroscopic surface roughness features can alter the BRDF of a surface. In general they will cause an observer facing the sun to see shadowed or shaded surfaces, thus reducing the magnitude of the forward reflectance peak. The roughness also increases the amount of backscatter by effectively reducing the solar zenith angle on roughness elements. The dimensions and orientation of the features determine how large this effect is.

Observation of the surface roughness features was not viewed as something to avoid because

they make our data appropriate for use on the high Antarctic Plateau. However, the surface roughness can introduce uncertainties into our observations in three ways: its effect may vary depending on the area of the observation footprint on the surface; the roughness can vary within our observation domain, producing different effects at different viewing angles; the roughness elements may have a preferred orientation, causing asymmetries across the principal plane.

As discussed in Section 2.3.1, the observations were made from the top of a tower to provide a large enough footprint to include a representative sample of surface roughness elements. Still, the area of the footprint does increase significantly as the viewing zenith angle increases. This increasing spatial averaging may affect our observations. We expect that this effect is likely to be small since the surface roughness mostly affects the BRDF at the largest viewing zenith angles (Warren et al. 1998), both of which have extremely large footprints, however, a rigorous assessment of this effect would require the use of a three-dimensional Monte Carlo radiative transfer model with the snow surface roughness features realistically described. Such modelling has not been carried out, and is beyond the scope of this paper. The potential effect of variations in R due to different amounts of spatial averaging should also be considered by those using surface and satellite observations together.

The measurements at each viewing angle observe different areas of the surface. This means there could be differences in the observed radiance field that are due to the observation of areas with different surface roughness features. Given the small size (relative to the footprint area) and random spatial distribution of the surface features seen in Figure 2.2, it is unlikely that any one footprint will fall on a truly unrepresentative area, especially at the larger viewing zenith angles, where the roughness has the greatest effect.

If the surface features have a preferred orientation, they can cause asymmetries across the principal plane, and this effect will vary depending on the orientation of the roughness features relative to the solar azimuth (Figure 5 of Warren et al. 1998). Since our methods of generating complete reflectance patterns assume that the reflectance is symmetric across the principal plane and that it is affected only by the relative azimuth angle, these roughness features may cause variations that we do not account for in our results.

The small size and variable orientation of the surface features at Dome C minimize these

sources of uncertainty. To estimate the magnitude of the error introduced into our analyzed patterns due to our assumption of symmetry across the principal plane, we calculated, for all observations used in the analyses, the relative difference between radiance measurements made during the same observation, with the same θ_v and with $|\phi|$ ($-180° < \phi \leq 180°$) within 4° of each other. These calculations do not isolate the effect of the assumption of symmetry; they will be affected by other sources of noise as well. At $\lambda \leq 1400$ nm the difference between such measurement pairs for all θ_o is generally less than 5%, and at longer wavelengths it is generally less than 10%. The largest differences occur at wavelengths with the lowest albedo, where the noise in the observations is greatest. These differences increase with θ_o but show no systematic variation with ϕ or θ_v. If these differences were entirely due to asymmetry across the principal plane caused by surface roughness then, from Figure 6 in Warren et al. (1998), we would expect the differences to increase with θ_v and to decrease with ϕ (away from the forward-scattering direction). That they do not suggests that they are influenced by other sources of noise as well.

Aside from factors that actually affect the BRDF of snow, other effects can introduce error into our measurements. These include errors introduced by variations in the amount of incoming flux, with either time or space, and those caused by instruments or observation methods.

During the field seasons we made BRDF observations only when it appeared they would be unaffected by clouds. It is possible that some errors will be introduced into the observations as a result of variations in downwelling fluxes due to subvisible clouds or boundary-layer ice crystals (diamond dust), a phenomenon too common to avoid completely. Diamond dust was present during about 25% of our observations. Variations in incoming flux due to changing solar elevation should be largely accounted for by our data processing.

Tests showed that the repeatability of radiance measurements made with the ASD was within ±2% over a 20-minute period, enough time for a complete set of measurements. Because R is normalized by the reflected flux, an absolute calibration was not necessary.

Small errors may have been introduced through inaccurate pointing of the goniometer. The goniometer was aligned in azimuth with reference to the shadow of the tower together with the equation of time for that day; it was leveled with a manufacturer-installed bubble level on its base. We estimate that our installation and pointing were accurate to within ±2° in both zenith

and azimuth.

It is impossible to estimate with a high degree of confidence the combined uncertainty from these numerous potential sources. Comparisons of separate analyzed patterns with solar zenith angles that differ by less than 1° suggest that the overall uncertainty is within ±3% at $\lambda <$ 1400 nm with small $\theta_\circ$ ($\lesssim 60°$), ±8% at longer wavelengths with small $\theta_\circ$, ±6% at $\lambda < 1400$ nm with large $\theta_\circ$ ($\gtrsim 70°$), and ±15% at longer wavelengths with large $\theta_\circ$. In general, uncertainty is larger at wavelengths with low albedos and in observations made with large solar zenith angles. Both of these situations reduce the amount of light reaching the detector, which may cause a lower signal-to-noise ratio, but probably more important is that both also significantly increase the anisotropy of the snow BRDF and its sensitivity to variations in grain radius. Uncertainty is also larger at longer wavelengths because of the increased anisotropy of the reflected radiation due to the lack of diffuse downwelling radiation. Increased anisotropy enhances the effect of small pointing errors.

2.4 Results

2.4.1 Observations

A few examples of the patterns of R resulting from our data analysis are shown in Figures 2.3 and 2.4. These polar plots show contours of the value of R as a function of θ_v (distance from center) and ϕ (angle clockwise from top) for various wavelengths and solar zenith angles.

Figure 2.3 shows examples of R measured at two wavelengths with contrasting albedos: 600 nm ($\alpha \approx 1.0$) and 1800 nm ($\alpha \approx 0.3$), for high, middle, and low solar elevations. These observations will be compared later with results of the parameterizations. Figure 2.4 shows R measured at 2000 nm (very low albedo; $\alpha < 0.1$) for high and low solar elevations.

These figures illustrate the two main features of the data: the snow is brightest when viewed near the horizon, in the direction of the solar azimuth, darkest when viewed near nadir, opposite the solar azimuth; and this anisotropy increases with increasing solar zenith angle and decreases with increasing albedo. The upper-left panel of Figure 2.3 is typical of the observations that are nearly isotropic.

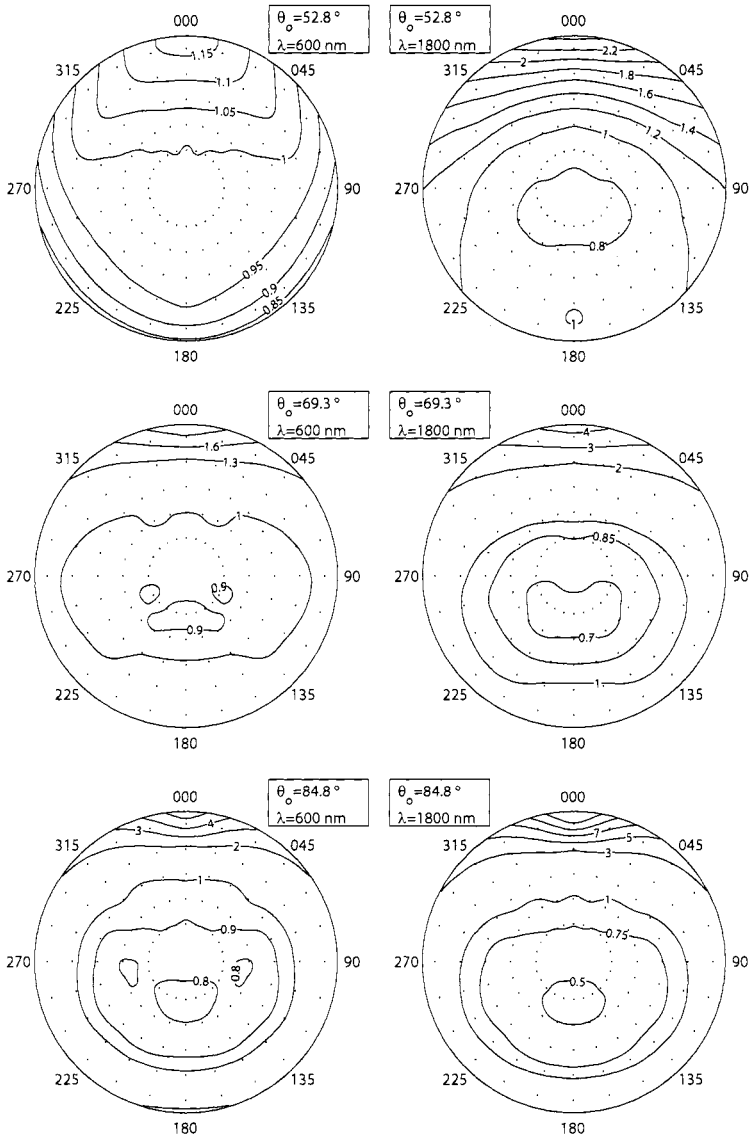

Figure 2.3: Polar contour plots of the anisotropic reflectance factor (R) of snow at Dome C measured under three different solar zenith angles at two different wavelengths (λ). Dots are placed every 15° in both viewing zenith angle, starting at 22.5°, and relative azimuth angle, starting at 0°, which indicates light coming from the azimuth containing the sun. The contour interval for $R < 1$ sometimes differs from that for $R > 1$.

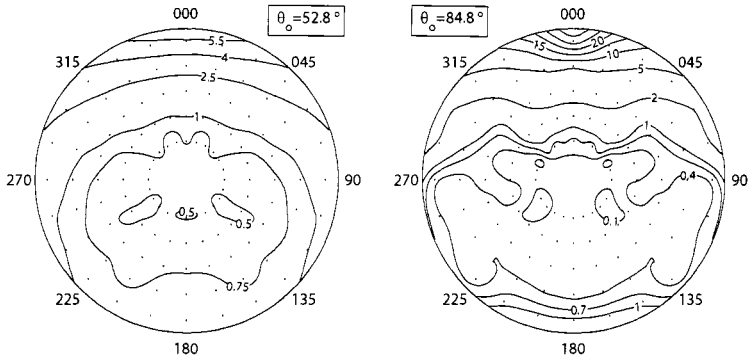

Figure 2.4: Polar contour plots of R measured at a wavelength of 2000 nm under two different solar zenith angles. Note that the contour interval is not constant.

During the two summers of observations we collected data to create 96 complete patterns of R, at solar zenith angles from 51.6° to 86.6°. Subsequent analysis revealed that the data at $\lambda > 2400$ nm were unreliable due to a low signal-to-noise ratio, so the analysis covers wavelengths from 350 to 2400 nm. Given the volume of data collected, we cannot present them all here, so those in Figures 2.3 and 2.4 were chosen as representative examples. More of the data can be viewed on our website (`http://www.atmos.washington.edu/~sgwgroup/DC/brdfPaper.html`). The values of R at the gridded angles are available there at any of the 96 measured solar zenith angles at 25-nanometer intervals for wavelengths between 350 and 2400 nm.

2.4.2 Parameterization

With such a large set of data available, we hoped to be able to develop and present a parameterization that could be used to predict R for any solar zenith angle and wavelength within the range we observed. The data proved too variable to allow for a single parameterization to accurately describe them all. However, by separating the data into a few groups, based on wavelength or albedo, solar zenith angle, and, sometimes, viewing zenith angle, it was possible to develop multiple parameterizations that fit the data with reasonable accuracy. These separate parameterizations cover most of the range of wavelengths and solar zenith angles observed, but some of the most extremely anisotropic cases, those with very low albedo, are not covered.

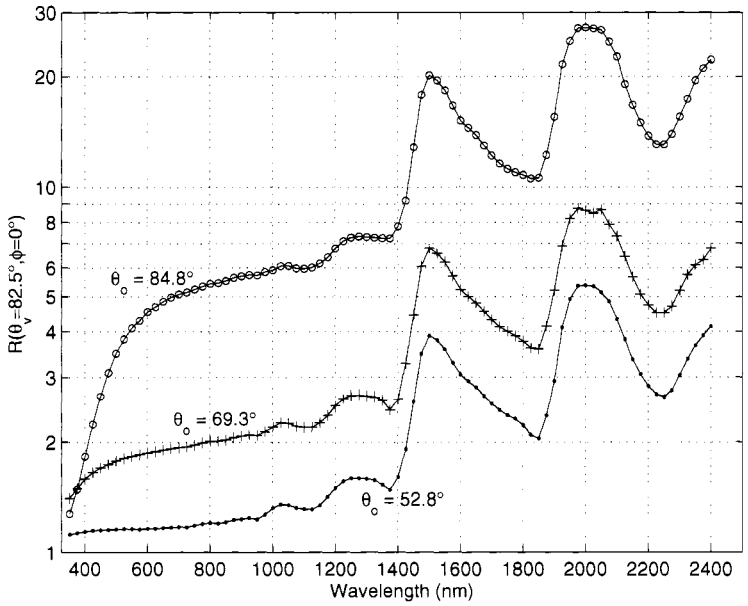

Figure 2.5: Values of R measured at the forward reflectance peak, as a function of wavelength, for three different solar zenith angles.

In this section we will first show how the data vary with wavelength, albedo, and solar zenith angle, and discuss why the parameterizations use the predictors they do and how we divided the data. After that we will explain the functions used in the parameterizations, and how these parameterizations were developed. Finally we show selected results from the parameterizations.

Variation of R with θ_o, λ, and α

The values of R at $(\theta_v = 82.5°, \phi = 0°)$ as a function of wavelength are shown in Figure 2.5 for observations at three different solar zenith angles. We present R at the forward reflectance peak because it is a good indication of the anisotropy of the overall pattern. We will abbreviate $R(\theta_v = 82.5°, \phi = 0°)$ as R_f. From Figure 2.5 we can see that the anisotropy does not increase monotonically with wavelength. At wavelengths longer than about 1000 nm the anisotropy varies with wavelength in a way that may seem erratic.

One feature in Figure 2.5 that may seem unusual is the crossing of the curves for the two larger solar zenith angles at $\lambda = 375$ nm. This feature is the result of the varying amount of

diffuse light incident on the snow. Diffuse incident flux acts to reduce the anisotropy of the reflected light: if the incident flux were isotropic, then there would be no forward direction into which light could be preferentially scattered. As the sun descends toward the horizon, the fraction of the incident flux that has been scattered out of the direct beam increases. This effect is larger at shorter wavelengths, where Rayleigh scattering is most effective. This combination is enough, in the ultraviolet region, to overcome the usual pattern of increasing anisotropy with solar zenith angle.

Of the five factors listed in Section 2.3.4 that affect the BRDF of snow, the single-scattering phase function and the absorption coefficient of ice both vary with wavelength. For a given grain radius and solar zenith angle, the albedo of the snow is largely determined by these two factors, suggesting that R, under direct-beam illumination, should be the same at any wavelengths at which snow has the same albedo.

The albedo of the snow at Dome C was measured one evening when clouds were thick enough to fully obscure the solar disk so that all incident flux was diffuse. Having only diffuse light incident on the snow greatly reduces the magnitude of errors that are introduced by small deviations from level of either the surface or the instrument. Figure 2.6 shows the albedo measured that evening, as a function of wavelength. The measured albedo at Dome C closely resembles that measured at the South Pole (Grenfell et al. 1994). Comparing Figures 2.5 and 2.6 supports the suggestion that albedo may be a better predictor of R than wavelength since the maxima of R_f are located near the minima of α.

A plot of R_f versus α, shown in Figure 2.7, confirms that this relationship is much more systematic than that shown in Figure 2.5. Figure 2.7 was created by plotting the values of R_f observed every 25 nm during three different observations (corresponding to the three solar zenith angles) versus the albedo from Figure 2.6 at that wavelength, so it shows the clear-sky R_f versus the diffuse (overcast) albedo. This plot shows a very good power-law relationship between the anisotropy of the reflected light and the albedo of the snow at albedos between about 0.15 and 0.95. The failure of the relationship at low albedos may result from noise due to the very small amounts of reflected light at these wavelengths, or it may represent variability caused by some other factor we have not considered here. At high albedos the relationship fails because these

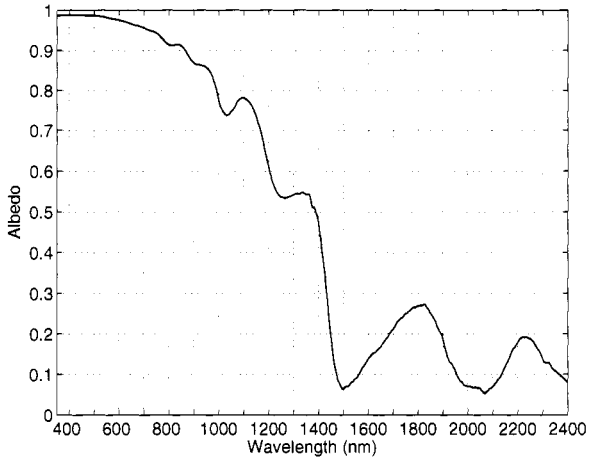

Figure 2.6: Spectral albedo of the snow surface at Dome C, measured between 2300 and 2330 LST 30 December 2004 under an overcast sky with the direct solar beam fully obscured. Five observations were averaged, and this average was then smoothed using an 11-nanometer running mean at $\lambda \leq 1825$ nm and a 101-nanometer running mean at larger wavelengths, where extremely low fluxes resulted in a low signal-to-noise ratio.

albedos occur in the visible and ultraviolet, where Rayleigh scattering causes a significant amount of diffuse downwelling radiation. A similar approach using clear-sky albedo might work as well as or better than using the diffuse albedo, but would require using a different spectral albedo for each solar zenith angle. However, the sorting of wavelengths according to their albedos will be nearly the same for all zenith angles, judging from Figure 11a of Wiscombe and Warren (1980), so Figure 2.7 would likely remain unchanged.

We considered the imaginary index of refraction of ice (m_{im}) as a predictor, rather than albedo, but chose to use albedo for two reasons. A plot, similar to Figure 2.7, of R_{f} versus m_{im} (not shown) showed that this relationship did not follow a simple functional form. Also, the albedo incorporates the variation of the single-scattering phase function with λ, and will allow the parameterization to be used for snow with different grain sizes than the snow at Dome C. If a user of the parameterization wishes to apply it to snow with larger grains, and therefore lower albedo in the near-infrared, the different grain size can be accounted for by using an estimate of the albedo of the snow of interest rather than the measured albedo of the snow at Dome C (Figure 2.6).

Figure 2.7 shows that wavelengths with the same albedo have the same forward peak, but

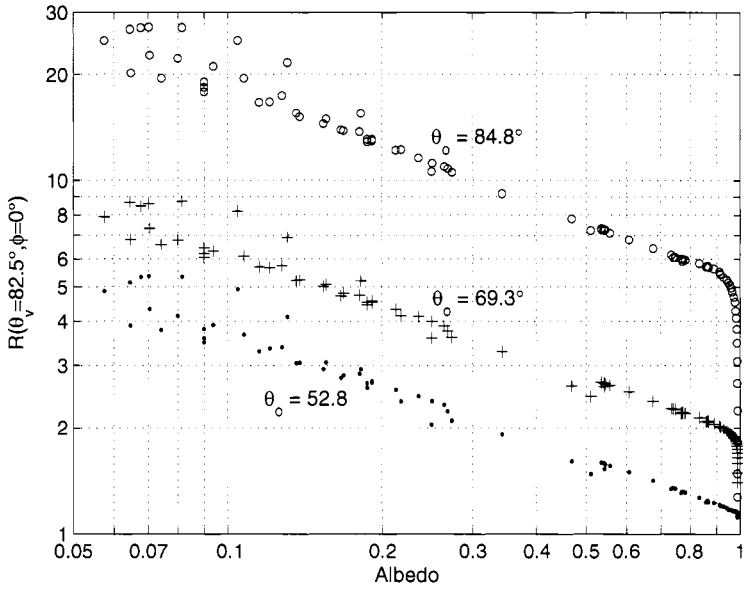

Figure 2.7: Values of R measured at the forward reflectance peak, as a function of albedo, for three different solar zenith angles.

do their BRDFs also agree at other angles? To answer this, complete angular patterns of R were compared at wavelengths with the same albedo. The patterns observed at 1450 nm and 2250 nm ($\alpha = 0.187$ at both wavelengths) show maximum differences of 8% with $\theta_o = 60°$ and 12% with $\theta_o = 80°$, and both differ by less than 6% at nearly all viewing angles. Similar small differences were found between the observed patterns at other pairs of wavelengths with equal albedos. In contrast to these small differences, observed patterns at the nearby wavelengths of 1400 nm ($\alpha = 0.47$) and 1450 nm ($\alpha = 0.19$) differ by up to 60%.

Based on results shown above, we chose to consider three wavelength regions. At short wavelengths, 350 to 950 nm, where Rayleigh scattering may affect our measurements and albedo varies smoothly with wavelength, we chose to use wavelength as a predictor in the parameterization. At longer wavelengths, we chose to use the albedo shown in Figure 2.6 as the predictor. We split the longer wavelength region into one from 950 to 1400 nm, where the albedo is intermediate, and another from 1450 to 2400 nm, where the albedo is low. We further limited this latter region by excluding wavelengths at which $\alpha < 0.15$. This last restriction means the regions

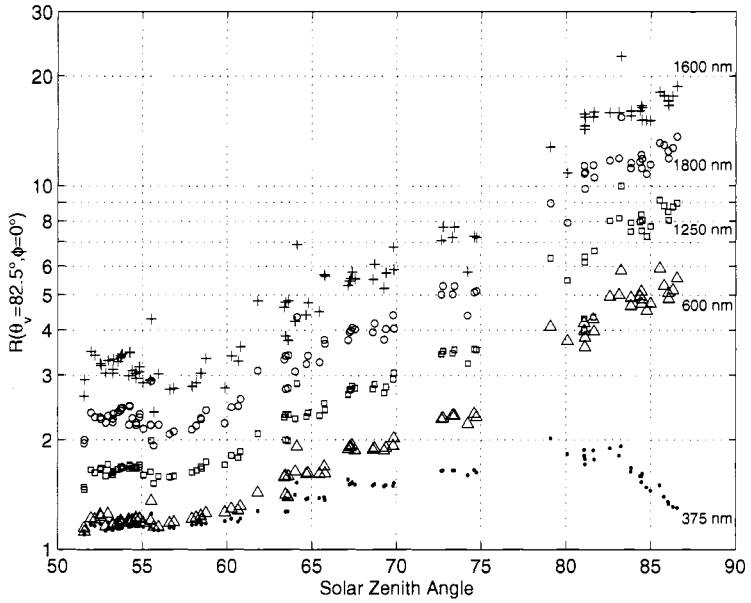

Figure 2.8: Values of R measured at the forward reflectance peak, as a function of solar zenith angle, for five wavelengths: 375 nm, dots; 600 nm, triangles; 1250 nm, squares; 1600 nm, crosses; and 1800 nm, circles.

near 1500, 2000, and 2400 nm (e.g. Figure 2.4) are not included in the parameterizations. Data between 1400 and 1450 nm were also not included because α varies so rapidly with wavelength in this region. Data at wavelengths not included in the parameterizations are available online (`http://www.atmos.washington.edu/~sgwgroup/DC/brdfPaper.html`).

The other necessary predictor in the parameterizations is the solar zenith angle. The variation of R_f with θ_o is shown for several wavelengths in Figure 2.8. This figure shows that at most wavelengths the anisotropy is nearly independent of θ_o for $\theta_o \lesssim 60°$, then increases with θ_o, at an increasing rate as θ_o increases. Again, the relationship is different at short wavelengths ($\lambda = 375$ nm), where the great reduction in the direct/diffuse ratio as the sun approaches the horizon leads to decreased anisotropy.

Separate parameterizations were developed for high and low sun. The primary parameterization for each of the three wavelength regions is for $\theta_o \leq 75°$. Parameterizations for $\theta_o \geq 70°$ were developed for the two shorter wavelength regions; an accurate parameterization for the low-sun data at long wavelengths could not be developed because of their more extreme anisotropy,

Table 2.1: Summary of the data included in and the root-mean-squared relative errors of the six parameterizations. The errors given for parameterizations E and F in the "All θ_v" column are for all angles included in the parameterization.

	Data Included in Parameterizations				RMS Error	
Parameterization	λ (nm)	θ_o	α	θ_v	All θ_v	$\theta_v \leq 52.5°$
A	350–950	51.6°–75°	n/a	0°–82.5°	2.3%	1.9%
B	350–950	70°–86.6°	n/a	0°–82.5°	3.7%	3.0%
C	950–1400	51.6°–75°	0.47–0.86	0°–82.5°	3.5%	2.7%
D	950–1400	70°–86.6°	0.47–0.86	0°–82.5°	4.1%	3.7%
E	1450–2400	51.6°–75°	0.15–0.28	0°–52.5°	5.6%	5.6%
F	1450–2400	51.6°–75°	0.15–0.28	52.5°–82.5°	7.9%	n/a

seen in the lower-right plot in Figure 2.3. The high- and low-sun parameterizations overlap for $70° \leq \theta_o \leq 75°$. This was done so that the low-sun parameterizations would be valid through the gap in our data between 75° and 79° (seen in Figure 2.8). In the region where both parameterizations are valid, the one for $\theta_o \leq 75°$ works better.

There was one final separation of the data necessary to develop accurate parameterizations. The long-wavelength data were separated into large and small viewing zenith angles at $\theta_v = 52.5°$; this angle is included in both. These two parameterizations produce nearly equal results at $\theta_v = 52.5°$ (the RMSE at 52.5° is 5.8% for the $\theta_v \geq 52.5°$ parameterization and 6.1% for the $\theta_v \leq 52.5°$ parameterization).

There are six groups of data to be parameterized, summarized in the first five columns of Table 2.1; the last two columns of the table will be discussed later.

Parameterization Development

Rather than use predefined functional forms to describe the data, such as Fourier series, which would require many terms to capture the more extreme anisotropy that exists in some of the data,

we chose to use the empirical orthogonal functions (EOFs) of the data. The EOFs are a set of orthonormal functions determined by performing a singular value decomposition of the data matrix. These functions are ordered such that the first one is the pattern that describes a larger fraction of the variance in the data than any other EOF, and the second is the function, orthogonal to the first that can describe more of the remaining variance than any other, and so on. The advantage of EOF analysis is that most of the significant variance in a data set can be represented with just the first few EOFs, making them ideal for use in our parameterizations.

Here we will work through a specific example of how this procedure was used to develop a parameterization. We use the subset of data that includes $\lambda \leq 950$ nm, $\theta_o \leq 75°$. This subset includes 71 observations at different solar zenith angles. For the development of the parameterizations, data at wavelengths that are integer multiples of 25 nm were used, meaning that this subset includes patterns of R at 25 wavelengths (350, 375, 400, ...,950 nm). So, there are $71 \times 25 = 1775$ different patterns included in the development of this parameterization. Each pattern contains the values of R gridded at 288 angular locations (6 viewing zenith angles and 48 viewing azimuth angles). Combining these numbers gives us a data matrix ($\mathbf{R}$) that has 1775 columns and 288 rows; each column contains all of the gridded values of R for one pattern, in some specified order, which is constant across all columns.

A technical-computing software package (Matlab) was used to compute the singular value decomposition of the data matrix minus one, decomposing the data into three matrices such that:

$$\mathbf{R} = \mathbf{1} + \mathbf{U}\mathbf{\Sigma}\mathbf{V}^{\mathrm{T}}, \tag{2.6}$$

where $\mathbf{1}$ is a 288×1775 matrix of ones. The EOFs are contained in the columns of $\mathbf{U}$, a 288×288 matrix (there are 288 rows because the EOFs are defined at the same grid points as the data, and there are 288 columns because there are as many spatial EOFs as there are spatial grid points). The first and second EOFs (the first and second columns of $\mathbf{U}$) are contoured in Figure 2.9.

The first column of $\mathbf{V}$, a 1775×288 matrix, contains the coefficients that multiply the first EOF to make each of the 1775 patterns. The second column of $\mathbf{V}$ are the coefficients that multiply the second EOF, and so on. The third matrix in Equation 2.6, $\mathbf{\Sigma}$, is a 288×288 matrix with positive scale factors on its diagonal, and zeros elsewhere. The values on the diagonal of $\mathbf{\Sigma}$ are in decreasing order, and are related to the amount of variance represented by each EOF.

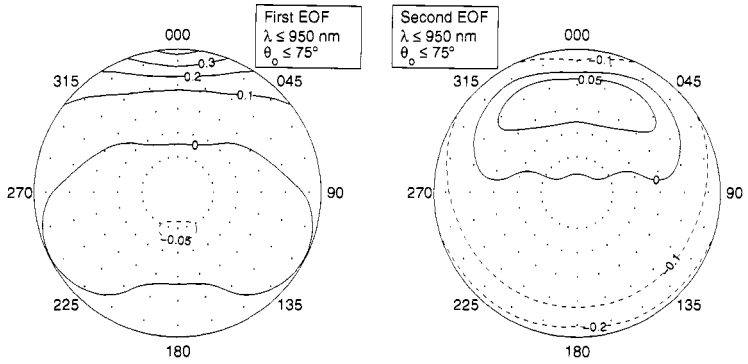

Figure 2.9: Polar contour plots of the first and second EOFs used in parameterization A. Contours of negative values are dashed.

While the singular value decomposition initially increases the number of values needed to describe the data from $288 \times 1775 = 511,200$ to $288 \times 288 + 288 + 1775 \times 288 = 594,432$ (ignoring the off-diagonal elements of $\mathbf{\Sigma}$), the power of the decomposition comes from the ability to recover the important aspects of the data with just the first few columns of $\mathbf{U}$, $\mathbf{\Sigma}$, and $\mathbf{V}$, thus greatly reducing the volume of data. In this case, the first two columns ($288 \times 2 + 2 + 1775 \times 2 = 4128$ values) contain enough information to describe nearly 98% of the variance in the full data set, and they are all that are used in the parameterization. Excluding the higher-order EOFs not only reduces the size of the data set, but also removes much of the noise from it.

Now, rather than parameterizing R as a function of $\theta_\circ$, λ (or α), θ_v, and ϕ, we separately parameterize the values in the first and second columns of $\mathbf{V}$ (we refer to these values as v_1 and v_2) as functions of $\theta_\circ$ and, in this case, λ. These coefficients can be represented with fairly simple functions. The form of these functions and the method used to optimize them is discussed below. Figure 2.10 shows the results of the parameterization of v_1 for this example. The left panel shows contours of the actual coefficients matching the measured R-patterns, smoothed with running means in both dimensions, and the results of the parameterization for these coefficients are contoured on the right. The parameterizations were fit to the unsmoothed coefficients.

Now, v_1 and v_2 can be calculated for any wavelength and solar zenith angle in the valid range for this parameterization. Once they are calculated, they can be used to calculate the values of R at the 288 grid points by using Equation 2.6, in which $\mathbf{U}$ is now a 288×2 matrix, with the first

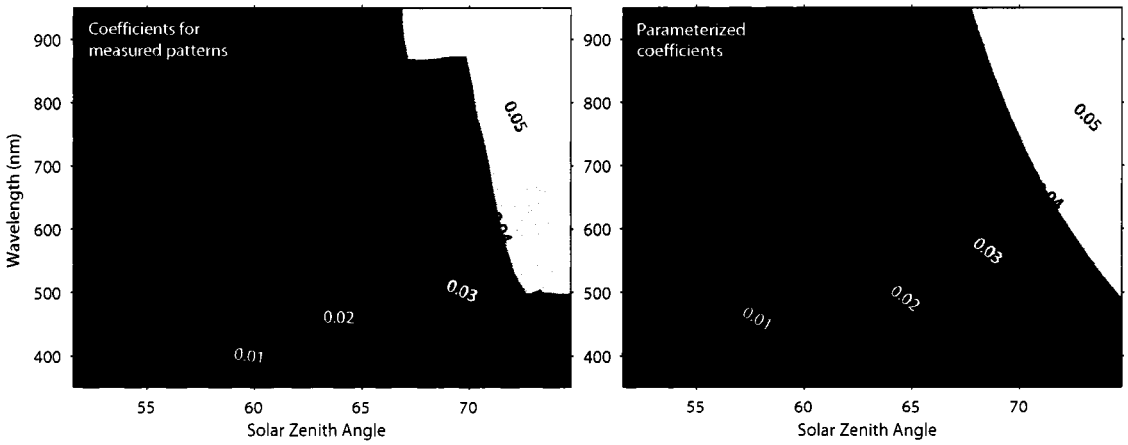

Figure 2.10: Contour plots of the coefficients multiplying the first EOF of the data in parameterization A. The coefficients fitting the measured data are shown on the left plot, where they have been smoothed with 2.5° and 50-nanometer running means. The parameterized coefficients are shown on the right.

two previously determined EOFs in its columns, $\mathbf{\Sigma}$ is a 2×2 matrix, with the first two previously determined scale factors on its diagonal, and $\mathbf{V}$ is the 1×2 matrix, $[v_1\ v_2]$. If the user calculates v_1 and v_2 for multiple combinations of $\theta_\circ$ and λ, multiple patterns of R can be calculated by adding more rows to the matrix $\mathbf{V}$. For an arbitrary viewing angle within the defined limits but not on the grid, one must determine R by interpolation.

This process was repeated for each of the six groups of data to be parameterized. The number of EOFs retained was decided by considering three factors: the amount of variance each EOF described, the form of each EOF (an EOF that does not show some reasonable structure is likely representing noise), and the variability of the coefficients in $\mathbf{V}$ for each EOF with $\theta_\circ$ and λ or α (if the coefficients do not show a systematic variation with at least one of the independent variables then it is likely that the EOF is representing noise). No hard rules were used to determine the cut off, but the appropriate number was generally obvious based on the above criteria. If there was any doubt about whether to include another EOF, the decision was made based on whether its inclusion improved the results. The first two EOFs were used (and, therefore, v_1 and v_2 were parameterized) for parameterizations A, B, C, and F (see Table 2.1 for definitions of these labels). Parameterization D required the first three EOFs, while parameterization E required only

the first EOF. In all cases the EOFs that were retained describe more than 97% of the variance in the data set. All 12 EOFs that are used in these parameterizations are available as delimited ASCII files with the supplementary material available on our website: `http://www.atmos.washington.edu/~sgwgroup/DC/brdfPaper.html`.

For each parameterization, the necessary values in $\mathbf{\Sigma}$ and the equations to calculate the necessary elements of $\mathbf{V}$ are presented in Table 2.2. After looking at contour plots of the coefficients in $\mathbf{V}$ for the various groups of data, we decided on the following functional form for the parameterization of those values:

$$v = c_1 + c_2\mu_\circ^{c_3} + c_4\lambda^{c_5} + c_6(\mu_\circ\lambda)^{c_7}, \tag{2.7}$$

where $\mu_\circ \equiv \cos(\theta_\circ)$. The function `nlinfit`, part of Matlab's Statistics Toolbox, was used to find the optimum values of c_i in a least-squares sense. This optimization was also attempted while leaving out various terms in Equation 2.7, and only those terms in the equations that improved the results were retained. Therefore the exact form of the equations shown in Table 2.2 varies.

Parameterization Results

The last two columns of Table 2.1 show the root-mean-squared relative error (RMSE) for each of the parameterizations. When possible, two RMSEs are given, one for the entire parameterization, and another calculated only for $\theta_v \leq 52.5°$, which are the viewing angles most likely to be used for remote sensing. The errors shown in Table 2.1 are in line with the estimated uncertainties in the data, discussed in Section 2.3.4. The magnitude of the error does not vary significantly across each parameterization's valid range of solar zenith angles or wavelengths.

Figure 2.11 shows the calculated values of R corresponding to the five observations shown in Figure 2.3 that are covered by the parameterizations. The plots on the right side of Figure 2.11 were created by combining the two parameterizations for long wavelengths. Comparing the plots in this figure to those in Figure 2.3 shows that the parameterizations accurately represent the main features seen in the data.

The errors in Figure 2.11, relative to the data in Figure 2.3, are shown in Figure 2.12. These plots show that the largest errors are often found at large viewing zenith angles, especially in the forward-scattering direction.

Table 2.2: The equations for the coefficients in $\mathbf{V}$ and the scaling factors in $\mathbf{\Sigma}$ for each parameterization (A–F, see Table 2.1 for definitions of the different parameterizations). Note that $\mu_\circ \equiv \cos\theta_\circ$. The final column gives the percentage of the variance in the dataset that is described by the EOFs that are included in each parameterization.

	Equation for v_x	$\mathbf{\Sigma}_{x,x}$	Variance
A	$v_1 = -0.0258 + 1.34\mu_\circ^{10.1} + 0.181\lambda^{0.519} - 0.206(\mu_\circ\lambda)^{0.608}$	75.6	97.7
	$v_2 = 0.105 - 0.0365\mu_\circ^{-1.01} - 0.00730\lambda^{-1.63} + 4.94\times10^{-5}(\mu_\circ\lambda)^{-2.86}$	24.2	
B	$v_1 = -0.784 + 1.35\mu_\circ^{-0.0872} - 0.399\lambda^{0.251} - 0.213(\mu_\circ\lambda)^{-0.284}$	217	99.4
	$v_2 = 1.90 + 1.39\mu_\circ^{1.32} - 0.0671\lambda^{-1.11} - 2.43(\mu_\circ\lambda)^{0.101}$	17.9	
C	$v_1 = -0.0623 - 7.98\times10^{-5}\alpha^{-5.99} + 0.0519(\mu_\circ\alpha)^{-0.454}$	121	98.2
	$v_2 = 0.0902 - 0.0349\mu_\circ^{-1.07}$	23.9	
D	$v_1 = -0.195 - 0.000372\mu_\circ^{-1.67} + 0.0569\alpha^{0.369} + 0.118(\mu_\circ\alpha)^{-0.216}$	289	99.7
	$v_2 = 1.75 - 0.132\mu_\circ^{-0.592} + 0.179\alpha^{3.11} - 1.91(\mu_\circ\alpha)^{0.146}$	21.8	
	$v_3 = 0.644 + 1.92\mu_\circ^{1.12} - 0.0221\alpha^{-2.82} - 1.61(\mu_\circ\alpha)^{0.298}$	16.8	
E	$v_1 = 0.106 - 0.124(\mu_\circ\alpha)^{0.193}$	129	98.0
F	$v_1 = 0.0161 - 0.0103(\mu_\circ\alpha)^{-0.599}$	301	99.0
	$v_2 = -0.151 + 0.0850\mu_\circ^{-0.679}$	36.8	

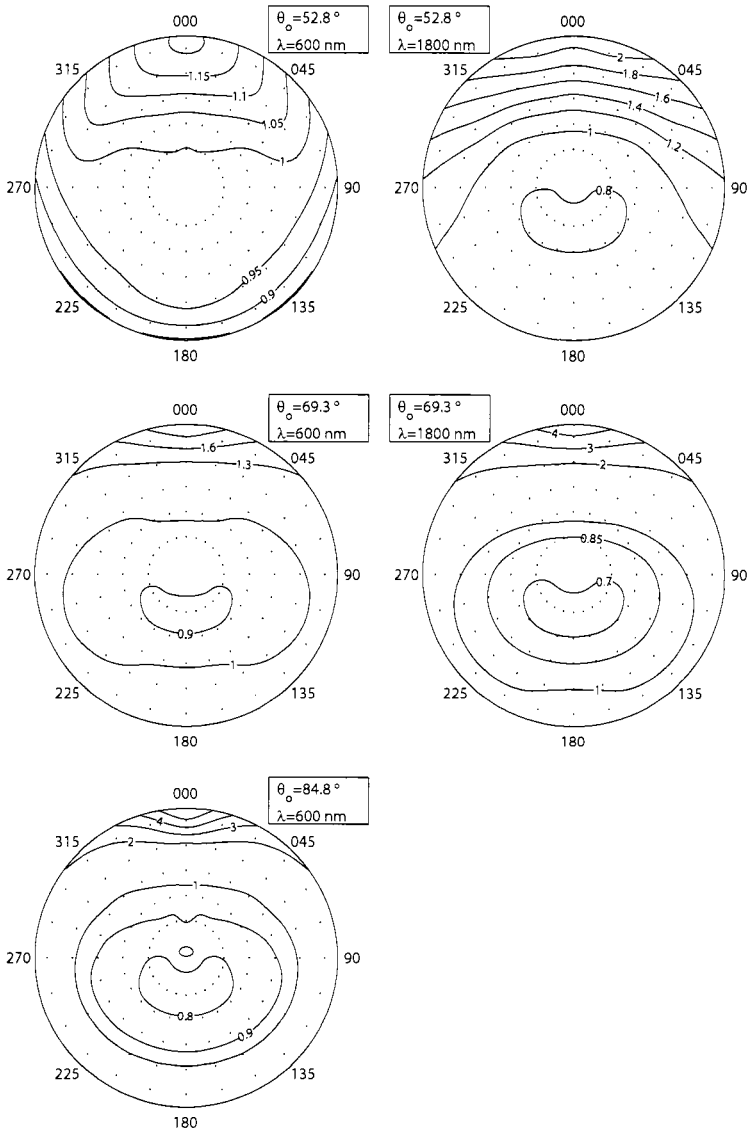

Figure 2.11: Polar contour plots of R, calculated with the parameterizations for five of the six observations shown in Figure 2.3. The sixth observation in Figure 2.3 is not covered by any of our parameterizations. The contour interval sometimes changes at 1.

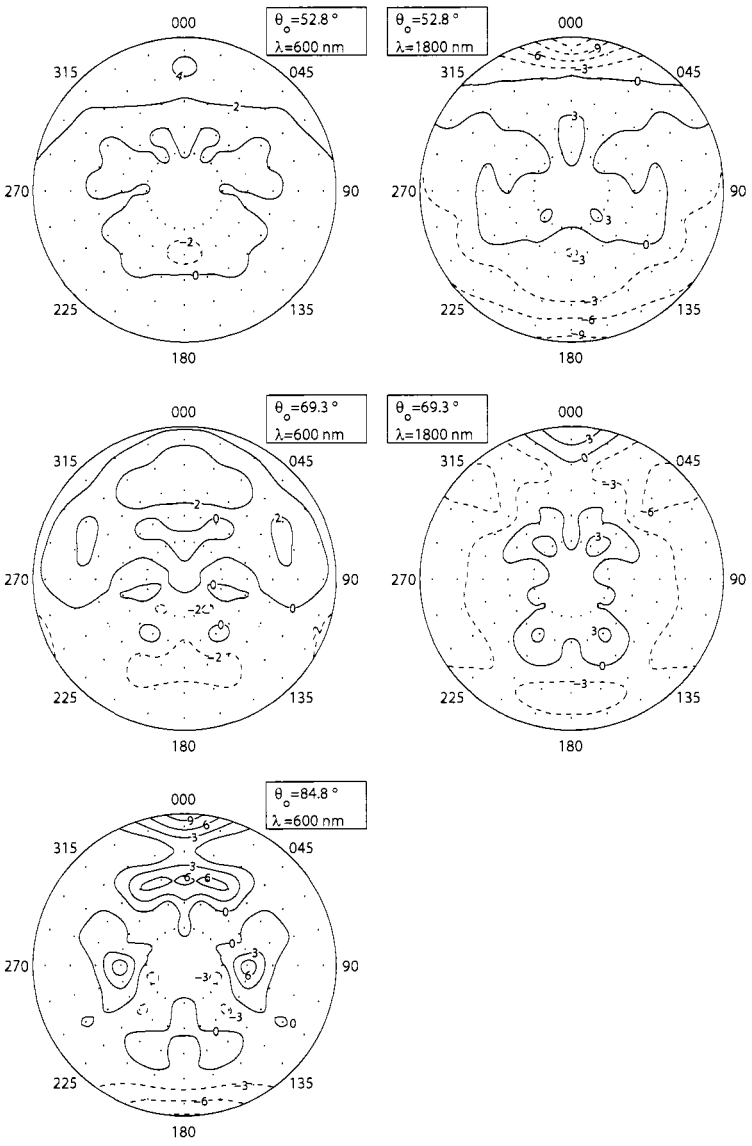

Figure 2.12: Polar contour plots of the relative error (%) of R, calculated with the parameterizations for five of the six observations shown in Figure 2.3. The sixth observation in Figure 2.3 is not covered by any of our parameterizations. Contours of negative values are dashed and indicate angles at which the parameterized R is less than the observed R.

No normalization requirement was placed on the parameterization results, so the patterns they predict do not necessarily satisfy Equation 2.2. This deviation from the correct normalization will introduce a small error when converting radiance measurements to albedo. For the parameterized patterns, the left hand side of Equation 2.2 is between 0.993 and 1.01 for parameterizations A and B, 0.996 and 1.005 for parameterizations C and D, and 0.985 and 1.02 for the combination of parameterizations E and F.

Parameterization Uncertainties

In Section 2.3.4 we considered factors that could introduce errors and noise into any of our individual analyzed reflectance patterns. Here we consider factors that may lead to variation in the reflectance pattern of the snow surface between our observations, and discuss how they might affect the parameterizations.

Of the five factors listed in Section 2.3.4 that affect the BRDF of snow, the parameterizations account for one directly and a second indirectly. The solar zenith angle is one of the independent variables in our parameterizations. The second independent variable is wavelength or albedo; this second independent variable accounts for variations in the absorption coefficient of ice, among other things. The other factors given above are not directly accounted for in our parameterizations and will introduce some level of uncertainty.

Grain-size variations during the two summers are a possible source of uncertainty in the parameterization. An increase in grain size primarily affects the BRDF of snow through two mechanisms: the asymmetry parameter (g) is increased (Wiscombe and Warren 1980), and the path length through ice between scattering events at air-ice interfaces is increased. Both of these effects increase the anisotropy of the BRDF pattern, strengthening the forward reflectance peak of the snow. Frequent observations of the surface snow showed that it was composed of grains with approximate radii between 50 and 100 μm, and that the range of sizes did not vary much during the field seasons. This size range is typical of the Antarctic Plateau, and the small magnitude of the variations minimizes the uncertainty they cause. Measurements of spectral albedo made on two traverses from Dome C to the coast at 67°S showed that the effective grain size was constant from latitude 75°S (Dome C) to latitude 68°S (Brandt and Warren, in preparation).

Variations in the single-scattering phase function of the snow grains can be examined by looking at variations in g. As mentioned above, g increases with grain size; it is also a function of wavelength. Its dependence on wavelength will be accounted for in the parameterizations through their dependence on wavelength and albedo. Its variation with grain size will introduce uncertainty into our parameterizations because we do not account for grain-size variations. This uncertainty will be small at wavelengths shorter than 1000 nm, where g varies little with grain size (Figure 4 of Wiscombe and Warren 1980), but may be more significant at longer wavelengths. Since modelling the BRDF of the snow surface with plane-parallel radiative transfer models does not match measurements for the natural rough surface, as discussed below in Section 2.5.2, it is difficult to quantitatively assess the variability of R that results from the small grain-size variations that occurred between our observations. However, it seems likely that much of the variation between observations made on different days at similar solar zenith angles (discussed at the end of Section 2.3.4) is due to these grain-size variations.

Our parameterizations also contain some level of uncertainty due to changes in the dimensions and orientation of the surface roughness features in the two summers during which we collected the data. It is only the variability of the features that introduces uncertainty into our parameterization, and while the exact shape and location of particular features changed over time, the overall character of the surface roughness did not change noticeably. Therefore, given that our measurement footprints were large enough, these changes will have little effect on the parameterizations.

Ultimately the parameterizations ignore much of the minor variability caused by day-to-day changes, and focus on the most significant ways in which the BRDF varies with solar zenith angle and either wavelength or albedo. This produces parameterizations valid for "average" conditions on the high parts of the Antarctic Plateau. The RMSE (Table 2.1) of the parameterizations provides some quantitative estimates of the uncertainty in the parameterizations.

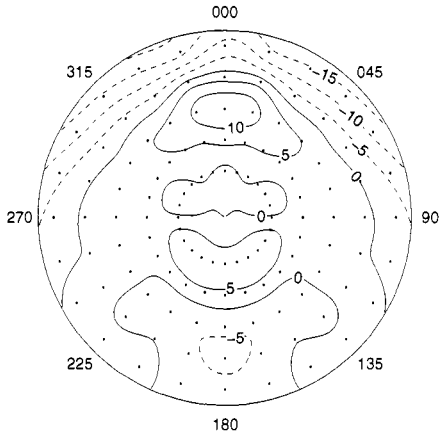

Figure 2.13: Relative difference (%) between observations of R at 900 nm from South Pole and Dome C. Negative contours are dashed and indicate angles at which R was greater at Dome C than at South Pole. The solar zenith angle at the time of the observations was 73.3° at Dome C and 73.5° at South Pole. The South Pole data are from Figure 4b of Warren et al. (1998).

2.5 Discussion

2.5.1 Comparison of Dome C to South Pole

The parameterizations presented above may apply only to the snow at Dome C since all of the data were collected there. However, we suggest that they can also be applied to snow on other high parts of the plateau, where surface features are similar to those at Dome C. Here we investigate whether they can be applied to areas of the plateau away from the domes and ridges by looking at a comparison with data from the South Pole.

Figure 2.13 shows the relative difference between two observations of R at $\lambda = 900$ nm, one made at Dome C with $\theta_o = 73.3°$ and the other made at the South Pole with $\theta_o = 73.5°$; the South Pole data were presented in Figure 4b of Warren et al. (1998). The differences at most angles are less than 10%. Given the uncertainties in both observations, this comparison suggests the data from Dome C are representative of conditions on other parts of the plateau, except at large viewing zenith angles in the forward scattering direction, the region most affected by sastrugi.

A similar comparison between the South Pole observation and the parameterization results at $\lambda = 900$ nm and $\theta_o = 73.5°$ (not shown) also indicated differences less than 10% at viewing

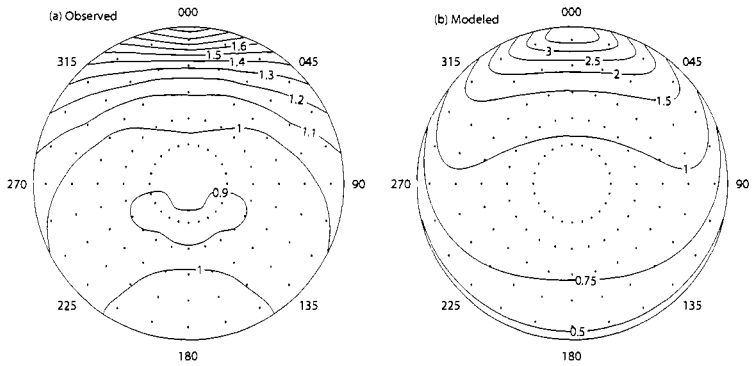

Figure 2.14: Values of R at 900 nm, $\theta_o = 64.8°$, observed for the natural rough surface at Dome C (a) and modeled for a hypothetical flat surface with DISORT (b).

zenith angles less than about 55°, but larger differences at larger viewing zenith angles, especially in the backscatter direction. Taking these two examples together, along with results from Warren et al. (1998) showing that the effect of sastrugi was mostly limited to large θ_v, we suggest the parameterizations may be applied to areas of the Antarctic Plateau with large-scale surface slope similar to that at the South Pole at viewing zenith angles less than 55°.

2.5.2 Comparison of Rough and Flat Surfaces

We have referred to the effect of sastrugi and surface roughness on the BRDF of snow but we have not been able to show exactly what effect these features have. Figure 2.14 shows the observed pattern of reflectance at $\lambda = 900$ nm and $\theta_o = 64.8°$ along with the reflectance predicted by DISORT, a multiple-scattering radiative-transfer model (Stamnes et al. 1988), for the same wavelength and solar zenith angle. The snow in DISORT was described as a semi-infinite layer with particle effective radii of 100 μm (the single-scattering albedo and asymmetry parameter were calculated with Mie theory for 100-micrometer ice spheres, and their phase function was then specified as the Henyey-Greenstein phase function with the asymmetry parameter determined from Mie theory).

This modeled snow surface is perfectly flat, so the reflectance pattern shown in Figure 2.14b should be representative of that from a snow surface with no surface roughness. These two patterns together suggest that the surface roughness greatly reduces the forward reflectance peak

(because an observer looking toward the sun sees shaded surfaces) and enhances the backward reflectance (because the roughness effectively reduces the incident zenith angle on roughness elements viewed when looking away from the sun). These effects of the surface roughness, combined with the tendency of the reflectance from a smooth snow surface to decrease continuously from forward to backward scattering angles, results in the observed minimum values of R, located at small viewing zenith angles in the backscattered direction.

The phase function of the real snow grains differs from the Henyey-Greenstein phase function, so some of the differences between Figures 2.14a and b could be due to an inadequate specification of the phase function in the model. Similar modelling in the future, using a variety of realistic phase functions, will further illustrate the degree to which this difference is caused by surface roughness. Leroux and Fily (1998) modeled the effect of sastrugi on the BRDF of snow and found that they do significantly reduce the forward reflectance while enhancing the backward reflectance. Their results support the suggestion that much of the difference between the measured and modeled reflectance in Figure 2.14 is due to the presence of sastrugi on the Dome-C snow surface.

2.5.3 Is BRDF Constant Across the Visible and Near-UV?

As discussed in Section 2.2, the values of R presented here for wavelengths less than about 800 nm are not directly related to the true BRDF of the snow because of the significant amount of diffuse light reaching the surface at wavelengths where Rayleigh scattering is effective. Often the user of these parameterizations may wish to obtain the true BRDF at these wavelengths, and here we discuss a method that may provide this.

We have seen that at wavelengths where Rayleigh scattering is not important, and at which R is therefore directly related to the true BRDF by Equation 2.5, R varies smoothly with α. Furthermore, extrapolating the relationship seen in Figure 2.7 at $\alpha < 0.9$ (wavelengths where Rayleigh scattering is not important) to $\alpha = 1.0$ suggests that, were there no diffuse light at these wavelengths, R would not vary much between $\alpha = 0.9$ and $\alpha = 1.0$. Based on these observations, it might be reasonable to assume that the BRDF at any wavelength at which Rayleigh scattering affects our observations can be determined from our observed values of R at 800 or 900 nm,

where α is around 0.9 and Rayleigh scattering is unimportant.

To test this idea in the near-UV where Rayleigh scattering is very strong, we again made use of DISORT, this time applied to the atmosphere rather than the snow. Figure 2.14 shows that simple implementations of DISORT cannot accurately model the reflectance from the snow surface, so we instead specified the surface BRDF at $\lambda = 375$ nm to be the same as that measured at 900 nm (but accounting for the difference in albedo)

$$\rho(\lambda = 375 \text{ nm}, \theta_\circ = 64.8^\circ, \theta_v, \phi) = \frac{\alpha(\lambda = 375 \text{ nm})}{\pi} R(\lambda = 900 \text{ nm}, \theta_\circ = 64.8^\circ, \theta_v, \phi).$$

This form comes from Equation 2.5, with the assumption that $R(\lambda = 375 \text{ nm})$ would equal $R(\lambda = 900 \text{ nm})$ if there were no diffuse light. We then used DISORT to apply the direct and diffuse downwelling radiation fields at 375 nm to the surface based on $R(\lambda = 900 \text{ nm})$, and compare the predicted upwelling radiation to the parameterization of $R(\lambda = 375 \text{ nm})$.

If our assumption is true that without diffuse light R would be similar at all wavelengths less than 900 nm, then the radiance reflected from the surface in this model should produce a pattern similar to our parameterization of R for $\lambda = 375$ nm and $\theta_\circ = 64.8^\circ$. Figure 2.15 shows the relative difference between the two. The model produced slightly too much forward reflectance, but agrees with the parameterization to within 4% at most angles and to within 7% everywhere, supporting our assumption. One possible cause for the differences shown in Figure 2.15 is the exclusion of aerosols and boundary-layer ice crystals from our model atmosphere; these would create more diffuse light, which would decrease the forward reflectance peak and increase reflectance elsewhere. The relatively small errors seen in Figure 2.15 indicate that the R patterns for wavelengths around 900 nm may be used to calculate the BRDF of the snow for all visible and near-UV wavelengths, without introducing large uncertainties.

The BRDF of the lower boundary in DISORT must be specified for all incidence angles from the sky-hemisphere, but our parameterizations are valid only for a limited range of incidence angles. We assumed an isotropic BRDF for an incidence angle of 0°, and specified the BRDF for incidence angles less than 51.6° as a linear interpolation between the isotropic pattern and that predicted for an incidence angle of 51.6°. While this is not likely to be completely accurate, the errors resulting from this approximation should be small since the BRDF at 51.6° is already

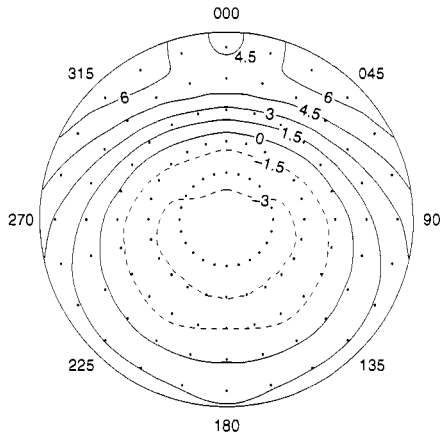

Figure 2.15: Relative difference (%) between parameterized values of R at 375 nm, $\theta_\circ = 64.8°$ and modeled values of R, computed with DISORT by placing layers representative of a typical Dome C summertime atmosphere, with properties appropriate for 375 nm, above a surface with a BRDF specified as equal to the parameterization at 900 nm with $\theta_\circ = 64.8°$. Negative contours are dashed and indicate angles at which the DISORT results were less than the parameterization.

nearly isotropic. The BRDF at incidence angles greater than 86.6° was specified as being equal to that at 86.6°.

For DISORT to determine the downwelling radiance field at the surface, it requires as input the optical depth, single-scattering albedo, and phase function of layers above the surface that represent the effect of the Dome C atmosphere on 375-nm light. The properties of these "atmospheric" layers were determined by using SBDART (Ricchiazzi et al. 1998), a spectral atmospheric radiative transfer model developed around DISORT, which uses spectral transmission data to determine the radiative properties of atmospheric layers given vertical profiles of temperature, pressure, water vapor, and ozone, along with aerosol data. SBDART was run with an atmospheric profile that was typical of the summertime atmosphere at Dome C. The output from SBDART included the optical depth and single-scattering albedo for the atmospheric layers, which we then used, with the Rayleigh phase function, as the atmospheric layers in DISORT. DISORT could then be used to model the radiative transfer from the top of the atmosphere to just after interaction with the surface. SBDART was used only to generate the appropriate input for DISORT because SBDART does not allow for the specification of an arbitrary lower BRDF.

In the atmospheric profile used as input to SBDART, temperature, pressure, and water vapor concentration below 28 km were specified as the mean of 47 radiosoundings conducted at Dome C during January 2004. Ozone concentration at all heights, and all quantities above 28 km were taken from the summertime South Pole model atmosphere of Walden et al. (1998), who used ozonesonde data for ozone concentrations below 30 km, and various satellite data for all quantities above 30 km. Our model atmosphere did not include any aerosols.

2.6 Summary

The data presented in this paper were collected at a high part of the Antarctic Plateau, where the surface slope is extremely small. As a result of the small slope, the winds at this site are both less intense and less directionally constant, resulting in a smoother and more randomized snow surface, than at other Antarctic locations at which the surface BRDF has previously been studied. The smoother snow surface minimizes the effect of the varying azimuth angle between the sun and the dominant direction of orientation of the surface roughness features, eliminating one of the difficulties that various remote sensing techniques must handle on the plateau.

The advantages of this location, combined with newer spectroscopic technology, allowed us to collect enough data during two summers to produce parameterizations that predict the anisotropic reflectance factor of the snow in this region, for most of the solar spectrum and for a wide range of solar zenith angles, with a high degree of accuracy. The development of relatively simple parameterizations was made possible by using the empirical orthogonal functions of the data set as our basis functions. Here we discuss some of the issues that must be considered when using these parameterizations.

Since the data were collected in just one location, the parameterizations are not necessarily applicable to the entire continent, nor to any other snow surfaces away from Dome C. However, with proper consideration, they can be used for some other areas. Most immediately, any part of the high Antarctic Plateau with small surface slope is likely to have similar surface properties to the area around Dome C, meaning these can probably be used around Dome A and along the ridge between Domes A and C with a good deal of confidence. Most other areas of the plateau have larger slopes and therefore larger sastrugi. Warren et al. (1998) showed that the sastrugi

at South Pole caused very little variation of the BRDF at viewing zenith angles less than about 50°. A comparison of data from Dome C and South Pole show that the data do not differ much at viewing zenith angles less than about 55°. For these reasons, the parameterizations should produce reasonable estimates of the anisotropic reflectance factor for any part of the Antarctic Plateau with sastrugi not much larger than those found at South Pole, as long as their use is limited to $\theta_v \lesssim 55°$. Perhaps they can also be applied, with caution, to the highest parts of the Greenland Ice Cap, in areas that do not experience melting.

The parameterizations should not be applied to the slope between the plateau and the coast of Antarctica. Winds in those areas tend to be both strong and directionally constant, resulting in large and well-aligned sastrugi, which may affect the reflectance even into near-nadir angles.

Snow in midlatitudes and seasonal Arctic snow may differ from snow on the Antarctic Plateau in any of several ways: it may not have significant macroscale surface roughness, it may contain more soot and other natural or anthropogenic contamination, it usually forms at higher temperatures thus producing larger snow grains, it experiences melting and more rapid metamorphism, and it may be affected by vegetation. Any of these factors would cause the BRDF to differ from these parameterizations.

In using these parameterizations, there are a few things to consider. Each parameterization was developed with a certain set of data, and none should be used outside of the range of parameters that is covered by its data set (shown in Table 2.1).

Parameterizations C–F were developed using the measured values of spectral albedo of the snow at Dome C (Figure 2.6) as one predictor of R, rather than wavelength; this made more physical sense in these spectral regions than using wavelength directly. Perhaps, when applying these parameterizations, the user can estimate the albedo of the snow of interest, and can use that directly (doing so should help to compensate for grain size differences between the snow of interest and the snow at Dome C). This idea has not been tested, and so should be used cautiously; if the expected albedo at a given wavelength is outside the range of albedos used to develop the parameterizations then it is unlikely that they will work for the snow of interest. If the user does not have a better estimate of albedo, then the values presented here for the development of the parameterizations (Figure 2.6, and in tabular form with the online supplementary material) may

be used.

Users should be cautious when applying the parameterizations to the visible and ultraviolet region of the spectrum since the predicted value of R at these wavelengths is not directly related by Equation 2.5 to the true BRDF because of the significant amount of diffuse incident light. If the true BRDF is the desired result in this spectral region, it can be determined from Equation 2.5 by using $R(\lambda = 900 \text{ nm})$ and the albedo at the wavelength of interest.

The parameterizations presented here are, to the authors' knowledge, the most comprehensive set available that are based on data. The difficulties of accurately modelling the angular reflectance of snow are many, and it is a time-consuming process, especially correctly accounting for surface roughness. We hope that these parameterizations will reduce the need for this modelling, and provide points for comparison when such modelling is necessary or desired. Our parameterizations can also provide good lower boundary conditions for atmospheric radiative transfer modelling over snow, allowing for estimates of the top-of-atmosphere BRDF for use with satellite data.

Chapter 3

THE EFFECT OF CLOUDS OVER SNOW ON DIRECTIONAL REFLECTANCE

This chapter was published under the title "An explanation for the effect of clouds over snow on the top-of-atmosphere bidirectional reflectance" in 2007 in *Journal of Geophysical Research* **112** (D19202) with coauthor Stephen G. Warren. Warren provided the initial suggestion that I investigate the explanation presented here, helped guide my research, and edited the manuscript.

3.1 Introduction

Understanding the effect of clouds on the bidirectional reflectance distribution function (BRDF) of snow-covered areas of the planet is necessary for quantifying the effects of clouds on the Earth's radiation budget (ERB) and for measuring the ERB from space. Such an understanding could also help develop methods for identifying clouds over the polar regions from satellite observations, a task that is still the subject of much research (Hatzianastassiou et al. 2001; Li et al. 2003).

Clouds and snow are both made of water, so their absorption spectra are broadly similar. This is true for both ice clouds and liquid-water clouds, because the absorption spectra of ice and water approximately parallel each other across the solar spectrum (e.g. Dozier 1989); i.e., at wavelengths where electronic transitions and intramolecular vibrational transitions are the dominant absorption mechanisms. (The water and ice spectra diverge in the thermal infrared where rotation and lattice-vibrations become important (Figure 1 of Irvine and Pollack 1968).) Viewed from above at most visible or near-infrared wavelengths, cloud-covered snow should therefore just resemble deeper snow, if there are no significant absorbers in the snow, in the cloud, or in the atmosphere between the cloud and the snow. The cloud particles, however, have effective radii

$r_{\text{eff}} < 20\ \mu$m, whereas surface snow grains are larger, with effective radii typically 50 μm for cold snow at the Antarctic surface, and much larger for melting snow. Because near-infrared albedo is higher for smaller particles, the broadband planetary albedo above a cloud over snow should be somewhat greater than that of clear sky over snow. The visible albedo should be unchanged. The effect on spectral albedo of putting a cloud over snow in a plane-parallel radiative transfer model is shown in Figure 1b of Masonis and Warren (2001); it is similar to the effect of a thin layer of fine-grained snow ($r_{\text{eff}} \sim 30\ \mu$m) over a thick layer of 100-μm snow (Figure 4 of Grenfell et al. 1994).

It has therefore been a long-standing puzzle that in nadir-viewing satellite pictures, cloud-covered snow is usually darker than clear sky over snow. Welch and Wielicki (1989) gave some examples from Landsat, one of which is reproduced in Figure 3.1. The entire upper half of this image contains snow-covered sea ice, but the lower-right portion of that ice is overlain by cloud, causing it to appear darker than the cloud-free areas with ice. Welch and Wielicki then used a Monte-Carlo model to show how clouds could lower the albedo over snow if they were tall and broken (essentially a 'trapping' effect as seen also for sastrugi in Figure 13 of Warren et al. (1998)). However, most clouds over snow do not have the height-to-width ratios required by Welch and Wielicki. Later Nemesure et al. (1994) compared Earth Radiation Budget Experiment (ERBE) measurements at the South Pole with surface identification of clear and cloudy scenes, showing that clouds do increase the planetary albedo over snow, in agreement with the plane-parallel model.

The darkening of the nadir view by clouds, also seen in AVHRR data by Loeb (1997), must therefore not indicate a reduced albedo, but instead be compensated by a brightening at larger viewing zenith angles. Wilson and Di Girolamo (2004) showed this to be true using measurements from the Multi-angle Imaging SpectroRadiometer (MISR), which observes the same scene nearly simultaneously at nine different viewing zenith angles. Clouds and the Earth's Radiant Energy System (CERES) measurements also give the same result (Figure 7 of Loeb et al., 2005; Figure 3 of Kato and Loeb 2005). Some data from the case analyzed by Wilson and Di Girolamo (2004) are shown in Figure 3.2. These show the bidirectional reflectance factor (a scaled reflectance that will be defined explicitly in Section 3.4) of the same scene, measured by MISR at

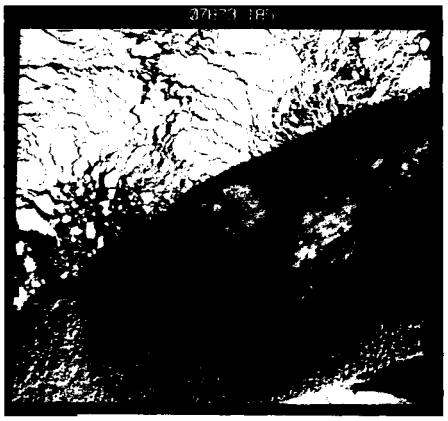

Figure 3.1: Landsat scene of partial cloud cover over sea ice in the Beaufort Sea, 71.0°N, 143.5°W, 12 October 1986. The solar elevation is 11°, solar azimuth is to the lower right of the frame. The shadow of the cloud is apparent as the dark band extending from lower left to upper right. The width of the frame is 185 km. Spatial resolution is 57 m. (Figure 4D of Welch and Wielicki (1989); original photo supplied by R. Welch.)

different viewing angles. The scene consists of snow-covered sea ice in the Beaufort Sea, north of Alaska. The darkest areas are open water exposed in leads. Near the center of the images, a large floe is visible under mostly clear skies; the area in the left half of the images is overcast, with some leads still visible at nadir through the thin cloud. When observed at nadir (left panel) the cloudy area appears darker than the clear area, but when forward-scattered light is viewed in the right panel, the clouds appear much brighter than the surface.

However, resolving one puzzle introduced another puzzle. In general, smaller particles are less forward-scattering than larger particles, so their asymmetry factors are lower. Putting a plane-parallel cloud, especially an ice cloud, over plane parallel snow in a radiative transfer model therefore slightly enhances the nadir reflection and reduces the forward reflectance peak, just the opposite of what is observed.

Explaining the observed effect of clouds on the reflected radiance field has proven difficult. Welch and Wielicki (1989) examined only near-nadir radiances and albedos, and therefore saw only that areas where clouds covered the snow were darker than cloud-free areas nearby. They attributed this darkening to increased absorption due to multiple scattering between the cloud and the surface giving the surface more opportunities to absorb the light, but this explanation does not

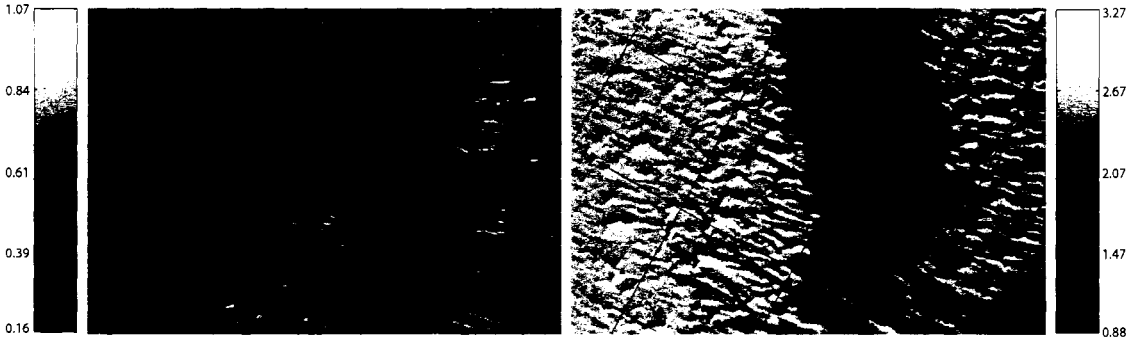

Figure 3.2: Bidirectional reflectance factor (BRF) at 672 nm observed by two cameras on MISR over the Beaufort Sea on 4 June 2000 at 0708 UTC (block 8 of orbit 2460, data version number 23). The left panel shows the BRF observed near nadir and the right shows the BRF measured when looking at a zenith angle of 70.5°, 15° from the principal plane, in the forward direction. The grid is labeled in degrees of north latitude and west longitude. The local time at longitude 150°W was 2108, so the sun was in the northwest at zenith angle 78°; the direction of view in the image at right (also the direction of travel for the satellite) is towards the top of the page.

explain the latter observation that cloudy areas are brighter than the cloud-free areas when viewed at large zenith angles. Kato and Loeb (2005) were unable to explain their observations from CERES using a plane-parallel radiative transfer model with a variety of particle scattering phase functions. They left the question unanswered, but suggested the effect may be due to surface roughness. Here we present an argument for the surface-roughness explanation. In particular, we suggest that polar clouds, which are often stratiform and/or optically thin, present a surface that is, optically, much smoother than the snow surface, thus masking the effect that snow-surface roughness has on the BRDF of snow.

3.2 The Effect of Surface Roughness on the BRDF of Snow

Polar snow surfaces are usually rough, primarily due to wind erosion. In this paper, we focus on observations from the East Antarctic Plateau; Figure 2.2 shows a typical view of the rough snow surface found in this area. The surface features visible in Figure 2.2 are called sastrugi, and they are typically elongated, with their long dimensions aligned parallel to the direction the wind was blowing when they formed. The photograph was taken at Dome C (75°S, 123°E), where

the standard deviation of surface elevation measurements made every 20 or 50 cm along several 20- to 35-meter lines was 2.3 cm, and where the highest sastrugi were 6 to 8 cm above the mean surface. The snow surface on many parts of the East Antarctic Plateau is rougher than at Dome C as a result of stronger winds.

We now consider the effect surface roughness has on the directional reflectance from a snow surface. Three-dimensional modelling of the radiative transfer in a snow pack with surface height variations similar to those found on polar snowpacks remains computationally challenging due to the large optical depth of the snow in the rough layer (just 1 cm of snow has an optical depth of more than 50). Nevertheless, we can gain an understanding of the effect of the roughness, at least qualitatively, without such modelling.

The simplest way to understand the effect is to consider how surface roughness affects what an observer sees when looking at a snow surface illuminated primarily by direct-beam radiation with a non-zero solar zenith angle (Figure 3.3). When observing light coming from the direction of the solar azimuth, the observer will see the shaded or shadowed sides of roughness elements. When the observer looks at small viewing zenith angles (nearly straight down), significant areas of the snow between roughness elements and even some of the sunlit sides of the elements will be seen, but as the viewing zenith angle increases the fraction of the field of view occupied by the shaded sides of roughness elements will increase. The area of each roughness element that is shadowed will depend on both the geometry of the roughness elements and the solar zenith angle. For a given geometry, the shadowed area will increase with solar zenith angle once a critical solar zenith angle is reached; below that critical zenith angle (where the solar elevation angle is equal to the largest slope on the shaded side), the roughness element produces no shadowed area. Regardless of the solar zenith angle, all parts of the shaded side of the element will receive less incident energy per unit area than a flat surface would. The result is that surface roughness reduces the forward-reflected intensity, relative to that from an identical, flat snow surface. This effect is greater at larger viewing zenith angles, and larger solar zenith angles.

Similarly, when an observer looks directly away from the sun, at backward-reflected light, some part of the field of view will be occupied by the sunlit sides of the roughness elements. These sides will appear brighter than a flat snow surface because they receive more incident

Figure 3.3: Two photographs of the snow surface at the South Pole taken from 22 m above the surface at the same time, in early March, just before sunset. The one on the left was taken while facing away from the sun, showing that the sastrugi enhance backward reflectance. The one on the right was taken while facing the sun, showing that the sastrugi reduce forward reflectance. The extremely large solar zenith angle and the wide spacing between sastrugi combine to make the effect very easy to see. The time of day was chosen so that the solar azimuth was approximately perpendicular to the long axis of the sastrugi, which also maximizes the effect. Photographs provided by Stephen Warren.

energy per unit area since the incident angle is locally reduced. Again, the effect will be greater at larger viewing zenith angles because the sunlit sides of elements will occupy a larger fraction of the field of view. This effect is also greater at larger solar zenith angles because the cosine changes more rapidly with angle for angles closer to 90°. The effect is somewhat complicated by the fact that the viewing zenith angle is also locally different when viewing a roughness element, so variations in the BRDF of the snow with viewing angle may cause the intensity difference to differ from what would be expected from the difference in incident angle cosines. However, the increase in incident energy probably overwhelms changes in the BRDF, except at small solar zenith angles. The effects of sastrugi on the BRDF of the snow are quite apparent in the photographs shown in Figure 3.3.

Observational and modelling studies support the idea that snow-surface roughness has an effect on the directional reflectance from the snow. Warren et al. (1998) used directional reflectance observations from the South Pole, where the solar zenith remains nearly constant during a day as its azimuth changes, to show that the forward reflectance peak was reduced and the backward re-

flectance was enhanced when the solar azimuth was perpendicular to the long axis of the sastrugi (which are well-aligned at the South Pole due to a fairly constant wind direction), compared to when the two were parallel. Variations in the directional reflectance with the sun-sastrugi angle increased with viewing and solar zenith angles. Leroux and Fily (1998) and O'Rawe (1991) both modeled the reflectance from a snow surface with highly idealized sastrugi by combining the modeled BRDF of a flat snow surface with the shadowing and intercepting effects of the rough surface. Both of these modelling studies showed that the roughness reduces the forward scattering and enhances the backscattering, but the magnitude of the modeled effect was too large, compared to observations, likely because of the idealized geometry used to describe the sastrugi.

Loeb et al. (1998) used a three-dimensional Monte Carlo model to compare the reflectance of overcast scenes from plane-parallel clouds to that from clouds with cloud-top height variations. Their results show that the presence of cloud-top height variations reduces the forward reflectance, by up to 30% in their cases, and, in some cases, slightly enhances the backward reflectance, by up to 10%. Their optical depth variations were far smaller than those on the Antarctic snow surface, but the results are not directly comparable since their clouds were underlain by a black surface, emphasizing the low-order scattering. Nevertheless, these results again show that roughness reduces forward reflectance and enhances backward reflectance.

To get a sense of the magnitude of the effect of snow-surface roughness on the directional reflectance of East-Antarctic snow, we can compare observations with plane-parallel modelling results. First we define the anisotropic reflectance factor (R), which we use to describe the directional reflectance:

$$R(\theta_\circ, \theta_v, \phi) = \frac{\pi I_r(\theta_\circ, \theta_v, \phi)}{\int_0^{2\pi} \int_0^{\pi/2} I_r(\theta_\circ, \theta_v, \phi) \cos\theta_v \sin\theta_v \, d\theta_v \, d\phi}. \tag{3.1}$$

Here, $\theta_\circ$ is the solar zenith angle; θ_v is the viewing zenith angle; ϕ is the relative azimuth angle, and I_r is the reflected radiance. An isotropic surface with any non-zero albedo has $R = 1$ at all angles.

The values of R for the snow at Dome C at wavelength (λ) 800 nm and solar zenith angle 70° are contoured in Figure 3.4 (top left). These values are from the parameterization presented in Chapter 2, which was developed from spectral observations of R at Dome C at 96 different solar zenith angles. These observations were made with a measurement footprint that was large

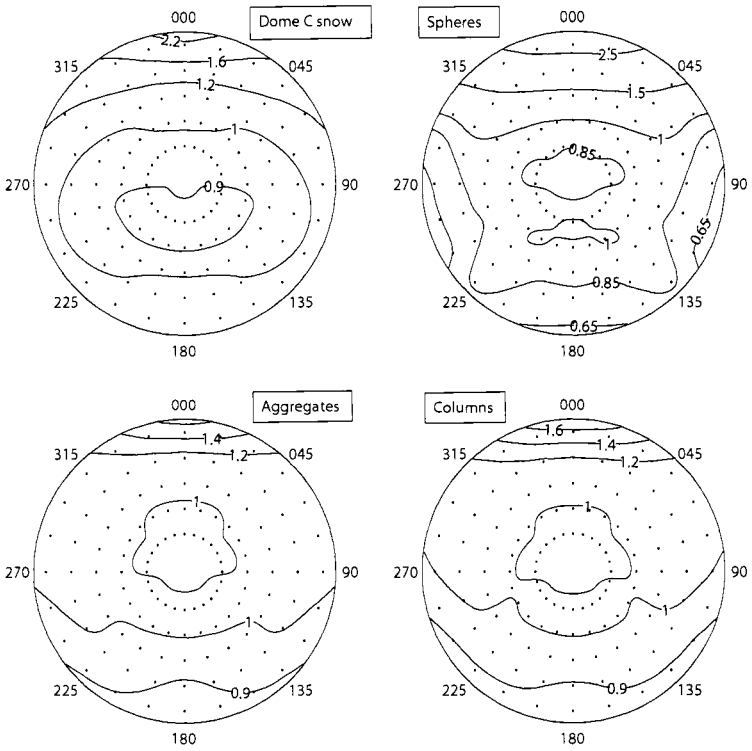

Figure 3.4: The upper-left plot shows the anisotropic reflectance factor (R) of the snow at Dome C. The other plots show the ratio of R modeled with DISORT, using different shapes to represent the snow grains, to the values in the upper-left plot. All plots are for wavelength 800 nm and solar zenith angle 70°. Values are contoured as functions of viewing zenith angle, increasing with distance from the center, and relative azimuth angle, increasing clockwise from the top. Dots are located every 15° in both zenith (starting at 22.5°) and azimuth. Note the contour intervals vary within and between plots.

enough to include a representative sample of surface roughness features, thereby capturing the effect of the surface roughness. When we need to make comparisons to clear-sky values of R at angles that were not observed, we use the parameterization to interpolate between angles that were observed.

The other plots in Figure 3.4 show the ratio of R predicted by DISORT (Stamnes et al. 1988), a plane-parallel radiative transfer model, for snowpacks composed of ice spheres, aggregate grains, or columns, to the values of R for the Dome C snow. All modelling was done with $\theta_o = 70°$ and atmospheric layers appropriate for the clear, summertime, Dome C atmosphere at $\lambda = 800$ nm.

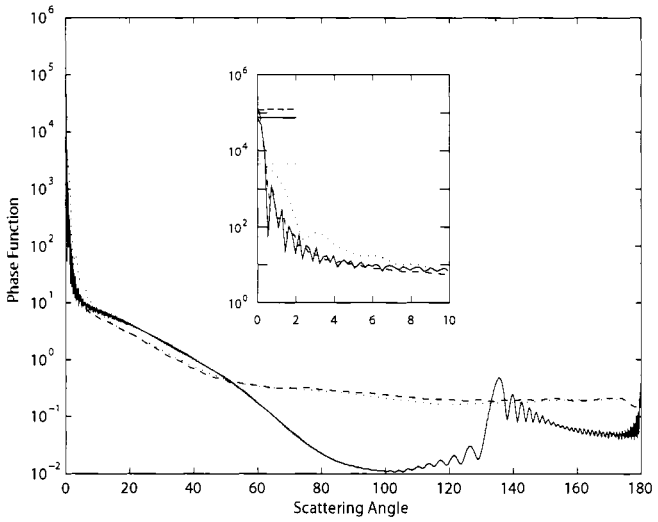

Figure 3.5: The three phase functions used in the modelling results shown in Figure 3.4. The solid line is the phase function for a 50-μm ice sphere, the dashed line is that for an aggregate ice crystal with maximum dimension of 200 μm, and the dotted line is that for a hexagonal column ice crystal with $a = 10$ μm and a length of 20 μm. The 0° to 10° region is enlarged in the inset, where the horizontal lines mark the maximum values.

The atmospheric layers were created using SBDART (Ricchiazzi et al. 1998), as described in Section 2.5.3. The single-scattering properties of the ice spheres were calculated for $\lambda = 800$ nm using the Mie code of Wiscombe (1980). The single-scattering properties of the aggregates and columns were calculated using an improved geometrics optics method (Yang and Liou 1996). The phase functions used in these calculations are shown in Figure 3.5. The scattering properties of the aggregates and columns are both for ice crystals with microscale roughness on their surfaces, which eliminates the halo peaks in the phase function. Using the scattering properties for particles without this roughness produces halos in the reflectance that are only rarely seen in the real snow, but otherwise causes no significant differences in the results. The radiance leaving the snow was calculated by DISORT on a $1° \times 1°$ grid; these were then averaged to simulate the coarser resolution of the observations.

For each of these possible phase functions, Figure 3.4 shows that the ratio of the plane-parallel reflectance to the observed reflectance is significantly greater than one at large forward-reflected

angles, and somewhat less than one at large backward-reflected angles, consistent with the expected effect of removing surface roughness. Also, the difference between the plane-parallel reflectance and the observed reflectance increases with solar zenith angle (not shown). With $\theta_o = 83°$ the plane-parallel R is around twice as large as the observed R in the forward direction, and about 30% lower in the backward direction; but with $\theta_o = 60°$ the differences between the plane-parallel and observed values of R are not much larger than the uncertainty in the observations. The snow grains at Dome C are mostly irregular aggregates, so it is not surprising that the aggregate model has the smallest error.

By performing these calculations at $\lambda = 800$ nm, where Rayleigh scattering and atmospheric gaseous absorption are both weak, we have minimized the possibility of errors due to an inaccurate specification of the atmospheric properties. The snow at the Dome C observation site had measured soot content between 0.5 and 3 nanograms of carbon per gram of snow (Warren et al. 2006), so impurities are unlikely to be the cause of the difference between the model and observations. Our modelling does not account for possible near-field effects of the closely packed snow grains; however, as explained by Warren (1982) in section E5a, this is not likely to be a problem since most of the volume of a shell of thickness on the order of λ surrounding a snow grain is occupied by air, not other snow grains. We therefore think it is reasonable to suggest that most of the difference between the modeled aggregate snowpack reflectance and the observed reflectance is due to the surface roughness, indicating that for this wavelength and solar zenith angle, the roughness reduces the forward reflectance by about 40%, and enhances backward reflectance by about 10%.

3.3 The BRDF of Fog over a Rough Snow Surface

Now that we have illustrated the effect of surface roughness on the directional reflectance of snow, we examine what happens when a cloud is placed above the rough snow surface. To begin, we look at the case of a thin fog layer above the snow. We made directional reflectance observations in the presence of fog at Dome C on several occasions. In all cases the fog layer extended from the surface to about 20 m; so, from our observation location at 32 m above the surface, we were looking down at the top of a thin cloud over the snow. As shown in Figure 3.6,

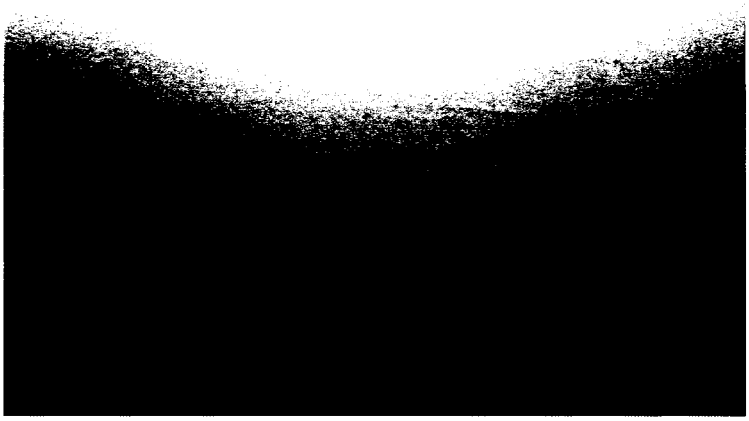

Figure 3.6: A photograph showing the strongly enhanced forward peak caused by a thin fog layer over the snow at Dome C.

the fog caused a strongly enhanced forward peak, noticeable by eye; its effect at other angles was less dramatic, except for the presence of a glory around the antisolar point. The glory, as well as riming on the observation tower, indicated that the fog was composed of supercooled liquid water droplets. These cases provide for a convenient case study since we have direct observations of the anisotropic reflectance pattern above the fog, along with observations at similar solar zenith angles without fog.

A representative reflectance observation above the fog is shown in Figure 3.7, along with the reflectance from the snow surface under a clear sky for the same solar zenith angle and wavelength; the relative difference caused by the fog is also shown. The addition of the fog has a qualitatively similar effect on the anisotropic reflectance factor to the removal of surface roughness; that is, it enhances the forward reflectance, by over 60% at large viewing angles, and reduces the backward reflectance, by about 20% at large viewing angles.

This similarity is more than coincidence. The thin fog, with an optical depth much less than one, presents an optically smooth surface, with optical depth variations that are tiny compared to those on the snow surface; the standard deviation of the snow surface height, 2.3 cm, corresponds

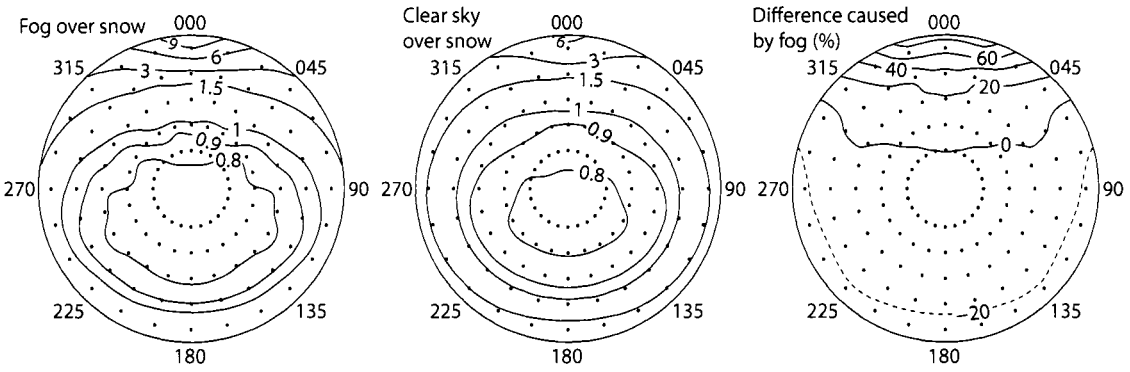

Figure 3.7: Observed R at Dome C with fog over the snow, R for the snow at Dome C with clear sky and no fog, and the relative difference caused by the fog (%). Observations are for $\theta_o = 82.7°$ and $\lambda = 800$ nm.

to an optical depth well over 100. The fog, formed in a very stable atmospheric layer, presents a surface that is also geometrically smooth, but the variations in optical depth are probably more important than those in geometrical depth. Either way, the smooth surface of the fog hides the rough surface of the snow, reducing the effects of the surface roughness on the directional reflectance, especially at large viewing zenith angles, where the optical slant path through the fog becomes significant.

If the fog is presenting a nearly plane-parallel surface, then we should be able to use DISORT to model this observation. However, since the fog is so thin, the surface reflectance is likely to remain important, so we must specify the correct surface BRDF, using the parameterization from Chapter 2, rather than modelling it as a plane-parallel surface or using an isotropic surface. By placing a cloud composed of 10-μm water spheres, with an optical depth of 0.05 above a surface with the parameterized snow-surface BRDF, we are able to match the fog-over-snow observation reasonably well as shown in Figure 3.8 (left and center). Except around the anti-solar point, where the modeled glory is probably too strong because of the uniform droplet size we used for the fog, the error in the model result is generally less than 10% and the strong enhancement of the forward peak seen in Figure 3.7 is modeled well. The angular separation of the glory fringes on a photograph during a different fog event at Dome C indicated an effective radius of between 7 and 8 μm. BRDF calculations were done for both $r_{\text{eff}} = 5$ μm and $r_{\text{eff}} = 10$ μm; the results were

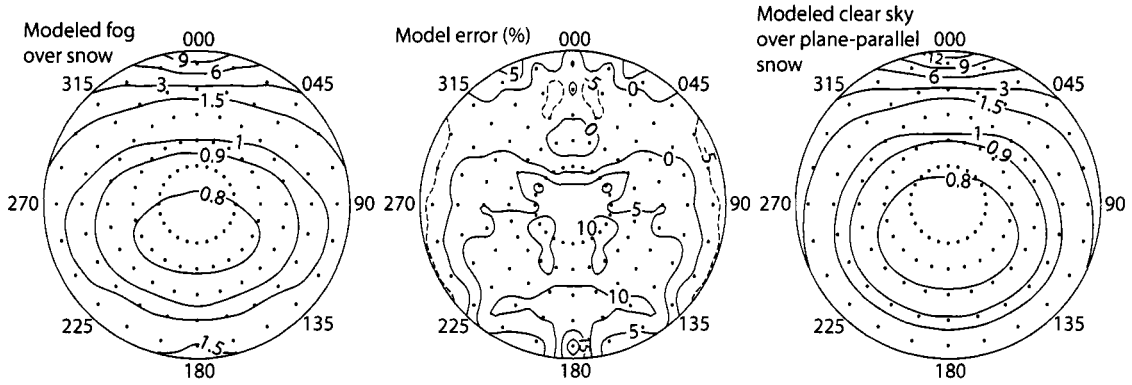

Figure 3.8: R modeled with DISORT for a thin, plane-parallel, liquid-water cloud immediately above a surface with the observed Dome C snow-surface BRDF, and the error of the model results relative to the fog-over-snow observation in Figure 3.7. Also shown is R modeled for a plane-parallel snowpack composed of rough aggregate snow grains under a clear sky. Both models used $\theta_o = 82.7°$ and $\lambda = 800$ nm.

similar.

In order to get such accurate model results with this thin cloud, it is critical to use the correct surface BRDF, since, as illustrated by comparing a modeled clear-sky reflectance for plane-parallel snow in Figure 3.8 (right) to the actual clear-sky reflectance in Figure 3.7 (center), modelling the surface as a plane-parallel snowpack grossly overestimates the forward reflectance at this large solar zenith angle. Therefore, modelling a fog above a plane-parallel snowpack would produce far too much forward reflectance. Of course the phase function of the fog particles is also important for the model; it was not possible to produce such accurate results with a fog composed of aggregate ice crystals. However, even when using an ice cloud, qualitatively correct effects, particularly an enhancement of the forward peak, are obtained, but errors in the side-scatter region are larger than with water drops.

3.4 The View from the Top of the Atmosphere

In the previous section we showed that the roughness of the snow surface is ultimately what leads to the observation that fog enhances the forward reflectance above snow. The fog case was a convenient one to use because of our observations, but the observations that inspired this work

were made from the top of the atmosphere (TOA), and looked at thicker clouds. Now we show that this same argument works well for these observations also.

The TOA observations are often reported as a bidirectional reflectance factor (BRF). The BRF is similar to R, but with the denominator of Equation 3.1 replaced by the incident flux, so that an isotropic surface has a BRF at all angles equal to its albedo. Figure 3.9 shows the BRF near the forward-reflectance peak, measured by MISR at 866 nm from a region around Dome C. Some parts of this scene contain cloud, while other parts are clear. As expected for this viewing geometry, the cloudy areas appear significantly brighter than the clear areas. The two black curves in Figure 3.10 show the MISR observations at all nine angles from the two points marked clear and cloudy in Figure 3.9. Here we can again see that, while the cloud appears brighter than the snow at large viewing zenith angles, it appears darker at near-nadir angles. (Unlike for the fog and plane-parallel snow, the cloud here appears brighter than the clear scene not only in the forward direction but also in the backward direction. This may be an effect of the different phase functions, or a result of the smaller solar zenith angle in this case. It could also simply be a result of comparing BRF with R; if the albedo of the cloudy scene is greater than that of the clear scene then a plot comparing R for these two scenes would have the cloudy curve shifted down relative to the clear curve. We do not have the necessary data to convert the MISR data to R or the surface data to BRF.)

Using DISORT, we modeled the TOA BRF for these two scenes. As for the results above, the model consisted of layers representative of the mean summertime Dome-C atmosphere above a surface with a specified BRDF. The surface BRDF was the product of our parameterization for R and the estimated albedo, both for 866 nm. Since we will now be comparing the BRF, rather than R, our estimate of albedo is important. The albedo was estimated by using SBDART to calculate the spectral albedo of snowpacks consisting of two layers, a 2.5 mm layer above a semi-infinite (optical depth 10,000) layer. The effective grain radius of each layer could be set to any multiple of 10 from 20 to 120 μm. The spectral albedo was then calculated for each combination of grain radii in the two layers, with layers above the snow representative of the Dome-C atmosphere containing a cloud that diffused the solar beam. The grain-size combination (40 μm above 90 μm) that resulted in the smallest root-mean-squared error when compared to our

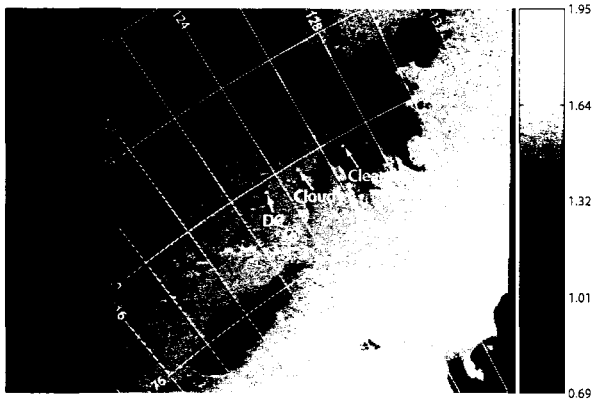

Figure 3.9: The BRF at 866 nm observed by MISR near Dome C at 0006 UTC 17 January 2005 at viewing zenith angle 71° and relative azimuth angle near 30°. The two marked locations in this image, one with cloud cover and one with clear sky, were chosen for further analysis (see Figure 3.10). A visual observation of the sky from the surface indicates it was overcast at Dome C (DC) at this time. Some surface features are visible in the clear region in the higher-resolution nadir image. The interpretation of the brighter areas as cloud and darker areas as clear is also supported by the MODIS cloud mask. The grid is labeled in degrees of south latitude and east longitude. This case uses MISR data with version number 24.

observed albedo (Figure 2.6), measured under diffuse incidence, was then used to calculate the clear-sky spectral albedo at solar zenith angles from 0° to 89°. The effect of surface roughness on albedo is expected to be much less than on reflected radiance (Section 8 of Warren et al. 1998), so the use of a plane-parallel model here should not cause large errors.

The resulting modeled TOA BRF for the clear and cloudy scenes are shown in gray in Figure 3.10. These models used a solar zenith angle of 61.1°, the same as at the two locations at the time of observation. The cloudy scene was modeled with a single cloud layer with optical depth 10, composed of liquid water drops with radius 5 μm. The modeled BRF for the cloudy scene matches the observations quite well, and is not very sensitive to the cloud optical depth or droplet radius. The modeled BRF for the clear scene is also in fairly good agreement with the observations, though it does underestimate the BRF at larger forward angles by about 4%. The addition to the clear model of a layer of boundary-layer ice crystals or of stratospheric aerosols did not correct this error. It also did not help to perform an integration over the MISR channel, rather than using the central wavelength of 866 nm. It seems most likely that the difference be-

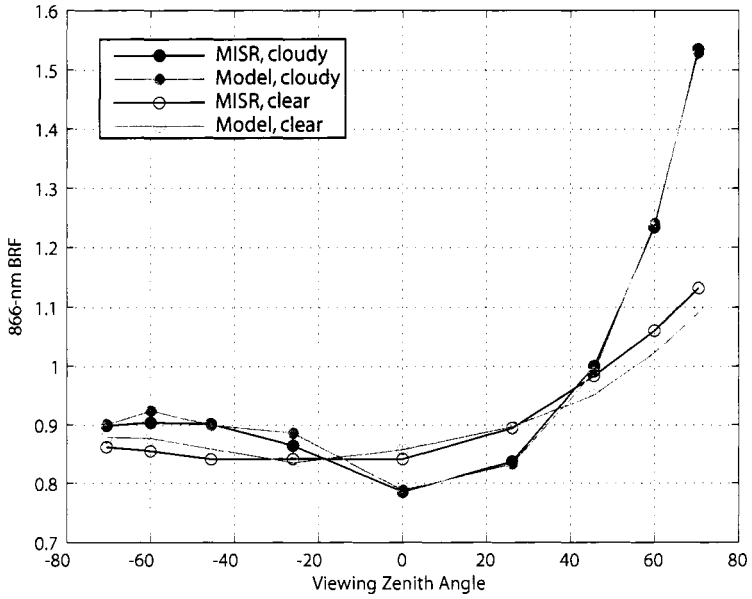

Figure 3.10: Observed and modeled TOA 866-nm BRF at the clear and cloudy locations marked in Figure 3.9. The solar zenith angle is 61.1°. The relative azimuth is about 30° for positive viewing zenith angles (forward scattering) and 150° for negative viewing zenith angles (backscattering).

tween the modeled and observed clear-sky BRF is due mostly to variation in time or space of the snow-surface BRDF.

Figures 3.11 through 3.13 illustrate some of the spatial variability that sometimes exists in the snow-surface reflectance. Figure 3.11 shows a nadir image from MISR around Dome C on a clear day. At least two types of spatial variability appear in this image. The wavy patterns on the right side of the image are megadunes, surface features with amplitudes of a few meters and wavelengths of a few kilometers (Fahnestock et al. 2000). In the left half of the image two areas with different reflectivities are visible, separated by a very distinct boundary. A likely explanation for this is that one of the regions has frost on the snow surface, while the other does not. As seen in Figure 3.12, dramatic changes in reflectance patterns due to frost have been observed while flying over Antarctica.

The observed BRF at all nine MISR angles at the four numbered locations in Figure 3.11 are shown in Figure 3.13, along with the modeled TOA BRF. In this case, the off-nadir model results

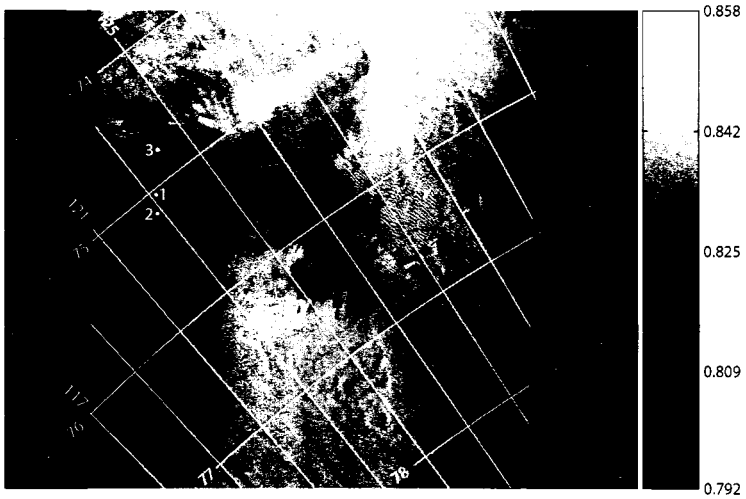

Figure 3.11: The near-nadir 866-nm BRF observed by MISR near Dome C at 2343 UTC 18 January 2004. The visibility of known surface features in the image and a coincident surface observation of the sky over Dome C both indicate that the sky is clear in most, if not all, of the image. The wave-like features to the right are megadunes, large-scale features on the snow surface. The magnitude of the BRF variations are small (note the scale), but, to the left, two different snow types are clearly visible. The four numbered locations correspond to the observations plotted in Figure 3.13. The grid is labeled in degrees of south latitude and east longitude. This case uses MISR data with version number 22.

Figure 3.12: View from an airplane near Siple Dome, West Antarctica (82°S, 150°W), November 1994. The surface elevation is about 500 m. The streaks which appear dark in this photograph were later identified (on an oversnow traverse by snowmobile) as surface frost; viewed from the opposite direction they instead appear brighter than the intervening regions of snow. (The frost therefore probably has little effect on the albedo.) Photo by Nadine Nereson.

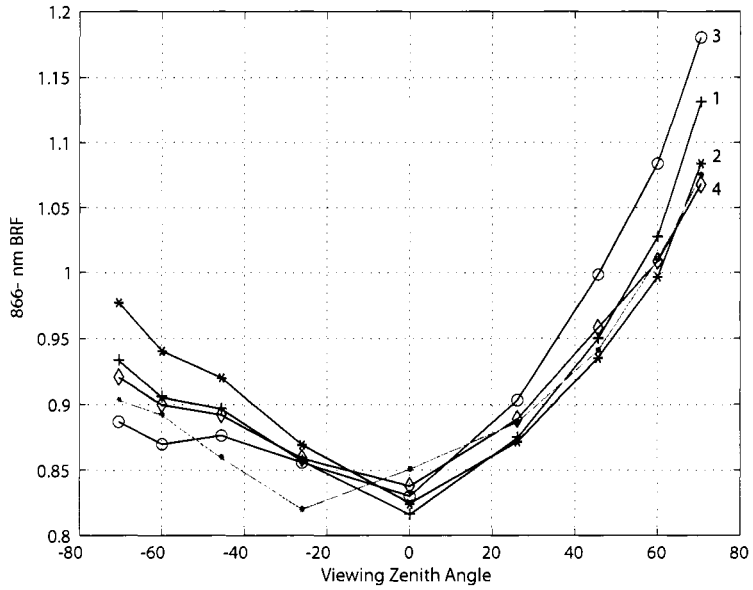

Figure 3.13: The four black curves show the 866-nm BRF observed by MISR at the four numbered locations in Figure 3.11 (the numbers to the right of the curves correspond to the numbered locations in Figure 3.11). The gray curve, marked with dots, is the modeled TOA 866-nm BRF. The solar zenith angle is about 63.5°.

lie in the low range of the observed spatial variability, except at two of the backward directions, where the model results are slightly less than the observations at any of these four locations.

The cases in Figures 3.9 through 3.13 show that our snow-surface reflectance parameterization may be used to model TOA BRF fairly accurately, but that there will be some errors in instantaneous comparisons due to spatial and temporal variability. That our measurement-based parameterization is appropriate for use in modelling satellite-observed reflectance, combined with the argument presented in Section 3.2 regarding the importance of surface roughness on the near-surface observations, suggests that the effect of surface roughness on satellite observations is similar to its effect on the near-surface observations, despite the satellite's larger footprint and much smaller angular field of view.

The orbital configuration of Terra, the spacecraft on which MISR flies, allows MISR to observe Dome C twice on most days, around 0000 and 1600 UTC (0800 and 0000 LST). The cases above were all from overpasses around 0000 UTC, and therefore all have solar zenith angles

around 60° since they were all made in late December or January. As mentioned in Section 3.2, at these solar zenith angles, a plane-parallel snowpack composed of aggregate snow grains has almost the same anisotropy as the observed snowpack. Therefore, when we model these MISR observations using a plane-parallel, aggregate-grain snow pack, the results have very similar anisotropy to what was observed by MISR; however, the resulting BRF is too high at all angles. Using larger aggregate grains would reduce the albedo, but would also likely increase the anisotropy. However, the better test of whether these scenes can be modeled with plane-parallel snow comes at larger solar zenith angles.

To look at this, we chose a clear scene from an overpass around 1600 UTC, when the solar zenith angle was 85°. Because Earth's curvature, which we do not account for, becomes important at large solar zenith angles, a solar zenith angle intermediate between 60° and 85° would probably be preferable, but is not available. In Figure 3.14 we compare two results for the modeled TOA BRF with the observed BRF. The solid gray curve, modeled using the observed surface, compares very well with the observation, with errors less than 10%, despite the large solar zenith angle. The largest errors occur at 26° and 46° in the backward direction, angles that may be affected by the shadow of the tower in our near-surface observations. The dashed gray curve, modeled using a plane-parallel snow pack composed of aggregate grains, shows much larger errors, especially near the forward peak, where the modeled BRF is nearly 30% too large. Again, this shows that the effects of the surface roughness become much more important as the solar zenith angle increases. We estimated the uncertainty caused by neglecting Earth's curvature by rerunning the observed-surface model with the optical depth of each atmospheric layer reduced so that the solar beam passed through the same optical depth in each layer as it would if the model accurately handled the curved geometry of the problem. The results with this simple correction differed by less than 0.5% from the results presented above. The curvature would be much more important at a wavelength where light interacts more with the atmosphere.

3.5 Summary

The inability of plane-parallel snow-pack models, using a variety of phase functions, to reproduce the anisotropy observed in the reflected radiance field over the snow surface at Dome

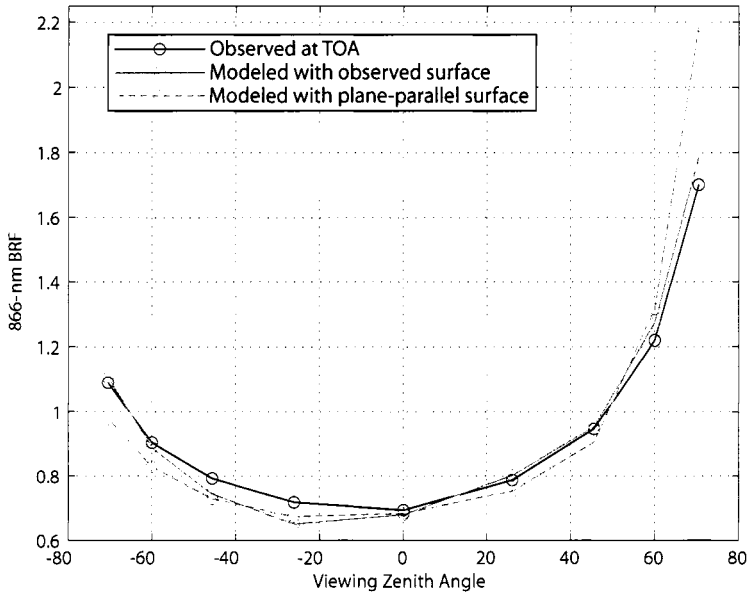

Figure 3.14: The observed 866-nm BRF at 1607 UTC 21 January 2004 from a clear location near Dome C is shown in black. The solid gray curve is the modeled TOA 866-nm BRF using the surface parameterization. The dashed gray curve shows the modeled BRF using a plane-parallel surface composed of aggregate ice crystals. The solar zenith angle is 85.0°.

C, combined with the fact that the error from all of these models is qualitatively in agreement with the expected effect of neglecting surface roughness, strongly suggests that the snow-surface roughness present on the Antarctic Plateau significantly alters the directional reflectance from the snow. Its effect is primarily to reduce the intensity at forward-reflected directions and to increase the intensity at other angles. This effect increases with solar zenith angle, and may be negligible at Dome C for solar zenith angles less than about 60°. Providing an accurate quantitative value for the magnitude of the effect of the surface roughness is an undertaking that will have to wait for computing improvements to allow for three-dimensional modelling of a realistic rough snow surface.

Plane-parallel models are able to calculate the reflected intensity field above clouds over the snow at Dome C if they use a parameterization of the reflectance from the snow surface at Dome C as the lower boundary. We showed good agreement between calculated and observed reflectance, for both clear and cloudy scenes, both near the surface and at the top of the atmosphere. Such

agreement was possible with the use of plane-parallel clouds, showing that the unexpected effects of having a cloud over the snow surface, a darkening of near-nadir views and brightening of forward-reflected views, is not caused by special properties of the clouds, but rather by the non-plane-parallel nature of the snow surface. Placing a cloud above the rough snow surface simply hides the snow-surface roughness with a surface that is, in units of optical depth, nearly plane parallel.

Clouds over snow affect the reflected radiance field most strongly and consistently near the principal plane, especially at large viewing zenith angles in the forward-scattering direction. Therefore, future projects wishing to accurately identify clouds over polar regions would benefit from the ability to observe at these angles. Instruments such as MISR, which can observe the same location from multiple angles near the principal plane in a short period, are especially well-suited for polar cloud identification using reflected natural light; however, future versions would need a wider swath width to fully cover the polar regions. Multi-angle instruments provide other benefits as well, such as stereo imaging to identify clouds.

Finally, the agreement between modeled and MISR-observed bidirectional reflectance at the top of the atmosphere, using the parameterized snow surface as the lower boundary in the model, indicates that this parameterization may be successfully used to model observations from satellites of the area around Dome C. This shows that, despite the differences in footprint size and angular field of view between satellite and near-surface observations, these types of field observations of directional reflectance from Earth's surfaces can be valuable tools for analyzing and interpreting satellite data. The effect of the surface roughness in this case, which can be observed only by going far enough above the surface to observe a fairly large footprint, shows that designers of such field programs must take care to ensure their measurements are representative of the large-scale views of the region if their data are to be used in this way.

Chapter 4

EVALUATION OF CERES OBSERVATIONS OVER ANTARCTICA

4.1 Introduction

The Clouds and the Earth's Radiant Energy System (CERES) is a suite of satellite-based instruments designed to monitor the Earth's radiation budget (Wielicki et al. 1996). The successor to the Earth Radiation Budget Experiment (ERBE), CERES is designed to double the accuracy of the ERBE observations through the use of improved instruments and analysis techniques. Data products produced by the CERES team include the observed broadband solar, window longwave, and broadband longwave radiances, along with many derived products, including fluxes in the three channels at the TOA and surface. The goals for absolute calibration of the CERES shortwave sensors is 1% or better.

CERES consists of five instruments on three satellites, and a sixth instrument to be placed on a satellite that will be launched in the future. Two of the satellites, Aqua and Terra, each have two instruments on board. These two are polar-orbiting satellites, so they frequently observe the East Antarctic Plateau, including the area around Dome C. In addition to the broadband radiance observations from the CERES instruments, the CERES algorithms make use of spectral observations from the Moderate Resolution Imaging Spectroradiometer (MODIS), which also flies on Aqua and Terra, to determine cloud fraction and properties. Another instrument useful for cloud studies, the Multiangle Imaging Spectroradiometer (MISR), also flies on the Terra satellite. MISR observes the same scene at four solar wavelengths from nine different viewing angles within 10 minutes. While not used in the CERES algorithms, MISR data are used here to evaluate model results.

One of the primary goals of the CERES experiment is to determine the TOA radiation budget of all regions of the planet. To do this the CERES workers must accurately convert their

instantaneous radiance observations to estimates of the instantaneous upwelling flux. Doing this conversion requires an angular distribution model (ADM) that predicts the radiance at all viewing angles, given the radiance at any one viewing angle. These ADMs were developed by combining all radiance observations made over a given surface type, with a given cloud fraction, and calculating the average radiance in each viewing angle bin as a function of solar zenith angle (Loeb et al. 2005). The ADMs that are of interest for observations made near Dome C are the permanent-snow ADMs, which are discussed in detail by Kato and Loeb (2005).

In this chapter I use an atmospheric radiative transfer model with the Dome-C parameterized surface bidirectional reflectance to calculate the upwelling solar radiance field at the TOA. Using these model results I provide an evaluation of the accuracy of the CERES radiance observations and the permanent-snow ADMs. I also examine how the atmosphere modifies the angular distribution of reflected radiance between the surface and TOA, and how variations in atmospheric properties may affect the TOA radiance field, introducing errors into the estimated fluxes.

4.2 Model

The model results presented here come from SBDART, a package for modelling radiative transfer in the atmosphere (Ricchiazzi et al. 1998). SBDART is built around the plane-parallel radiative transfer model DISORT (Stamnes et al. 1988), and uses the band models developed for LOWTRAN 7 for atmospheric gaseous absorption.

The model was modified to use the parameterizations presented in Chapter 2 to determine the BRF of the surface. Because these parameterizations do not cover all wavelengths or incidence angles, certain assumptions and extensions had to be made since CERES observes the full solar spectrum and the model must be able to calculate the BRF for all incidence angles to handle diffuse incidence. Three assumptions regarding the variation of R with incidence angle were made for all wavelengths: R at incidence angles greater than 86.6° is equal to the parameterized R at 86.6°; R at an incidence angle of 0° is equal to 1 at all viewing angles (isotropic reflectance); R at incidence angles between 0° and 51.6° is the linear interpolation, in cosine of the incidence angle, between the isotropic reflection at 0° and the parameterized R at 51.6°. At visible wavelengths R is not far from isotropic even at $\theta_o = 51.6°$, so little error should result from the interpolation.

All wavelengths between 0.2 and 0.8 μm used $R(\lambda = 0.8\ \mu m)$ to avoid the effect of diffuse radiation in the observations, as discussed in Section 2.5.3. For wavelengths with albedo between 0.2735 and 0.4687, R was determined with a new parameterization developed with data from wavelengths 1.39 to 1.51 μm. Interpolation in a lookup table of $R(\theta_v = 82.6°)$ as a function of albedo was used to find R for all incidence angles greater than 75° at wavelengths with albedo between 0.1537 and 0.2735. For wavelengths with albedo less than 0.1537, R was set to the parameterized values of R at albedo equal to 0.1537 if the incidence angle was less than 75°, or to $R(\alpha = 0.1537, \theta_v = 82.6°)$ if the incidence angle was greater than 75°.

The parameterization requires knowledge of the surface albedo under diffuse illumination at all wavelengths beyond 0.95 μm, but we measured albedo only at wavelengths out to 2.5 μm. To estimate the albedo at other wavelengths, SBDART was used to model the spectral albedo of a snow pack consisting of a 0.25-mm layer of 40-μm ice spheres above a semi-infinite layer of 90-μm ice spheres (the sizes that resulted in a best fit to our observations, as described in Section 3.4) at wavelengths from 0.2 to 10 μm under a cloud that diffused the solar beam. These albedo values were used in the parameterization at wavelengths where we did not observe the albedo.

The assumptions listed above allow the parameterizations to be extended to provide R for all necessary wavelengths and incidence angles, but DISORT needs the BRF, not R; the two differ by a factor of the surface albedo. In this case the surface albedo that is used should vary with incidence angle, especially important at near-infrared wavelengths. A table of albedo as a function of solar zenith angle ($\theta_v = 0°, 1°, 2°, \ldots, 89°$) and wavelength ($\lambda = 0.2 \times 1.016^n$, $n = 0, 1, 2, \ldots, 250$) was calculated with SBDART for the same snow pack as above, but with no atmosphere or cloud. Bilinear interpolation could then be used to determine the albedo at any wavelength between 0.2 and 10 μm and any incidence angle.

At this point the model can estimate the BRF of the surface at all necessary wavelengths and incidence angles. The importance of many of the assumptions and estimates that went into the model is diminished by the fact that most of them primarily affect wavelengths longer than 1.4 μm, where there is less incident solar radiation than at shorter wavelengths and where the snow has a low albedo (generally less than 0.3); about 85% of the incident solar flux and 94% to 98% of the reflected solar flux (depending on θ_o) at the TOA over Dome C is at wavelengths

shorter than 1.4 μm.

Below 28 km, the temperature, pressure, and water vapor profiles used as input to SBDART were specified as the mean of 47 radiosoundings conducted at Dome C during January 2004. Ozone concentration at all heights, and all quantities above 28 km, were taken from the summertime South Pole model atmosphere of Walden et al. (1998), who used ozonesonde data for ozone concentrations below 30 km, and various satellite data for all quantities above 30 km. No aerosols were used in the model; the mean observed clear-sky aerosol optical thickness at Dome C during summer 2003–2004 was 0.02 at 0.44 μm and 0.007 at 0.87 μm (Six et al. 2005). Running the model with a layer of stratospheric aerosols with optical depth 0.02 at 0.55 μm resulted in reflected flux calculations that differ from the standard model by 0.008% at $\theta_\circ = 59°$ and by 0.13% at $\theta_\circ = 80°$, and resulted in reflected radiance calculations that differ from the standard model by less than 1% at $\theta_\circ = 59°$ and by less than 4.5% at $\theta_\circ = 80°$, for $\theta_v \leq 70°$ (those most important to CERES). Radiance differences exceed 10% at large θ_v in the forward-reflected direction.

The model was run, with thermal emission turned off, over the wavelength range 0.2 to 10 μm, with a wavelength interval of 0.02 times the current wavelength, resulting in 196 wavelengths, more closely spaced at shorter wavelengths, where the majority of the reflected energy is. DISORT was run with 24 streams and with its intensity correction algorithm turned on (Nakajima and Tanaka 1988).

For the comparisons with CERES observations in Section 4.3, the model was run at 1-degree solar-zenith-angle intervals and output was saved at 2-degree viewing-zenith-angle intervals and 3.75-degree relative-azimuth-angle intervals. The modeled radiance at the solar zenith angle and viewing geometry of the CERES observations was then determined by interpolating the stored radiances in solar zenith, viewing zenith, and relative azimuth angles.

For the comparisons with MISR observations in Section 4.3, the model was run at the central wavelengths of the 4 MISR channels (0.4464, 0.5575, 0.6717, and 0.8664 μm) at 0.5-degree intervals of solar zenith angle. Output was saved at intervals of 3.75° in relative azimuth angle, at the MISR viewing zenith angles (0°, 26.1°, 45.6°, 60.0°, and 70.5°). The comparisons were then made with the nearest modeled solar zenith angle and relative azimuth angle to the observation.

For the results in Section 4.4, the model was run and output saved at the bin-center an-

gles used in the CERES ADMs ($\theta_o = 1°, 3°, 5°, \ldots, 89°$; $\theta_v = 2.5°, 7.5°, 12.5°, \ldots, 87.5°$; $\phi = 2.5°, 7.5°, 12.5°, \ldots, 177.5°$), and the comparisons were then made directly.

4.3 Comparison with Individual Observations

To try to assess the accuracy of CERES radiance and flux data from observations over the area around Dome C, modeled radiances and fluxes are compared with CERES observations from this region. CERES data with surface footprints lying within 200 km of Dome C were gathered from 3 days in January 2004 and 1 day in January 2005, during times when our surface observations indicated that skies were clear of clouds and boundary-layer ice crystals at Dome C for at least 6 hours. This provided 23,257 radiance observations that were used by CERES to determine fluxes (with $\theta_o < 86.5°$ and $\theta_v < 70.0°$). Of these observations, 20,700 were identified by CERES as having clear skies, and only these observations were used in the comparison.

The relative difference between each CERES radiance observation and the modeled radiance at the same solar zenith, viewing zenith, and relative azimuth angles was calculated, along with the relative difference between each CERES flux calculation and the modeled flux at the same solar zenith angle. The results are summarized, as functions of solar or viewing zenith angle, in Figures 4.1 to 4.4. In each of these figures, the data are grouped into 2-degree bins in θ_o or 5-degree bins in θ_v, and are summarized with box plots that show, for each bin, the median difference, the upper and lower quartiles, the range of differences nearer the median than 1.5 times the interquartile range, and any outliers. The figures also show the number of observations in each bin, which varies significantly in Figures 4.1 and 4.2 because the satellites' orbits cause them to pass near Dome C most often in mid-morning and late-evening.

The general pattern seen in these figures is that the CERES radiances and fluxes are smaller than the modeled values, with a median difference of about 5%. Comparing Figure 4.1 with 4.2, or Figure 4.3 with 4.4, we see that the outlying data with large negative differences in the radiance plots have the magnitude of their differences significantly reduced in the flux plots. This is due to differences between the model and CERES anisotropic reflectance patterns (see Section 4.4), which cause the relative error in the flux estimate to differ from the relative error in the radiance measurement.

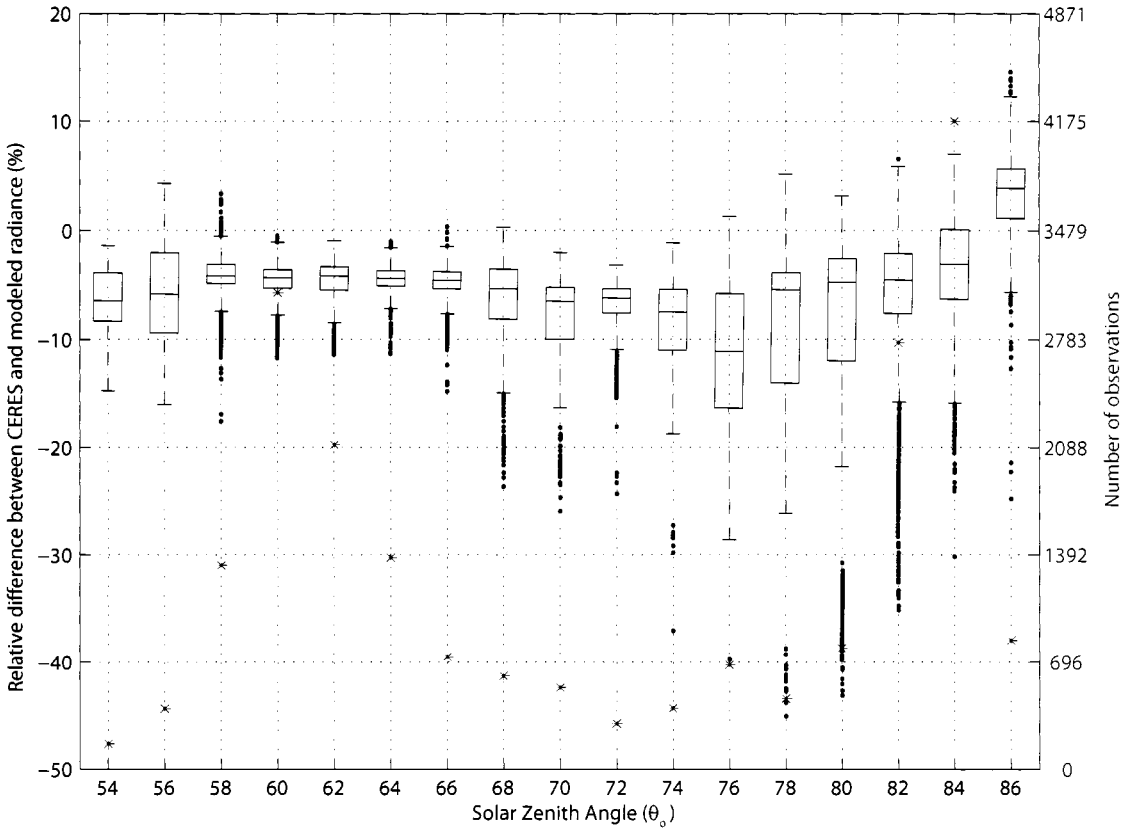

Figure 4.1: The box plots show the relative difference between the CERES-observed and the modeled radiance [$100 \times$ (CERES $-$ model)/model] within 200 km of Dome C, as a function of solar zenith angle; they show the median, upper and lower quartiles, and the whiskers extend to the most extreme value nearer the median than $1.5\times$ the interquartile range, with more extreme values shown individually with dots. The number of observations used to create each box plot is shown by the red asterisks and the right-hand axis. Negative values indicate that CERES radiance is less than the model radiance.

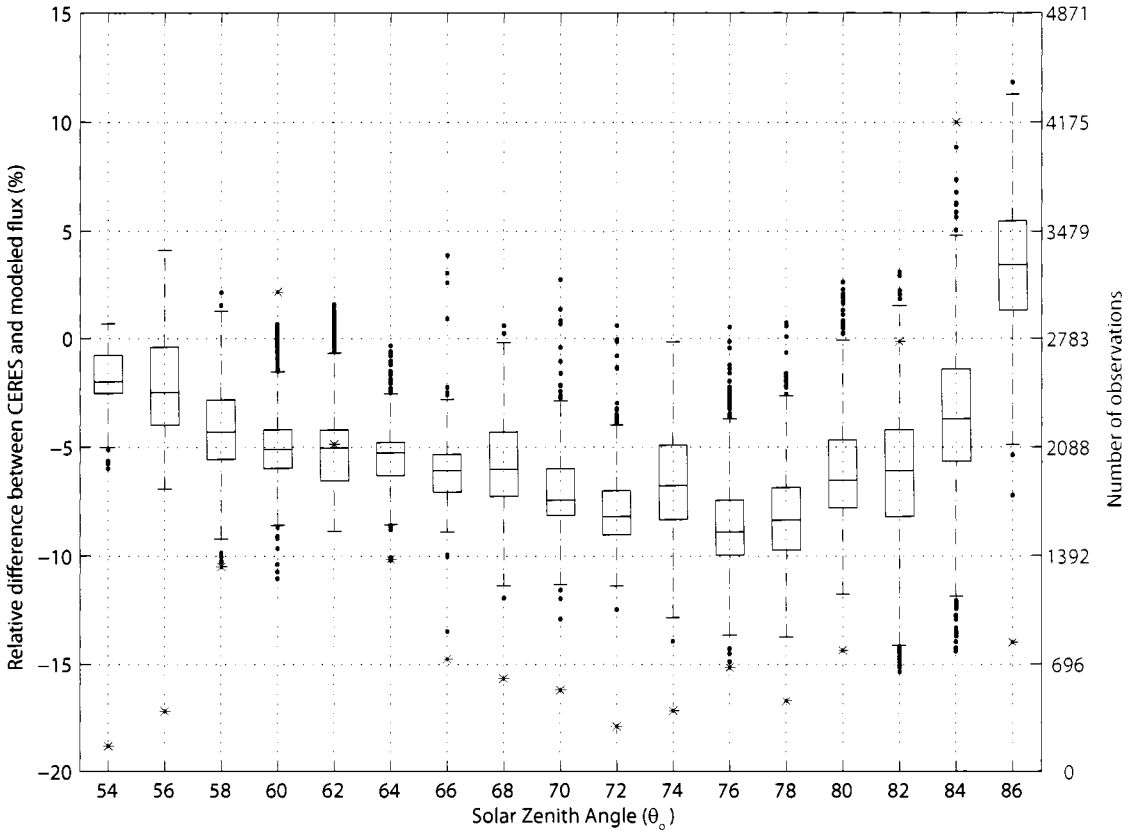

Figure 4.2: The box plots show the relative difference between the CERES-derived and the modeled flux within 200 km of Dome C, as a function of solar zenith angle; they show the median, upper and lower quartiles, and the whiskers extend to the most extreme value nearer the median than 1.5× the interquartile range, with more extreme values shown individually with dots. The number of observations used to create each box plot is shown by the red asterisks and the right-hand axis. Negative values indicate that CERES flux is less than the model flux. The scale on the left axis differs from Figure 4.1.

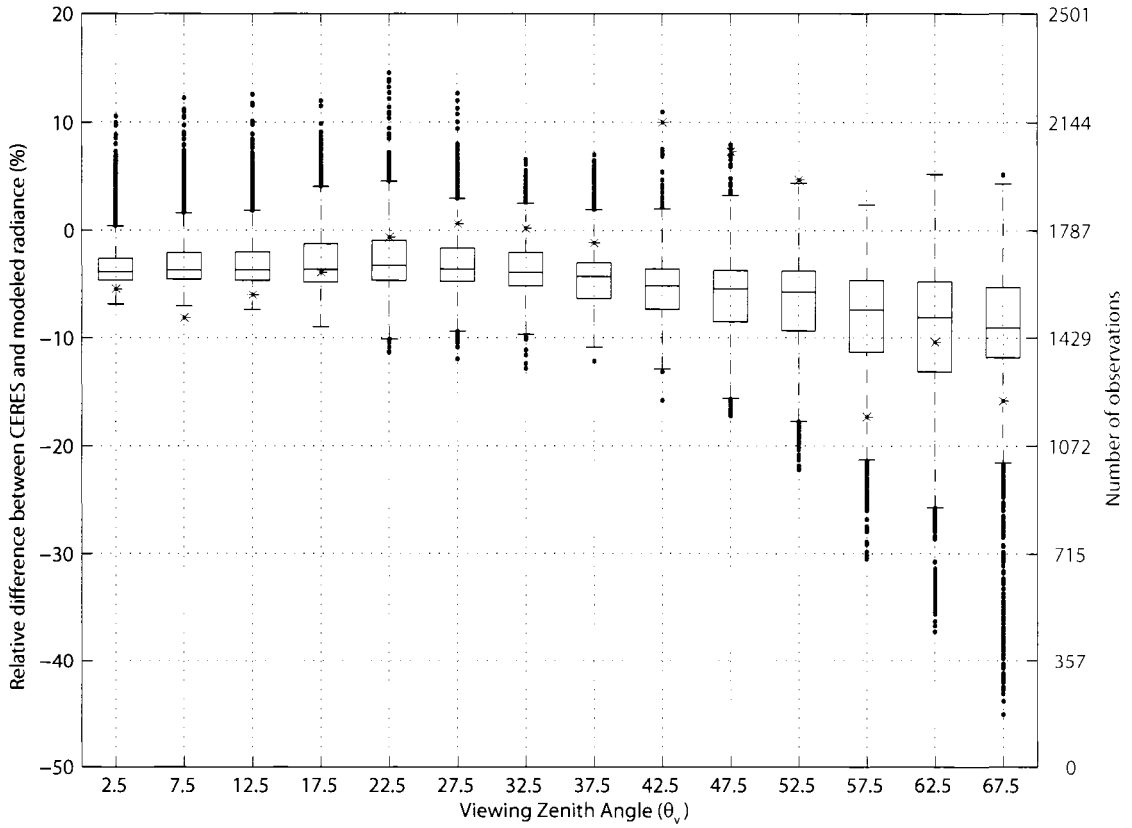

Figure 4.3: The box plots show the relative difference between the CERES-observed and the modeled radiance within 200 km of Dome C, as a function of viewing zenith angle; they show the median, upper and lower quartiles, and the whiskers extend to the most extreme value nearer the median than 1.5× the interquartile range, with more extreme values shown individually with dots. The number of observations used to create each box plot is shown by the red asterisks and the right-hand axis. Negative values indicate that CERES radiance is less than the model radiance.

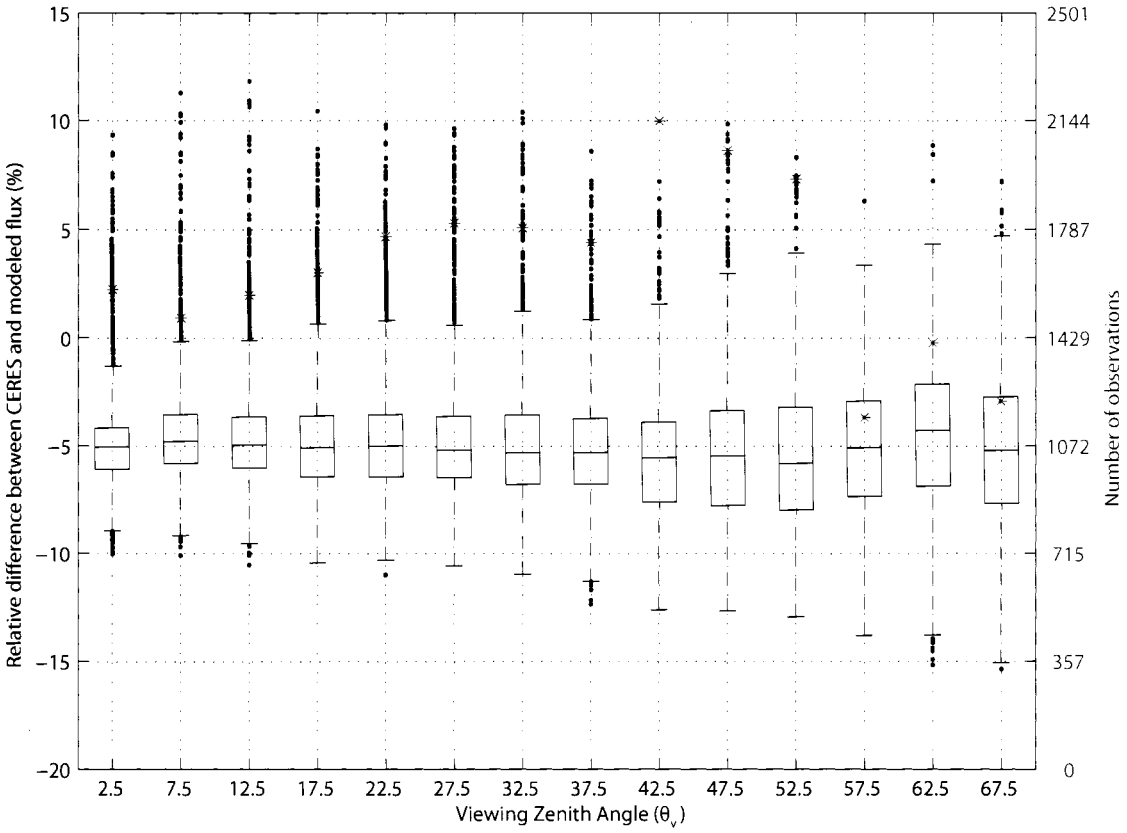

Figure 4.4: The box plots show the relative difference between the CERES-derived and the modeled flux within 200 km of Dome C, as a function of viewing zenith angle; they show the median, upper and lower quartiles, and the whiskers extend to the most extreme value nearer the median than 1.5× the interquartile range, with more extreme values shown individually with dots. The number of observations used to create each box plot is shown by the red asterisks and the right-hand axis. Negative values indicate that CERES flux is less than the model flux. The scale on the left axis differs from Figure 4.3.

Those large differences represent a small fraction of the data; fewer than 1.1% of the observations differ from the model by more than 25%, and about 80% of the observations differ from the model by between 0 and -10%, with a median of -4.3%. The only observations in which the CERES radiances or fluxes are systematically larger than the modeled values are those made when the solar zenith angle was very large. At these large solar zenith angles, a significant fraction of the reflected light at the TOA did not enter the atmosphere above the observation location, but was scattered through the atmosphere to that location; the plane-parallel model used here does not account for this scattered light, which entered the atmosphere at a smaller zenith angle as a result of the Earth's curvature. The model also overestimates the atmospheric pathlength, compared to the real pathlength through the spherical atmosphere, therefore causing too much absorption.

Some scatter is to be expected in comparisons between CERES observations and the model since the model has an atmosphere and snow surface that are representative of average summer conditions at Dome C, but the CERES observations see both spatial and temporal variability. However, the consistent bias seen in the Figures 4.1 to 4.4 suggests that the model overestimates the reflectance, or that CERES underestimates the reflectance, or that some combination of these is occurring. To try to see if the model is overestimating the reflectance for some reason, modeled reflected radiances at four wavelengths were compared with the radiances observed by MISR on four overpasses of Dome C.

Two representative examples of these comparisons are shown in Figures 4.5 and 4.6. In these comparisons, the shape of the modeled reflectance versus viewing zenith angle compares well with the MISR observations. In only 3 of the 144 individual comparisons (4 overpasses with 9 cameras, each with 4 channels), the model calculated a radiance that was above the observed range, and these were all at nadir views, where our parameterizations are less reliable due to a lack of data. All other individual comparisons, like those shown here, had model radiances within or below the range of observed radiances.

The absolute uncertainty in MISR radiances is estimated to be within 4% (1 standard deviation level of confidence) for bright uniform targets (MISR Science Team 2004; Bruegge et al. 2002). So, while the comparison of the model with MISR does not provide proof that CERES is

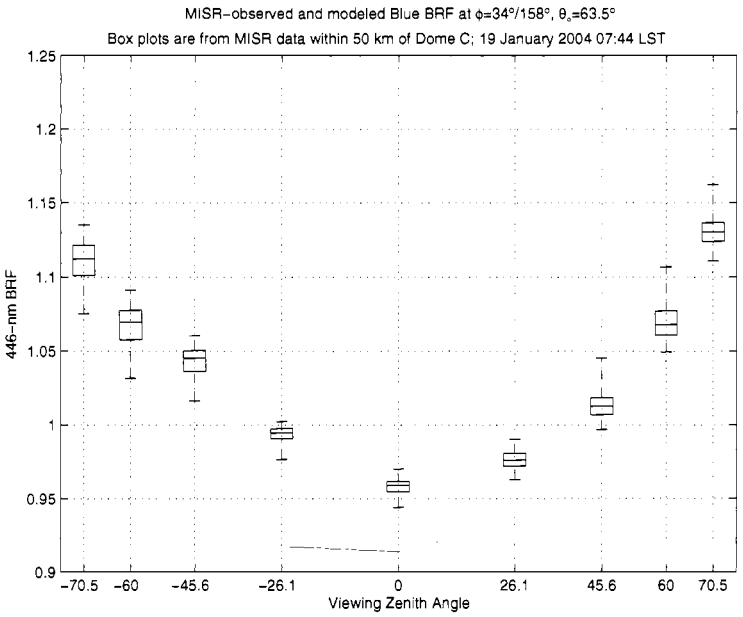

Figure 4.5: The box plots show MISR blue-channel BRF observations from within 50 km of Dome C during one overpass, at 07:44 LST 19 January 2004 (23:44 UTC 18 January 2004); they show the median, upper and lower quartiles, and the range. The modeled BRF for the same solar zenith angle and relative azimuth angles is shown in red.

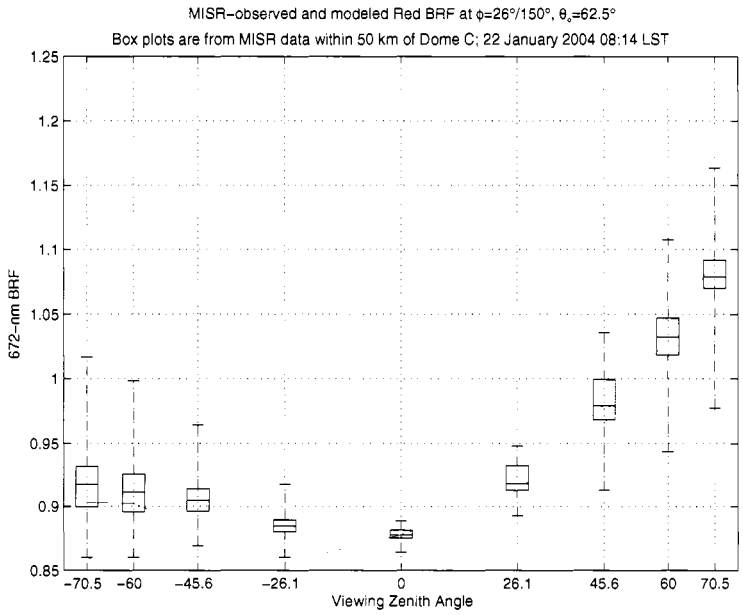

Figure 4.6: The box plots show MISR red-channel BRF observations from within 50 km of Dome C during one overpass, at 08:14 LST 22 January 2004 (00:14 UTC 22 January 2004); they show the median, upper and lower quartiles, and the range. The modeled BRF for the same solar zenith angle and relative azimuth angles is shown in red.

underreporting the reflected radiance near Dome C, it does suggest that the error may be in the CERES observations rather than the model. This supports previous findings by the CERES science team that suggest CERES radiances are too low (Seiji Kato, personal communication 2007; Thomas Charlock, personal communication 2006).

4.4 Comparison with Angular Distribution Models

The CERES team has developed two sets of ADMs for clear-sky observations over permanently snow-covered surfaces: a bright permanent snow ADM and a dark permanent snow ADM (Kato and Loeb 2005). This brightness distinction was made to try to account for some of the snow-property changes that can affect the distribution of reflected radiance. MODIS 0.645-μm reflectance observations near nadir during the two-year ADM-development data set were used to classify permanent-snow regions as bright or dark, based on whether their monthly-mean reflectance was greater or less than the mean reflectance from permanent snow (the evaluation was done as a function of solar zenith angle). Operationally, the CERES algorithms choose the bright or dark ADM based on which one more closely matches the observation. As shown below, the main difference between the two ADMs is their albedo.

Each ADM provides the TOA albedo as a function of solar zenith angle and the TOA R as a function of solar zenith angle and viewing angles. They were developed using all clear-sky permanent snow scenes observed by CERES, mostly the Greenland and Antarctic ice sheets. In this section they are compared with the TOA modeled reflectance over Dome C. Since data from lower-elevation sites with higher precipitable water and from locations and times with varying ozone concentrations were included in the ADM development, an exact match between the ADMs and the model should not be expected; nevertheless, the ADMs are used over Dome C, so these comparisons provide a useful estimate of their uncertainty.

Figure 4.7 compares the albedo from the ADMs with that from the model. The different shape of the curves at large solar zenith angles is due to the different geometry of the atmosphere and model, as discussed in Section 4.3. At other solar zenith angles there is a general trend of slightly increasing albedo with solar zenith angle. This trend is caused by the increase in surface albedo with increase in solar zenith angle, especially at near-infrared wavelengths. The model albedos

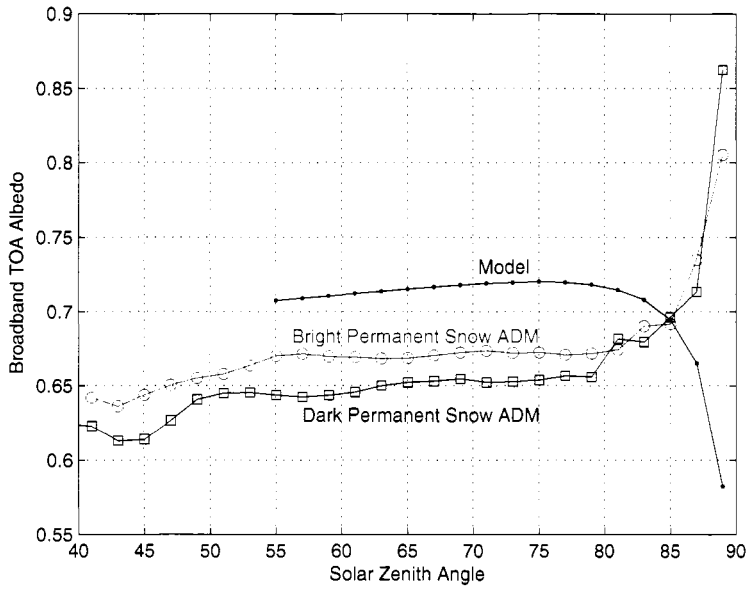

Figure 4.7: A comparison of broadband albedos, versus solar zenith angle, at the TOA from the CERES operational permanent snow ADMs and from our model.

are higher than the ADM albedos by about 0.05, consistent with the difference in individual observations presented above.

Dome C is one of the higher, drier permanent snow regions, with only 0.7 mm of precipitable water in the model summertime atmosphere used here. To see if this lack of water vapor could account for the albedo difference seen here, the model was run with a solar zenith angle of 75°, using the subarctic winter atmosphere (McClatchey et al. 1972), which contains 4 mm of precipitable water. Using this atmosphere reduced the model albedo from 0.720 to 0.654, in line with the ADM albedos. Thus the albedo difference could be explained if most of the permanent snow seen by CERES had high values of water vapor. However, while the varying water-vapor amounts may account for some of the difference seen in Figure 4.7, there are other issues that suggest it is not likely to explain all of the difference. First, most of Antarctica has less precipitable water than the subarctic winter atmosphere, according the the NCEP/NCAR Reanalysis January mean. Second, the subarctic winter atmosphere has a column ozone amount of 486 Dobson units, about 75% more than the January Antarctic atmosphere, according to NOAA-GMD ozonesonde data

and to Global Ozone Monitoring Experiment data (Burrows et al. 1999). Third, Antarctica has 8 times the area of Greenland, so most of the permenent snow used by CERES to develop ADMs would have had water-vapor amounts far lower than Arctic values. Finally, a separate comparison was made with non-operational CERES ADMs developed by Seiji Kato (personal communication) with data from only the region around Dome C, and it showed similar differences between the model and ADM albedos.

Comparisons of anisotropic reflectance factors, which remove the effect of varying albedo, are shown in Figure 4.8. This figure shows the modeled values of R at two solar zenith angles and the difference between the values of R from the ADMs and the values of R from the model. These plots show that, despite the different regions included in the CERES ADM development, they appear to be appropriate for use over Dome C, one of the more extreme locations in the permanent-snow regions.

Most CERES observations that are used operationally are made with $\theta_v < 70°$. At these angles, the differences between R from the CERES ADMs and R from the Dome-C model are mostly smaller than 5%. Larger errors are found at large θ_v, possibly due to including observations over moister atmospheres, since increased water-vapor concentrations would affect R more at large θ_v, where the atmospheric path length is longer. These differences could also be due to other spatial or temporal variability, or to procedures used in the ADM development, in which viewing angles without data were filled with model results. Alternatively, they could represent error in the Dome-C model.

4.5 Variation in Angular Distribution Models Due to the Atmosphere

Since the method used to develop the CERES ADMs for regions of permanent snow combines all permanent-snow scenes, regardless of surface elevation or atmospheric water vapor or ozone concentrations, it is important to determine how much uncertainty may be introduced into the CERES flux calculations as a result of spatial and temporal variations in R at the TOA due to atmospheric variations. This section assesses this variation by running the model described above with a variety of different atmospheres and examining how the TOA R changes.

Figure 4.9 shows a selection of the results. The overall message of this figure is that the

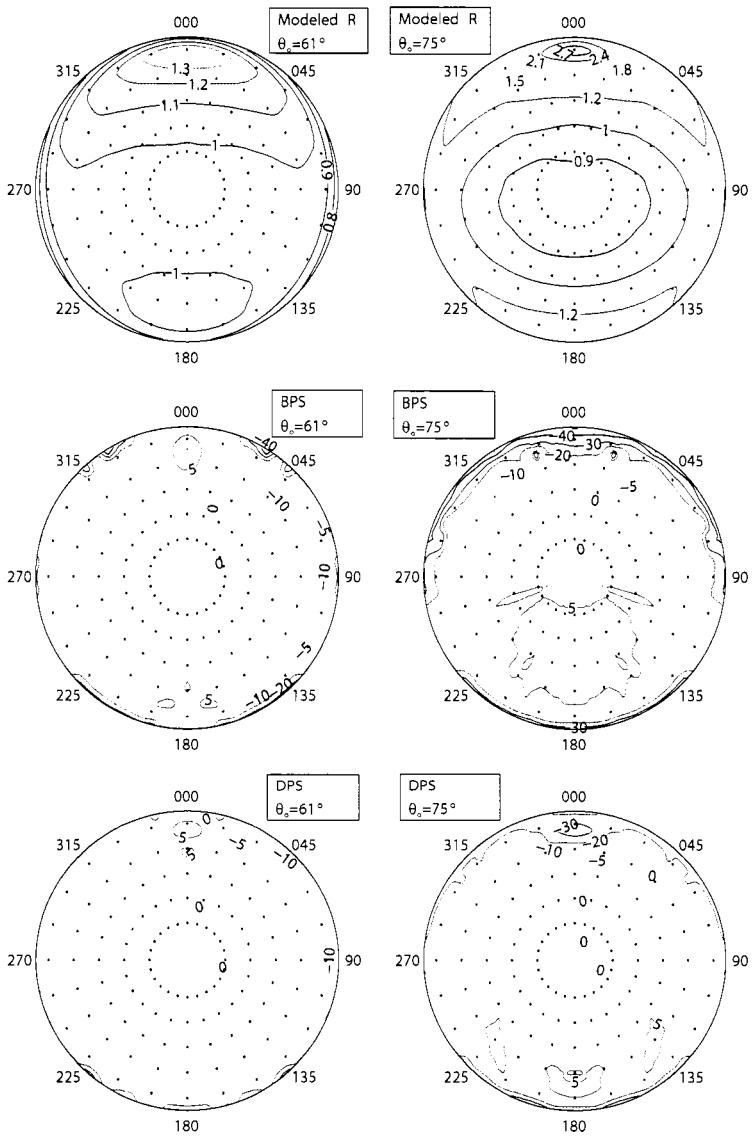

Figure 4.8: The top plots show the modeled TOA R values at solar zenith angles of 61° and 75°. The middle and bottom plots show the relative difference (%) between R from the CERES bright (BPS) and dark (DPS) permanent snow ADMs and the modeled R at the same two solar zenith angles. Negative differences indicate CERES R is less than the modeled R. Dots are located every 15 degrees in ϕ and at θ_v of 22.5°, 37.5°, 52.5°, 67.5°, and 82.5°.

expected variations in the atmosphere do not have a very large effect on R at the TOA, as long as $\theta_v < 70°$, which is generally the case for CERES observations.

The top two plots show the relative change in TOA R caused by switching from the Dome C summer atmosphere to the subarctic winter atmosphere. There are three main differences between the two atmospheres that are important to solar radiation: the subarctic winter atmosphere contains nearly six times as much water vapor (4.18 mm of precipitable water compared to 0.72 mm) and about 70% more ozone (486 Dobson Units compared to 284 Dobson Units), and it has 56% more atmospheric mass (surface pressure of 1013 mb compared to 650 mb), which affects Rayleigh scattering and the total amount of carbon dioxide. These two atmospheres are nearly the extremes of the summer-mean atmospheres found over ice sheets. Some parts of Greenland or coastal Antarctica may sometimes have more water vapor than the subarctic winter atmosphere; ozone amounts are rarely greater than that in the subarctic winter atmosphere, but may be less than that in the Dome C atmosphere, especially in spring over Antarctica; surface pressure and total water vapor can be slightly lower than the Dome C atmosphere over the higher parts of Antarctica.

These top two plots in Figure 4.9 show that variations in the atmosphere above different permanent snow surfaces are not likely to introduce significant uncertainty into the CERES radiance-to-flux conversions. At $\theta_o = 60°$, the variations in R are less than 4% at all viewing angles important to CERES, and at $\theta_o = 80°$, they exceed 4% only near the forward reflectance peak, a region where R is likely to vary for other reasons as well, including surface-roughness and snow-grain-shape variations. These variations in TOA R are less than or similar to day-to-day variations in the surface R observations from Dome C, discussed in Section 2.3.4.

The lower-left and middle two plots in Figure 4.9 are intended to dissect the various contributions to the top-left plot. They show the effects of individual atmospheric changes with $\theta_o = 60°$. An increase in ozone has a significant effect on R only at very large θ_v, a result that also holds true with $\theta_o = 80°$ (not shown). Likewise, a six-fold increase in column water-vapor amount causes less than 1.5% change in R at most θ_v; this effect approaches 3% at $\theta_v = 75°$, $\phi = 0°$, with $\theta_o = 80°$ (not shown). Increasing the concentration of all well-mixed gases to bring the surface pressure to that at sea level (the total amounts of water vapor and ozone were not changed) en-

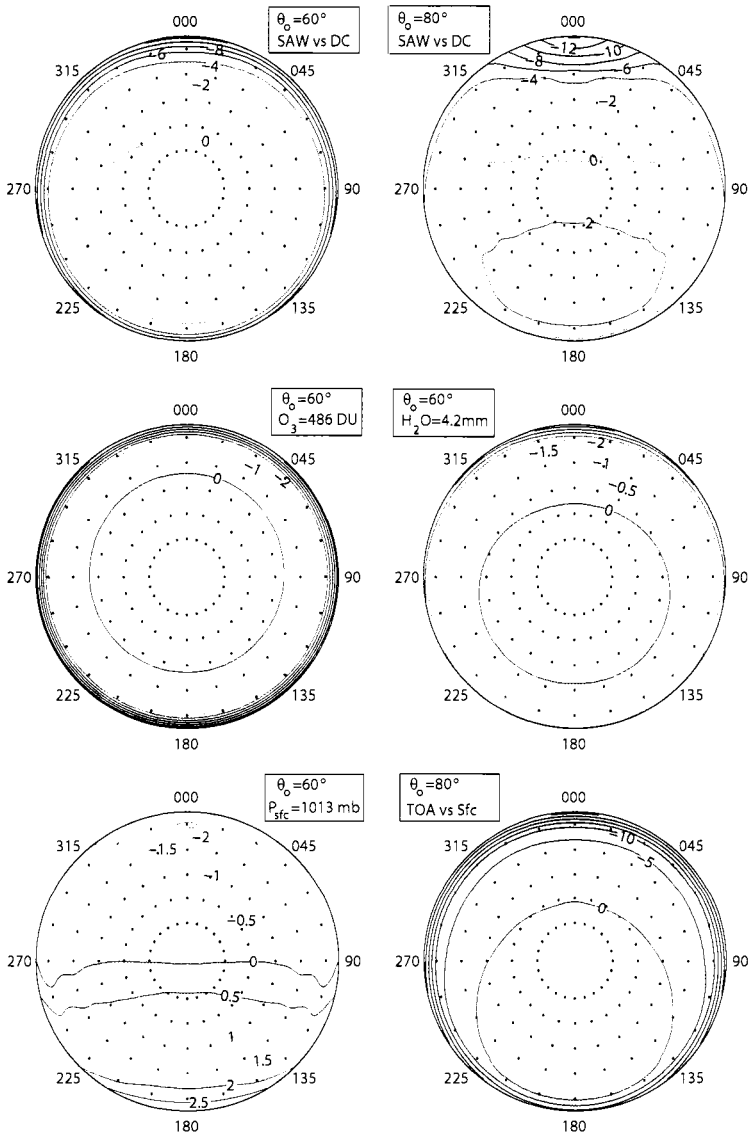

Figure 4.9: The top two plots contour the relative difference (%) between modeled TOA R above the subarctic winter (SAW) atmosphere and that above the Dome C atmosphere (negative values indicate lower values over the SAW atmosphere), for solar zenith angles 60° and 80°. The middle two and the bottom-left plots show the relative difference (%) between modeled TOA R above a modified Dome C atmosphere relative to that above the standard Dome C atmosphere (negative values indicate lower values above the modified atmosphere), all with solar zenith angle 60°. The modifications were an increase in total column ozone from 284 to 486 Dobson Units, or an increase in total column water vapor from 0.7 to 4.2 mm of precipitable water, or an increase in surface pressure from 650 to 1013 mb (without changing total column ozone or water vapor amounts). The lower-right plot contours the relative difference (%) between the modeled TOA and surface values of R with the unmodified Dome C atmosphere and solar zenith angle 60° (negative values indicate R is lower at the TOA).

hances the amount of Rayleigh scattering, causing changes in R of up to about 2%; this increases to about 6% at large θ_v near the principal plane when $\theta_o = 80°$.

All of the changes just discussed lower the TOA albedo, by about 2.3%, 3.6%, and 1.3% (relative decrease in albedo, from 0.71) for the ozone, water-vapor, and pressure changes with $\theta_o = 60°$. The relative decrease in albedo caused by switching to the subarctic winter atmosphere is 7.4%, nearly equal to the sum of the three individual changes. These albedo changes can be captured by the CERES algorithms if they occur without significant alterations to R. At most viewing angles the variation in R is much less than the albedo change, except for the run with increased surface pressure.

The lower-right plot in Figure 4.9 shows the relative difference between R at the TOA and at the surface, with $\theta_o = 60°$. Because light reflected by the surface into large nadir angles must travel through a longer atmospheric path to reach the TOA, it is more likely to be absorbed on the way. This results in the general pattern seen here, that the atmosphere decreases R at large θ_v. The effect of the atmosphere is not symmetric because Rayleigh scattering is much more isotropic than the snow-grain scattering, which causes the R at the TOA to be more nearly isotropic than R at the surface. A secondary reason the atmospheric effect is not symmetric is that light scattered into the backward peak of the Rayleigh phase function will enhance TOA backscatter, while light scattered into the forward peak of the Rayleigh phase function will be directed toward the surface. The lower-left plot shows the asymmetric effect of the atmospheric scattering.

4.6 Summary

The parameterizations presented in Chapter 2 provide a realistic lower boundary condition for use in modelling radiative transfer at solar wavelengths over the East Antarctic Plateau. Here they have been extended to cover the full solar spectrum, allowing for the calculation of reflected solar radiance and flux.

Comparisons of modeled TOA radiance and flux with CERES observations of radiance and estimates of flux showed that the CERES values are generally lower than the modeled values by about 5%. A comparison of modeled and MISR-observed radiances suggeted that the model is not overestimating the reflectance. These results support earlier suspicions that there may be a

negative bias in the CERES observations.

The CERES ADMs for permanent snow scenes were compared with the model results. As expected from the observation that CERES TOA fluxes are lower than those from the model, the albedos from the ADMs were less than the albedos from the model at solar zenith angles where the plane-parallel model works well. The angular distribution of the reflected radiance in the ADMs was compared with the model by removing the effect of differing albedo and comparing patterns of R. These comparisons showed that the CERES permanent-snow ADMs are appropriate for use over Dome C, with their values of R differing from the modeled values by less than 5% at most geometries.

Finally, the effect of the atmosphere and of variations in the atmosphere on TOA R was examined through modelling results. While the atmosphere significantly alters R from the values seen at the surface, especially at large θ_v, expected variability in atmospheric properties over permanently snow-covered areas do not cause large changes to TOA R. This result shows that the choice to combine all permanently snow-covered regions in the development of the ADMs may not limit the accuracy of the CERES fluxes.

Chapter 5

CONCLUSION AND FUTURE WORK

This thesis presented a set of parameterizations that accurately give the anisotropic reflectance factor of the snow surface of the high parts of the East Antarctic Plateau. These parameterizations were developed from an extensive set of observations made from 32 m above the surface, and they account for the surface roughness found at Dome C.

Comparison of the reflectance from modeled snow surfaces in plane-parallel models to those of the parameterizations were used to show that the effect of the snow-surface roughness on the directional reflectance is to reduce forward-reflected intensities and enhance backward-reflected intensities. This modification of the anisotropy of the reflected light helps explain the difficulty researchers have had in trying to explain observations of the effect of clouds on TOA reflectance over snow-covered scenes. Here it was argued that the main reason clouds over snow reduce the intensity of reflected light near nadir and enhance the intensity near the forward peak is that the clouds hide the surface roughness with a surface that is, optically, nearly plane-parallel.

Finally, the parameterizations were used for modelling the reflectance from near Dome C, integrated over the solar spectrum. These results allowed for an evaluation of CERES data and algorithms. Comparison of the model results with individual CERES observations suggested that the CERES instruments may be reporting radiances that are biased low, by about 5%. Some work by members of the CERES science team has also suggested a similar bias, though it has not been confirmed. Comparisons of the anisotropic reflectance patterns in the ADMs used by CERES to convert radiance to flux over permanent snow surfaces, to the values from the model, showed that there was generally good agreement between the two. This indicates that, if the CERES radiances are correct, they should be able to accurately determine the flux over the East Antarctic Plateau. Furthermore, modelling the reflectance with different atmospheric properties had relatively small effects on the TOA anisotropy, suggesting the accuracy of CERES fluxes is

not likely to be significantly affected by spatial or temporal variations in the atmosphere above mid- to high-elevation permanent snow surfaces. This work did not address whether spatial or temporal variations in the surface roughness features on permanent snow surfaces could affect the accuracy of the flux conversion.

The modelling work presented in this thesis has shown that these parameterizations provide a way of specifying the snow-surface bidirectional reflectance in plane-parallel atmospheric radiation models, which otherwise are unable to include the effects of surface roughness on the snow-surface anisotropy. The comparisons with satellite observations showed the benefits of using an accurate parameterization to specify the reflectance from the snow surface. These parameterizations should be useful to members of the satellite-remote-sensing community who are working on observations made over Antarctica.

There is more work to be done with CERES, and I plan to work with Seiji Kato, the member of the CERES team responsible for the ADMs for snow-covered scenes, to continue to examine the ADMs, investigate what are the principal sources of uncertainty in them, and see if they can be improved. He is currently using results from the model described in Chapter 4 to see if they can help improve the ADMs. This work looked at CERES data and procedures only from clear scenes. Much could also be done to evaluate the system's performance over cloudy scenes, and the parameterizations should prove useful for this as well, especially when the clouds are thin.

Modelling studies using these parameterizations could also be used to address questions about the Antarctic climate system. If summertime cloud properties and frequency can be accurately determined then the shortwave cloud radiative forcing, which remains uncertain, could be modeled. This method would allow for the determination of the effect of various types of clouds, in addition to an estimate of the overall forcing due to clouds. This is just one idea for how these parameterizations may be used in the future.

BIBLIOGRAPHY

Aoki, T., T. Aoki, M. Fukabori, A. Hachikubo, Y. Tachibana and F. Nishio, 2000: Effects of snow physical parameters on spectral albedo and bidirectional reflectance of snow surface. *J. Geophys. Res.*, **105**(D8), 10,219–10,236.

Arnold, G. T., S.-C. Tsay, M. D. King, J. Y. Li and P. F. Soulen, 2002: Airborne spectral measurements of surface-atmosphere anisotropy for arctic sea ice and tundra. *Int. J. Remote Sens.*, **23**(18), 3763–3781.

Bruegge, C. J., N. L. Chrien, R. R. Ando, D. J. Diner, W. A. Abdou, M. C. Helmlinger, S. H. Pilorz and K. J. Thome, 2002: Early validation of the Multi-angle Imaging SpectroRadiometer (MISR) radiometric scale. *IEEE Trans. Geosci. Remote Sens.*, **40**(7), 1477–1492.

Burrows, J. P., M. Weber, M. Buchwitz, V. Rozanov, A. Ladstätter-Weißenmayer, A. Richter, R. DeBeek, R. Hoogen, K. Bramstedt, K.-U. Eichmann and M. Eisinger, 1999: The Global Ozone Monitoring Experiment (GOME): Mission concept and first scientific results. *J. Atmos. Sci.*, **56**(2), 151–175.

Dozier, J., 1989: Estimation of properties of alpine snow from landsat thematic mapper. *Adv. Space Res.*, **9**(1), 207–215.

Fahnestock, M. A., T. A. Scambos, C. A. Shuman, R. J. Arthern, D. P. Winebrenner and R. Kwok, 2000: Snow megadune fields on the East Antarctic Plateau: extreme atmosphere-ice interaction. *Geophys. Res. Lett.*, **27**(22), 3719–3722.

Grenfell, T. C., S. G. Warren and P. C. Mullen, 1994: Reflection of solar radiation by the Antarctic snow surface at ultraviolet, visible, and near-infrared wavelengths. *J. Geophys. Res.*, **99**(D9), 18,669–18,684.

Hatzianastassiou, N., N. Cleridou and I. Vardavas, 2001: Polar cloud climatologies from ISCCP C2 and D2 datasets. *J. Climate*, **14**(18), 3851–3862.

Irvine, W. M. and J. B. Pollack, 1968: Infrared optical properties of water and ice spheres. *Icarus*, **8**(1–3), 324–360.

Kato, S. and N. G. Loeb, 2005: Top-of-atmosphere shortwave broadband observed radiance and estimated irradiance over polar regions from Clouds and the Earth's Radiant Energy System (CERES) instruments on Terra. *J. Geophys. Res.*, **110**, D07202.

Kindel, B. C., Z. Qu and A. F. H. Goetz, 2001: Direct solar spectral irradiance and transmittance measurements from 350 to 2500 nm. *Appl. Opt.*, **40**(21), 3483–3494.

Kokhanovsky, A. A., T. Aoki, A. Hachikubo, M. Hori and E. P. Zege, 2005: Reflective properties of natural snow: Approximate asymptotic theory versus *in situ* measurements. *IEEE Trans. Geosci. Remote Sens.*, **43**(7), 1529–1535.

Kuhn, M., 1985: Bidirectional reflectance of polar and alpine snow surfaces. *Ann. Glaciol.*, **6**, 164–167.

Leroux, C., J.-L. Deuzé, P. Goloub, C. Sergent and M. Fily, 1998: Ground measurements of the polarized bidirectional reflectance of snow in the near-infrared spectral domain: Comparisons with model results. *J. Geophys. Res.*, **103**(D16), 19,721–19,731.

Leroux, C. and M. Fily, 1998: Modeling the effect of sastrugi on snow reflectance. *J. Geophys. Res.*, **103**(E11), 25,779–25,788.

Leroux, C., J. Lenoble, G. Brogniez, J. W. Hovenier and J. F. De Haan, 1999: A model for the bidirectional polarized reflectance of snow. *J. Quant. Spectrosc. Radiat. Trans.*, **61**(3), 273–285.

Li, J., W. P. Menzel, Z. Yang, R. A. Frey and S. A. Ackerman, 2003: High-spatial-resolution surface and cloud-type classification from MODIS multispectral band measurements. *J. Appl. Meteorol*, **42**(2), 204–226.

Li, S. and X. Zhou, 2004: Modelling and measuring the spectral bidirectional reflectance factor of snow-covered sea ice: an intercomparison study. *Hydrol. Process.*, **18**(18), 3559–3581.

Loeb, N. G., 1997: In-flight calibration of NOAA AVHRR visible and near-IR bands over Greenland and Antarctica. *Int. J. Remote Sens.*, **18**(3), 477–490.

Loeb, N. G., S. Kato, K. Loukachine and N. Manalo-Smith, 2005: Angular distribution models for top-of-atmosphere radiative flux estimation from the Clouds and the Earth's Radiant Energy System instrument on the *Terra* satellite. Part I: Methodology. *J. Atmos. Oceanic Technol.*, **22**(4), 338–351.

Loeb, N. G., T. Várnai and D. M. Winker, 1998: Influence of subpixel-scale cloud-top structure on reflectances from overcast stratiform cloud layer. *J. Atmos. Sci.*, **55**(18), 2960–2973.

Masonis, S. J. and S. G. Warren, 2001: Gain of the AVHRR visible channel as tracked using bidirectional reflectance of Antarctic and Greenland snow. *Int. J. Remote Sens.*, **22**(8), 1495–1520.

McClatchey, R. A., R. W. Fenn, J. E. A. Selby, F. E. Volz and J. S. Garing, 1972: *Optical Properties of the Atmosphere (Third Edition)*. No. 411 in Environmental Research Papers. Air Force Cambridge Research Laboratories, Bedford, Massachusetts.

Michalsky, J. J., 1988: The Astronomical Almanac's algorithm for approximate solar position (1950–2050). *Solar Energy*, **40**(3), 227–235.

MISR Science Team, 2004: MISR level 1 products quality statement. `http://eosweb.larc.nasa.gov/PRODOCS/misr/Quality_Summaries/L1_Products_20040310.html`.

Nakajima, T. and M. Tanaka, 1988: Algorithms for radiative intensity calculations in moderately thick atmospheres using a truncation approximation. *J. Quant. Spectrosc. Radiat. Trans.*, **40**(1), 51–69.

Nemesure, S., R. D. Cess, E. G. Dutton, J. J. DeLuisi, Z. Li and H. G. Leighton, 1994: Impact of clouds on the shortwave radiation budget of the surface-atmosphere system for snow-covered surfaces. *J. Climate*, **7**(4), 579–585.

Nicodemus, F. E., J. C. Richmond, J. J. Hsia, I. W. Ginsberg and T. Limperis, 1977: *Geometrical Considerations and Nomenclature for Reflectance*. NBS Monograph 160. National Bureau of Standards.

O'Rawe, P., 1991: *Monte Carlo Models for the Reflection of Sunlight from Rough Snow Surfaces: Suncups and Sastrugi*. Master's thesis, Univ. of Washington, Seattle, 521 pp.

Painter, T. H. and J. Dozier, 2004: Measurements of the hemispherical-directional reflectance of snow at fine spectral and angular resolution. *J. Geophys. Res.*, **109**.

Ricchiazzi, P., S. Yang, C. Gautier and D. Sowle, 1998: SBDART: A research and teaching software tool for plane-parallel radiative transfer in the Earth's atmosphere. *Bull. Amer. Meteor. Soc.*, **79**(10), 2101–2114.

Schwerdtfeger, W., 1984: *Weather and Climate of the Antarctic*. Elsevier, Amsterdam, 261 pp.

Six, D., M. Fily, L. Blarel and P. Goloub, 2005: First aerosol optical thickness measurements at Dome C (East Antarctica), summer season 2003–2004. *Atmos. Environ.*, **32**, 5041–5050.

Stamnes, K., S.-C. Tsay, W. Wiscombe and K. Jayaweera, 1988: Numerically stable algorithm for discrete-ordinate-method radiative transfer in multiple scattering and emitting layered media. *Appl. Opt.*, **27**(12), 2502–2509.

Suttles, J. T., R. N. Green, P. Minnis, G. L. Smith, W. F. Staylor, B. A. Wielicki, I. J. Walker, D. F. Young, V. R. Taylor and L. L. Stowe, 1988: *Angular Radiation Models for Earth-Atmosphere System, Volume 1–Shortwave Radiation.* NASA Reference Publication 1184. National Aeronautics and Space Administration.

Walden, V. P., S. G. Warren and F. J. Murcray, 1998: Measurements of the downward longwave radiation spectrum over the Antarctic Plateau and comparisons with a line-by-line radiative transfer model for clear skies. *J. Geophys. Res.*, **103**(D4), 3825–3846.

Warren, S. G., 1982: Optical properties of snow. *Rev. Geophys. Space Phys.*, **20**(1), 67–89.

Warren, S. G., R. E. Brandt and T. C. Grenfell, 2006: Visible and near-ultraviolet absorption spectrum of ice from transmission of solar radiation into snow. *Appl. Opt.*, **45**(21), 5320–5334.

Warren, S. G., R. E. Brandt and P. O'Rawe Hinton, 1998: Effect of surface roughness on bidirectional reflectance of Antarctic snow. *J. Geophys. Res.*, **103**(E11), 25,789–25,807.

Warren, S. G. and A. D. Clarke, 1990: Soot in the atmosphere and snow surface of Antarctica. *J. Geophys. Res.*, **95**(D2), 1811–1816.

Welch, R. M. and B. A. Wielicki, 1989: Reflected fluxes for broken clouds over a Lambertian surface. *J. Atmos. Sci.*, **46**(10), 1384–1395.

Wielicki, B. A., B. R. Barkstrom, E. F. Harrison, R. B. Lee III, G. L. Smith and J. E. Cooper, 1996: Clouds and the Earth's Radiant Energy System (CERES): An Earth Observing System experiment. *Bull. Amer. Meteor. Soc.*, **77**(5), 853–868.

Wilson, M. J. and L. Di Girolamo, 2004: The utilization of MISR for polar cloud modeling. *Geoscience and Remote Sensing Symposium, 2004. IGARSS '04. Proceedings. 2004 IEEE International*, Vol. 7, IEEE, 4361–4362.

Wiscombe, W. J., 1980: Improved Mie scattering algorithms. *Appl. Opt.*, **19**(9), 1505–1509.

Wiscombe, W. J. and S. G. Warren, 1980: A model for the spectral albedo of snow. I: Pure snow. *J. Atmos. Sci.*, **37**(12), 2712–2733.

Yang, P. and K. N. Liou, 1996: Geometric-optics-integral-equation method for light scattering by nonspherical ice crystals. *Appl. Opt.*, **35**(33), 6568–6584.

VITA

Stephen Hudson was born 25 December 1977 in Media, Pennsylvania, where he lived until college. Early on, he developed interests in weather and the polar regions, which led him to study atmospheric sciences at Cornell University, where he received a Bachelor of Science degree in Atmospheric Sciences in 2000. He came to the University of Washington in September 2000 to continue his studies and to focus on the polar regions. In 2004 he earned a Master of Science in Atmospheric Sciences from the University of Washington, with a study of the surface-based temperature inversion on the Antarctic Plateau, which involved eleven months of field work through the winter at the South Pole. His publications from his time at the University of Washington are listed below.

Hudson, S. R. and S. G. Warren, 2007: An Explanation for the Effect of Clouds over Snow on the Top-of-Atmosphere Bidirectional Reflectance. *J. Geophys. Res.*, **112**, D19202.

Hudson, S. R., S. G. Warren, R. E. Brandt, T. C. Grenfell, and D. Six, 2006: Spectral Bidirectional Reflectance of Antarctic Snow: Measurements and Parameterization. *J. Geophys. Res.*, **111**, D18106.

Hudson, S. R. and R. E. Brandt, 2005: A Look at the Surface-Based Temperature Inversion on the Antarctic Plateau. *J. Climate*, **18**, 1673–96.

Hudson, S. R., M. S. Town, V. P. Walden, and S. G. Warren, 2004: Temperature, Humidity, and Pressure Response of Radiosondes at Low Temperatures. *J. Atmos. Oceanic Technol.*, **21**, 825–36.

Warren, S. G. and S. R. Hudson, 2003: Bacterial Activity in South Pole Snow Is Questionable (Comment). *Appl. Environ. Microbiol.*, **69**, 6340–41.